Max-Planck-Institut für Metallforschung
Stuttgart

Solid-Solid Phase Transformation Kinetics

Rico Bauer

Dissertation
an der
Universität Stuttgart

Bericht Nr. 230
November 2010

Solid-Solid Phase Transformation Kinetics

Von der Fakultät Chemie der Universität Stuttgart
zur Erlangung der Würde eines Doktors der Naturwissenschaften (Dr. rer. nat.)
genehmigte Abhandlung

vorgelegt von

Rico Bauer

aus Jena

Hauptberichter:	Prof. Dr. Ir. E. J. Mittemeijer
Mitberichter:	Prof. Dr. J. Bill
Prüfungsvorsitzender:	Prof. Dr. Th. Schleid
Tag der Einreichung:	18.08.2010
Tag der mündlichen Prüfung:	23.11.2010

MAX-PLANCK-INSTITUT FÜR METALLFORSCHUNG STUTTGART
INSTITUT FÜR MATERIALWISSENSCHAFT DER UNIVERSITÄT STUTTGART

Stuttgart 2010

Contents

1 Introduction

The application and development of materials is intrinsically tied to the development of mankind. Materials and the understanding of its behavior have been playing an important role since the beginning of civilization. In ancient Egypt the most important material was simple stone (ceramic) machined with copper and, probably, iron-based tools leading to impressive civil works like the Great Pyramids of Giza. A better availability and improved production and machining processes of raw materials led to the intensive use of materials like copper and bronze (Copper and Bronze Age) and iron (Iron Age) which were used for e. g. tools, dishes, weaponry,… (Fig. 1.1). The use of materials by ancient crafts over the millenniums was affected by *materials technology*, i. e. procedural and observational knowledge about the processing of materials led to the desired properties [1]. This kind of approach was very successful as documented by the advance made of entire civilizations, but also affected by a lack of understanding of the underlying mechanisms being responsible for the obtained properties.

In contrast, *materials science* is placing emphasis to the understanding of the underlying mechanisms on a *micro*- (nm - µm), *meso*- (µm - mm) and *macro*scale (> mm) in order to improve the properties of and/or find new materials. Materials science is affecting the manipulation of materials since the late 19^{th} century basing in particular on scientific milestones like the atomic theory or the quantum mechanics as basic paradigms for today's progress in *materials science*. The speed of this progress during the last century in comparison to the ages before has raised up tremendously, forced by and, concurrently, leading to technological advance. After a period of analysing the basic mechanisms, nowadays a period of synthesising materials with desired properties is under way leading to a very large spectrum of more or less complex materials which have been developed applying the knowledge gained from the scientific research on metals, ceramics, polymers, compounds, and, since the latest, bio-inspired and nano- materials (Fig. 1.1).

The science of materials is of great importance in order to understand existing and to solve new problems, e. g. improvement of materials properties or synthesis of new materials from the point of ecology and the environment being in constant conflict with economical and technological aims and/or interests.

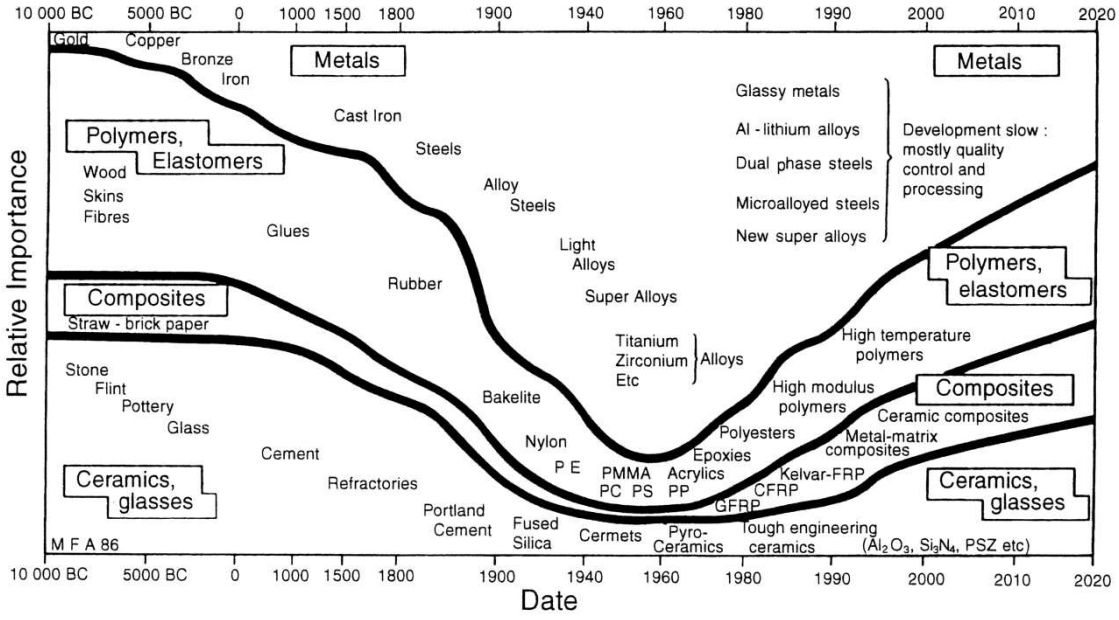

Fig. 1.1: Overview of the relative importance of materials with time [2].

The progress of materials science is also related to the paradigms and laws in order to understand and describe the behaviour of matter [1]. A full understanding of processes in materials at all scales is not available for a long time yet. Models are only as powerful as the things which can be described by them and, hence, a permanent urge is necessary in order to arrive at point leading to better model descriptions of observed phenomena.

A milestone in materials science was the identification of the microstructure as an important parameter in order to control the materials properties, additionally to the chemical composition. Materials scientist got more and more aware about the mechanisms within the materials (at first in metals and after it in all other material classes by transferring the discovered principles) influenced by any thermo-mechanical treatment. In doing so, materials scientist achieved understanding for instance about the influence of thermal annealing treatments which surprisingly led to both, age hardening and softening.

One of many elementary and well-known examples is the thermo-mechanical treatment of iron-based alloys. After producing the material by alloying iron, carbon and other essential elements (e. g. Cr, Ni, Si, Mn,…) the knowledge of a materials scientist becomes necessary. The material can be subjected to processes like quenching, tempering, hot or cold forging, work or age hardening etc. in order to influence the phase composition (e. g. martensite, austenite, perlite, etc.) and microstructure (e. g. grain size, dislocation density, precipitate size, distribution etc.) without changing the chemical composition.

Another well-known example is the precipitation hardening which leads to an increase in strength. It was first discovered in aluminium based alloys in the early 20th century. After gaining the knowledge about the underlying processes upon precipitation hardening (partly dependent on technological progress as X-ray diffractometry or transmission electron microscopy) many other alloy system were found to be hardenable. This requires a region of completely or partly solid solution at high temperatures and, upon cooling, a decreasing solubility of one of the components (Fig. 1.2). Again, the typical metallurgical heat treatment comes into operation as solution annealing at high temperatures followed by quench (hardening) and precipitation heat treatment below the solubility line. This leads to precipitates characterized by their nature, size and distribution.

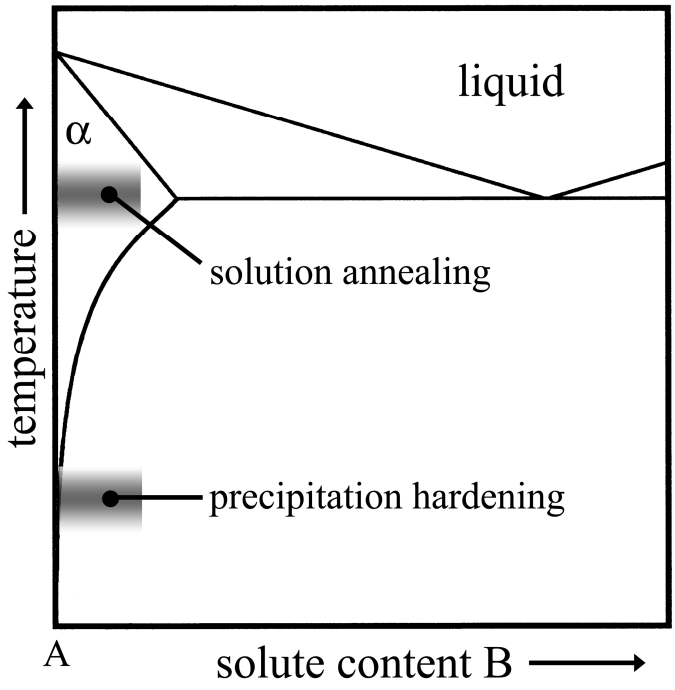

Fig. 1.2: Schematic of the conditions of an alloy being hardenable by precipitation heat treatment

Despite the knowledge of the basic processes for a wide range of phase transformations in materials, most of the process parameters are still of empirical nature and, hence, a description basing on the fundamentals of thermodynamics and kinetics is favoured in order to gain a better understanding of these processes.

1.1 Modular Phase Transformation Model

The analysis of a phase transformation applying the modular phase transformation model according to Ref. 3 allows for a separate treatment of the three overlapping mechanisms of nucleation, growth and impingement (Fig. 1.3). This model can be applied to isothermally (constant temperature) as well as isochronally (constant change of temperature as a function of time) conducted experiments following an analytical or numerical approach. Thereto, the transformation curve, calculated with the model, is generally fitted to that from the experiment, yielding a description of the controlling kinetic process. The numbers of kinetic parameters which describe the considered phase transformation depend on the chosen model description [4].

A phase transformation can be experimentally followed by tracing a meaningful physical property, e. g. the length change by dilatometry, the released heat by calorimetry, the lattice parameter change by X-ray diffractometry,… as a function of time, *t*, and temperature, *T*. The knowledge of both the initial and end value of the traced physical property makes the degree of transformation, f ($0 \leq f \leq 1$), accessible [5].

Generally, the degree of transformation, *f*, is determined by the thermal history, i. e. in order to arrive at an end state, the material in its initial state can be subjected to different types of heat treatment. Hence, it depends not on *t* or *T*(*t*) in a direct way. A general full description of the reaction path, i. e. the degree of transformation, can be given by introducing a path variable *ß* [5]. The path variable does only depend on thermal history and yields the following simplified expression for the degree of transformation:

$$f = F(\beta). \tag{1.1}$$

Independent from the thermal history (i. e. the path in the time-temperature-diagram) the path variable can be expressed by taking the integral over time of a rate constant *K*(*T*(*t*)):

$$\beta = \int K(T(t))\,dt. \tag{1.2}$$

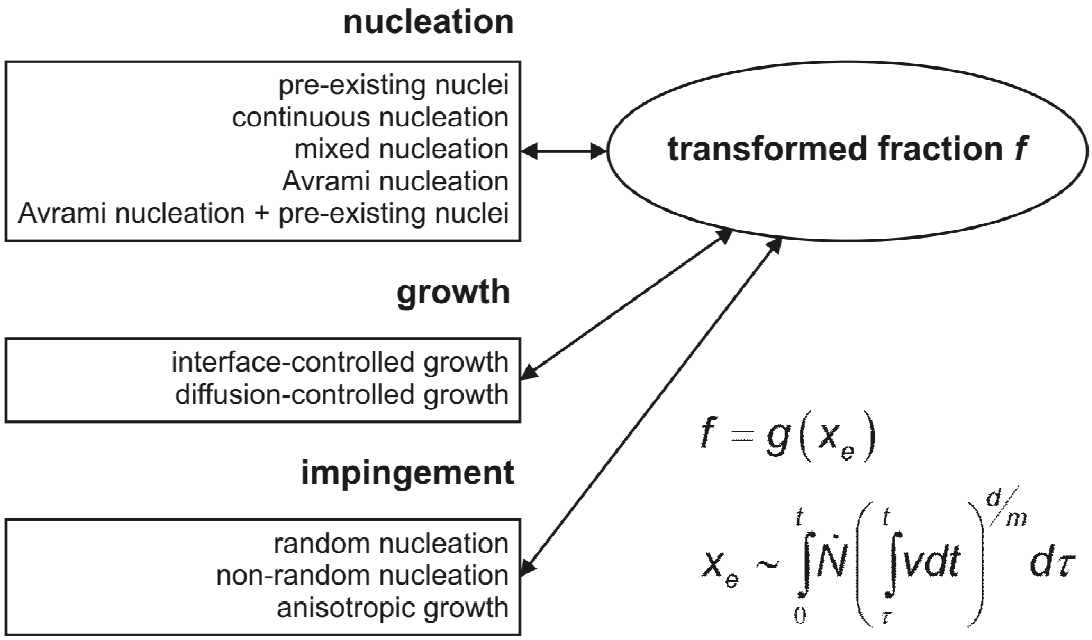

Fig. 1.3: Schematic of the modular phase transformation model. Adopting specific models for nucleation (nucleation rate $\dot{N}$) and growth (volume *Y*) yields the extended transformed fraction, x_e, from which the real transformed fraction, *f*, can be calculated using an appropriate impingement correction function, $g(x_e)$ [3, 4].

This expression for *ß* is compatible with the additivity rule [5] equivalent to an "isokinetic" behavior, i. e. the mechanism of a transformation does not change throughout the temperature or time range of interest. In general, despite of a rigorous theoretical justification [5], the rate constant can be expressed by an Arrhenius-type equation as

$$K\left(T\left(t\right)\right) = K_0 \exp\left(-\frac{Q}{RT\left(t\right)}\right) \tag{1.3}$$

with K_0 as the temperature and time independent pre-exponential factor, *Q* as the effective activation energy describing the temperature dependence of the transformation in a given time-temperature-range and R as the gas constant.

The use of a path variable is advantageous as for a given time-temperature window the kinetic parameters found are independent of the type of annealing as long as a isokinetic behavior prevails.

General explicit analytical expressions or numerical values for the degree transformation can be derived in terms of the modular transformation model as follows (see also Fig. 1.3). Supposing that every product particle grows into an infinitely large parent phase, the volume of all product particles at time *t* is given by the so called extended volume

(1.4) $$V_e = \int_0^t V\dot{N}(\tau)Y(\tau)\,\mathrm{d}\tau$$

where V_e is the extended volume and V is the specimen volume, which is supposed to be constant throughout the transformation. Thereby, an appropriate nucleation model for the description of the nucleation rate $\dot{N}$ and an appropriate growth model for the description of the volume Y of a particle at time t nucleated at time τ have to be used.

Evidently, product phase particles cannot nucleate and grow in specimen volume that has already been occupied by other product phase particles. This is called “hard impingement” (Fig. 1.4(a)). Further, if diffusion of solute towards product particles is necessary to establish growth, then a solute depletion zone develops around a growing product particle in which zone less likely further nucleation can take place (because of a lesser supersaturation) or even no further nucleation can occur at all (if the supersaturation has become negligible). This is called “soft impingement” (Fig. 1.4(b)).

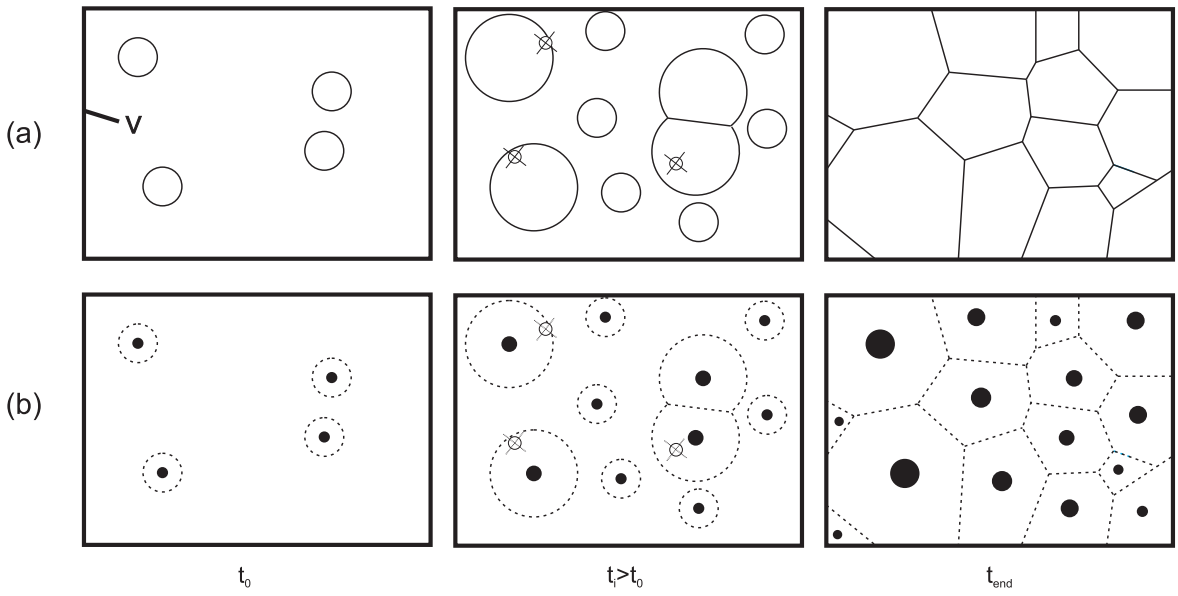

Fig. 1.4: Schematic of a phase transformation reaction exhibiting constant nucleation rate during the whole transformation from t_0 to $t_{end} > t_0$ in case of (a) hard impingement of hard spheres, e. g. solidification of a pure metal, and (b) soft impingement of diffusion fields (dashed), e. g. precipitation of second product phase particles (black filled circles) from an initially supersaturated solid solution.

Evidently, the extended volume, V_e, does not account for hard or soft impingement. A relationship between the actually transformed volume at time t, V_t, and the extended volume, V_e, or between the real transformed fraction, $f \equiv V_t/V$, and the extended transformed fraction, $x_e = V_e/V$, is required. This is called impingement correction. The expression for the extended volume is then substituted into the appropriate impingement correction function $g(x_e)$ (Fig. 1.3) to give the degree of transformation, f ($0 \le f \le 1$).

Applying the recipe for calculating the degree of transformation as described in Refs. 4 and 7, JMA like equations are obtained in case of isothermal or isochronal annealing (i. e. annealing with constant heating rate) for transformations using for nucleation either the continuous nucleation model or the site saturation model and for growth, diffusion controlled growth or interface controlled growth, and for impingement the assumption that the isotropically growing particles are dispersed randomly throughout the total volume

$$f = 1 - \exp\left(-\beta^n\right) = 1 - \exp\left(-x_e\right) \tag{1.5}$$

with the growth exponent *n*. Indeed, a lot of experimental kinetic data on phase transformations have been interpreted on such a basis. The prescription by Eq. (1.5) means that the equations that describe the degree of transformation are identical in the cases of isothermal or isochronal annealing, if they can be expressed as a function of β.

To account for growth anisotropy (relevant to many solid-solid phase transformations) the following impingement correction has been proposed [10 - 13]

$$f = 1 - \left[1 + (\xi - 1)\, x_e\right]^{-1/(\xi - 1)} \tag{1.6}$$

with the impingement parameter $\xi > 1$. In case of hard impingement of anisotropically growing particles Eq. (1.6) accounts for the, on average, smaller time interval compared to impingement according to Eq. (1.5), in which the randomly dispersed nuclei can grow before 'blocking' by other particles occurs.

Equations (1.5) and (1.6) have originally been given for hard impingement. A rigorous treatment of soft impingement does not exist. However, in many cases, e g. precipitation of a second product phase from an initially supersaturated solid solution, no good description for the entire transformation is obtained [8] and fitting with a JMA like equation as given by Eq. (1.5) has to be restricted to the first part of the transformation [9]. This hints at the inappropriateness of the correction for impingement given by Eq. (1.5). It can be inferred [14] that Eq. (1.5) also halts for soft impingement (in case of randomly dispersed nuclei and isotropic growth). This may be understood as that for the case of "soft impingement" each product particle is supposed to be surrounded, effectively, by an outer solute depleted shell of size such that upon completed precipitation all precipitate particles with their surrounding solute depleted shells occupy the whole volume of the specimen. Similarly it can be expected that in case of anisotropic growth of e. g. plate-like instead of spherical particles, Eq. (1.6) can also be used as an viable approximation for soft impingement as shown in Ref. 8.

The presented treatment leads to explicit expressions for the kinetic parameters n, Q and K_0 for a range of nucleation and growth modes for isothermal and isochronal annealing (see Tables 1 to 3 in Ref. 4).

The overall activation energy Q can be expressed as a function of the activation energy for nucleation, Q_N, and the activation energy for growth, Q_G [7]:

$$Q = \frac{\frac{d}{m} Q_G + \left(n - \frac{d}{m}\right) Q_N}{n} \tag{1.7}$$

with d as the growth dimension and m as the growth mode ($m = 1$ in case of interface controlled growth, $m = 2$ in case of diffusion controlled growth). Values for Q_N and Q_G can be determined separately by varying the nucleation mode, e. g. by pre-annealing.

Values for Q and n can be determined without recourse to any specific model using procedures given in Refs. 3 and 4.

For isochronal anneals of variable heating rate the effective activation energy Q can be deduced from the temperatures where a specific, chosen degree of transformation is attained and for isothermal anneals of variable temperature the effective activation energy Q can be deduced from the time needed where a specific, chosen degree of transformation is attained, according to a Kissinger like analysis [3].

A value for the growth exponent n for isochronal anneals of variable heating can be deduced from a plot of $\ln(\ln(1 - f_T))$ vs. $\ln(\Phi)$ in case of impingement according to Eq. (1.5) or $\ln[((1 - f_T)^{1-\xi} - 1)/(\xi - 1)]$ vs. $\ln(\Phi)$ in case of impingement according to Eq. (1.6). A value for the growth exponent n for isothermal anneals of variable temperature can be deduced from a plot of $\ln(-\ln(1 - f))$ vs. $\ln(t)$ in case of impingement according to Eq. (1.5) or $\ln[((1 - f)^{1-\xi} - 1)/(\xi - 1)]$ vs. $\ln(t)$ in case of impingement according to Eq. (1.6), according to a procedure presented in Ref. 4.

1.2 Focus of this Thesis

This thesis is focussing on the description of the kinetics of solid-solid phase transformations. Different types of phase transformations are investigated, such as an allotropic phase transformation (conversion of one crystal structure to another without composition change) or, in contrast, the precipitation of a second product phase. In all cases, the associated microstructural evolution and morphology is interpreted with regard to the results obtained from the kinetic analysis.

1.3 Methodology

In this thesis the kinetics of the considered phase transformations are investigated by combined use of differential scanning calorimetry (DSC), (high-resolution) transmission electron microscopy [(HR)TEM], and, depending on necessity, X-ray diffractometry (XRD), light optical microscopy (LM) and hardness measurements. This combination is necessary in order to reach a comprehensive description of the occurring processes during the phase transformation, to obtain input parameters for the kinetic model approach and to interpret the results from the kinetic analysis. The operation mode of the widely-used DSC and (HR)TEM methods are described briefly in the following.

1.3.1 Differential Scanning Calorimetry

In a power compensated DSC, as used in this work, the transition enthalpy of the investigate phase transformation reaction is measured by an external energy source [6]. The difference in heating or cooling between the sample and reference is then used as a measurement signal. The DSC contains a sensor head with two identical measuring cells, of which one serves as a measurement and the other as a reference cell. Platinum wire coils are installed at the bottom of both cells with good thermal contact. These are used for direct heating of the cells and as a resistance thermometer for temperature measurement (Fig. 1.5). Both cells are held at constant temperature during isothermal measurements or heated/cooled upon isochronal annealing with a constant rate, dT/dt.

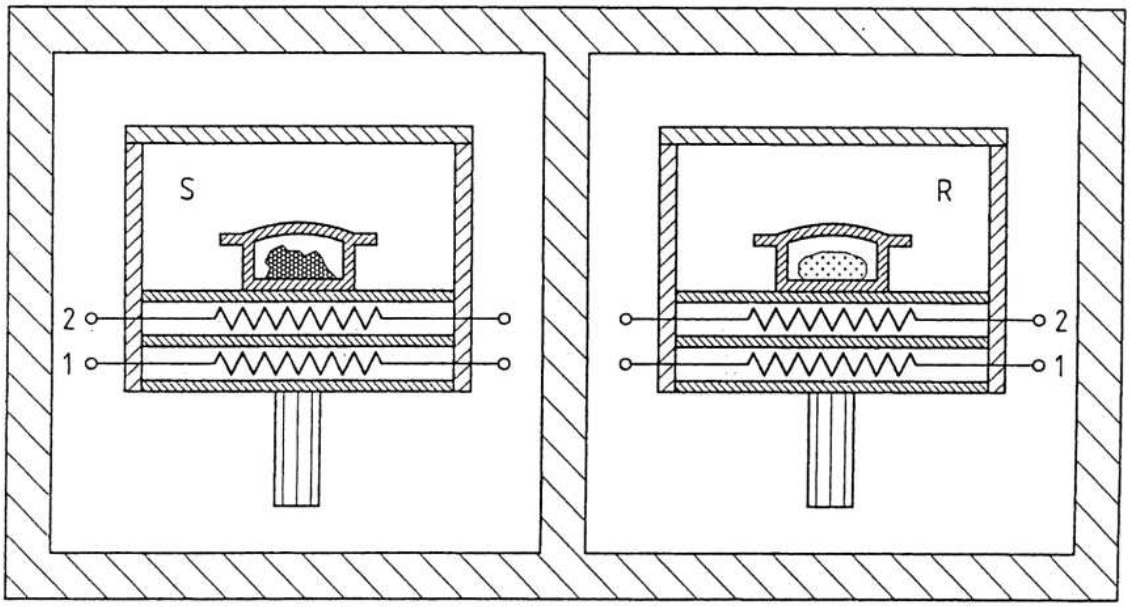

Fig. 1.5: Set-up of the measuring system of a power compensation DSC by Perkin Elmer according to Ref. 6.: S sample measuring system with sample crucible, microfurnace and lid, R reference sample system (mostly empty) (analogous to S), 1 heating wire, 2 resistance thermometer. Both measuring systems, separated from each other, are positioned in a equilibrated surrounding (block).

In a dynamic measurement, i. e. at constant heating or cooling rate, the area enclosed by the complete DSC signal, which shows a peak e. g. for one reaction, is given by the transformation enthalpy, ΔH, the heating of the sample and the heating of the reference using the relevant heat capacity values. For isothermal measurements, the reference is chosen such that the difference in heat capacity in comparison to the sample is as small as possible. In practice, usually an empty pan is used.

Several procedures associated with certain assumptions are used in order to extract the transformation enthalpy from the heat signal which is generally composed of contributions from the pans, sample, reference and DSC device.

In case of an allotropic solid-solid reaction, as it is the case for e. g. Co (*hcp* Co as low temperature phase, *fcc* Co as high temperature phase), the measured heat signal can be corrected with a heat signal obtained from a DSC scan with empty pans. Generally the heat capacity does not change during a solid-solid state reaction (excepting e. g. crystallization of initially amorphous alloys, e.g. Ref. 15). The transformation enthalpy is thus obtained from the area enclosed by the heat signal and a linear baseline which connects those parts of the heat signal prior to and after the peak, i. e. a virtual heat signal "without" a reaction is supposed.

In the case of a reaction in which an initially metastable state is transformed into a stable state, a second run is performed directly after the first run adopting, that the transformation does only take place during the first run. The transformation enthalpy is thus obtained, after subtracting the second from the first run, from the area enclosed by the remaining heat signal.

The degree of the transformed fraction, f, corresponding to the investigated reaction can be calculated as a function of time or temperature directly from the extracted heat signal using the correlation $\mathrm{d}f/\mathrm{d}t = (\mathrm{d}\Delta H(t)/\mathrm{d}t)/\Delta H$.

In this work a Perkin1 DSC from PerkinElmer is used for both annealing modes, isothermal and isochronal, in order to gain information on the kinetics of the investigated reaction upon different heat treatments. Details on the experimental procedure as calibration and annealing program are given in the corresponding chapters of this work.

1.3.2 (High-Resolution) Transmission Electron Microscopy

In TEM accelerated electrons are focused (using magnetic lenses) onto a sample typically 50 to 150 nm thick [16]. During passing the specimen (transmission) the electrons are scattered (dynamical diffraction). In order to illustrate the information carried by the scattered electrons, techniques like conventional imaging (bright-field TEM), electron diffraction (selected area electron diffraction, SAD) or phase-contrast imaging (high-resolution TEM) are widely used [17].

Bright-field images are obtained from the primary beam by filtering out all diffracted beams using an aperture lens. The contrast results from a position sensitive variation of intensity of the transmitted electron beam due to the diffraction in the specimen (diffraction contrast). The diffraction contrast decreases with increasing specimen thickness due to a higher amount of diffuse, inelastic diffraction of the electrons in the specimen. In principal all diffracted beams can be used leading to different imaging conditions (e. g. two-beam condition, weak-beam condition, etc).

A major strength of the TEM is due to the fact that there is always a comparison between image and diffraction pattern possible. This makes a systematic alignment of contrast conditions possible and, further, the determination of crystallography and geometry of structural elements (e. g. precipitate particles).

In HRTEM the theoretical resolution is almost completely exhausted (0.1 – 0.2 nm). In contrast to conventional TEM the diffracted electron beams (aperture) are refracted by an electron lens [17]. This leads to an interference pattern formed from the phase relationships of diffracted beams. For irradiation in low-indexed zone axes the three-dimensional lattice structures of the sample and two-dimensional projection of atomic columns (not of individual atoms!) can be mapped.

In this study (HR)TEM was applied using different types of (HR)TEM devices in order to trace the microstructural evolution upon a defined annealing procedure or to characterize the crystal structure of phase transformation products.

1.4 Investigated Systems

1.4.1 Co

Pure Cobalt exhibits an allotropic phase transformation at the equilibrium temperature $T_a = 690 \pm 7$ K [19] with the hexagonal closest packed (*hcp*) modification as low temperature phase and the face centered cubic (*fcc*) modification as high temperature phase. This allotropic transformation fulfills the characteristics of a martensitic transformation as no diffusion and no composition change occur leading to the characteristic athermal character of this type of phase transformation [20 - 22]. The occurrence of a body centered cubic (*bcc*) crystal structure of Co is perceived as *forced* structure [23] and was found by enforced grow via thin layer deposition on orientated substrates [24].

The lattice parameters for the *hcp* polymorph are $a_{Co,hcp} = 0.25071$ nm and $c_{Co,hcp} = 0.40686$ nm and for the *fcc* polymorph $a_{Co,fcc} = 0.35447$ nm [25]. The allotropic phase transformation, e. g. for *hcp*→*fcc*, is associated with a contraction parallel to the closest packed plane $\{0001\}_{Co,hcp}$ / $\{111\}_{Co,fcc}$ of -0.024 % and perpendicular to the closest packed plane of +0.242 % [26]. The kinetics of the *hcp*→*fcc* phase transformation is investigated in chapter 5.

1.4.2 AuCo

The two metals Au and Co constitute an eutectic binary system (see phase diagram [18], Fig. 1.6) with an *fcc* Au-rich phase and a Co-rich phase showing an allotropic phase transformation at $T_a = 690 \pm 7$ K [19] with an *hcp* crystal structure below T_a and an *fcc* crystal structure above T_a. The allotropy of Co leads to a pronounced miscibility gap for the solid solution. The maximum solubility of Co in *fcc* Au is about nine times larger than that of Au in *fcc* Co. Below T_a the solubility of Au in *hcp* Co is less than 0.05 at.% and the solubility of Co in *fcc* Au is less than 0.2 at.%.

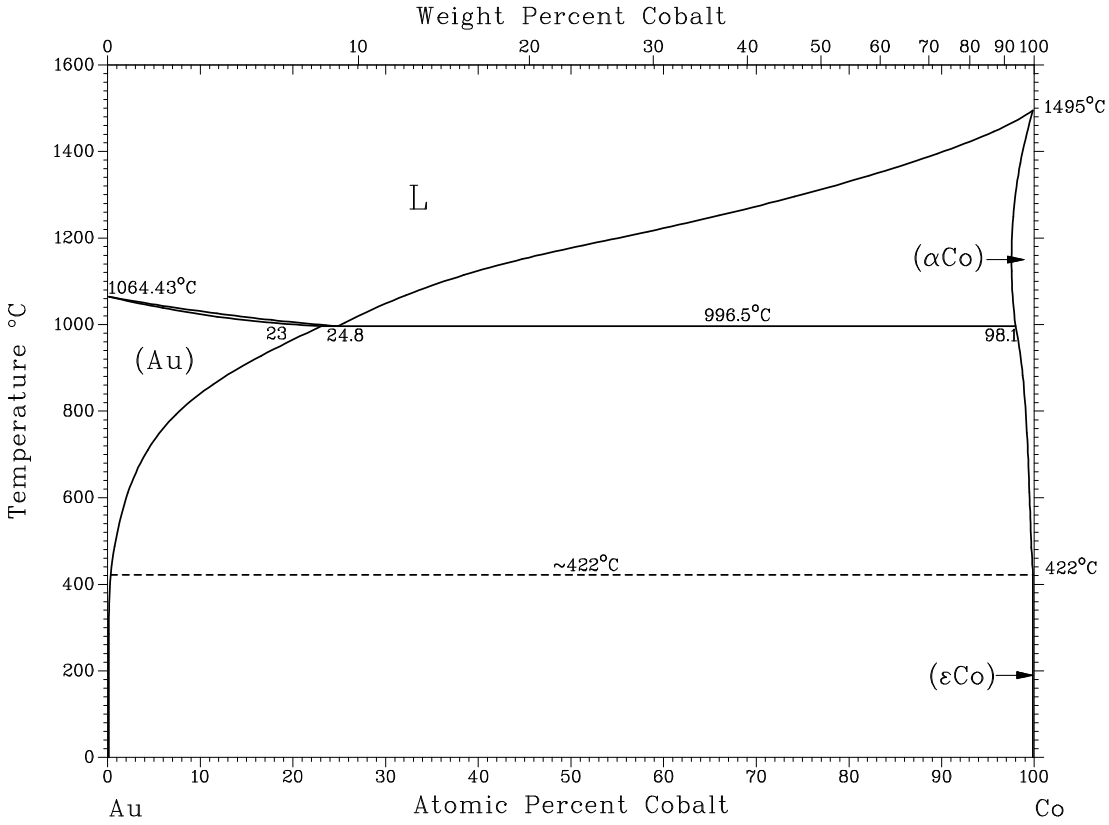

Fig. 1.6: Phase diagram of the binary system Au-Co according to Ref. 18.

Below T_a the approximately pure Au-rich and Co-rich phase exhibit a large lattice mismatch $\delta = (a_{Co} - a_{Au})/a_{Au} \cdot 100\% = -13.3\%$ with $a_{Co} = 0.35447$ nm and $a_{Au} = 0.40782$ nm [25]. Upon precipitation of Co from a supersaturated Au-rich solid solution of Au and Co the formation of plate-like Co precipitates is expected due to the large lattice mismatch (Fig. 1.7) [27].

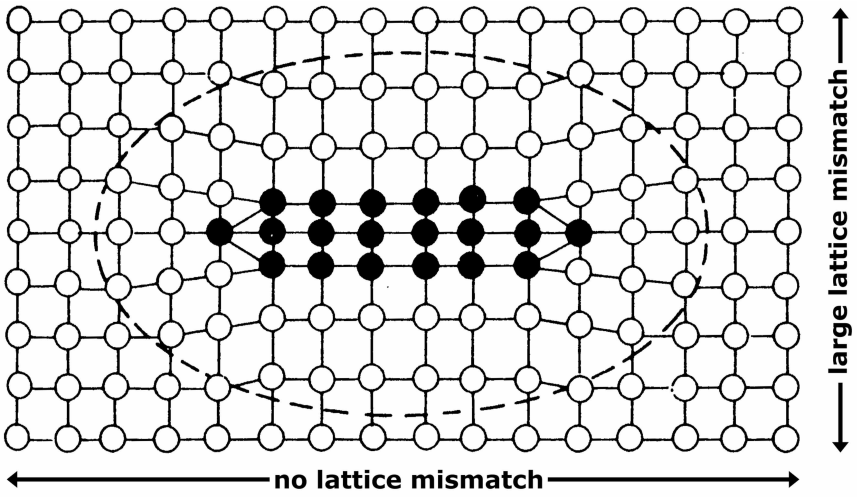

Fig. 1.7: Formation of a coherent thin rigid plate-like inclusion in a soft matrix with no lattice misfit parallel and a large misfit perpendicular to the plane of the plate (graphic according to Ref. 27).

1.4.3 CuCo

The two metals Co and Cu constitute a peritectic binary system (see phase diagram [28], Fig. 1.8) exhibiting a large miscibility gap with a negligible solubility of the components in each other below 873 K. The Cu mixed crystal exhibits a *fcc* crystal structure with a maximum solubility of Co of 8 at. % at the peritectic temperature 1385 K. The Co mixed crystal exhibits an allotropic reaction at the equilibrium temperature T_a = 690±7 K [19] with a *hcp* phase at low temperature and a *fcc* phase at high temperature.

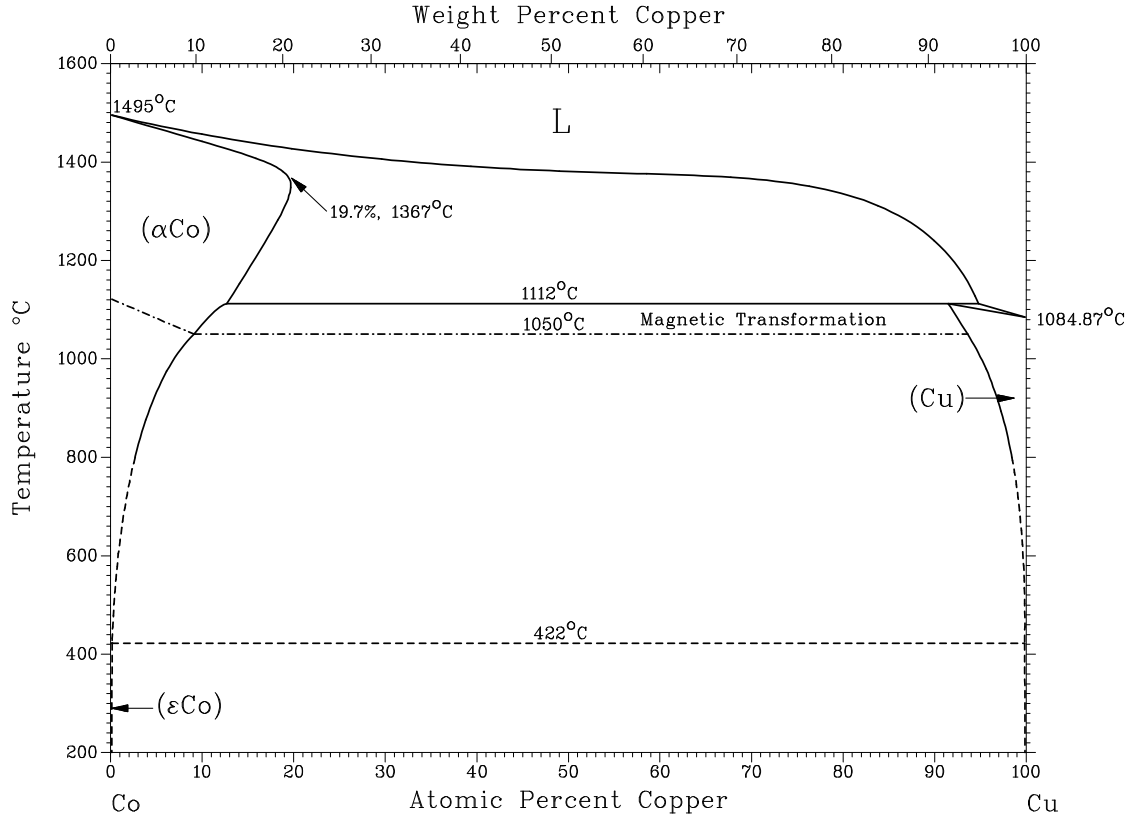

Fig. 1.8: Phase diagram of the binary system Co-Cu according to Ref. 28.

The lattice mismatch, δ, of the nearly pure alloy elements Cu and Co below 873 K is $\delta = (a_{Co} - a_{Cu})/a_{Cu} \cdot 100\% = -1.9\%$ with a_{Co} = 0.35447 nm and a_{Cu} = 0.36146 nm [25] as the lattice parameter values of Co and Co. In case of precipitation of Co from a supersaturated Cu-rich alloy above T_a the formation of spherical Co particles are favoured due to the low lattice mismatch and a *fcc* crystal structure for both, Co and Cu [27].

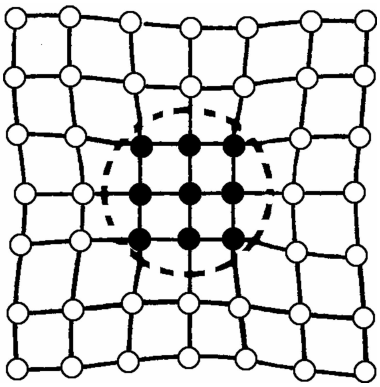

Fig. 1.9: Spherical rigid inclusion formed in a soft matrix exhibiting a small lattice mismatch (graphic according to Ref. 27).

1.5 Outline of this Thesis

Chapter 2 of this thesis presents the investigation of the microstructural evolution of Co precipitates formed upon isochronal annealing of an initially supersaturated Au - 10.12 at. % Co solid solution. It was proven, that initially plate-like *bcc* Co precipitates have formed, which deviates from the expected stable *fcc* Co crystal structure. Upon prolonged annealing, i. e. with ongoing precipitation reaction, the *bcc* Co was transformed into *fcc* Co accompanied with a morphological change of the Co precipitate shape from plates to equiaxed particles. Quantitative (high resolution) transmission electron microscopy (HR)TEM analysis and a thermodynamic examination were done.

In *chapter 3* the microstructural evolution and the kinetics of the precipitation of Co from an initially supersaturated Au – 10.12 at.% Co upon isothermal and isochronal annealing were described. The precipitation reaction was followed by DSC, XRD, (HR)TEM and microhardness measurements in order to understand the microstructural evolution. The isothermal and isochronal precipitation kinetics were analyzed using analytical expressions for the description of the phase transformation applying the modular phase transformation model in combination with an appropriate impingement correction.

In *chapter 4* the kinetics of the precipitation of coherent, spherical *fcc* Co from an initially supersaturated Cu – 0.95 at. % Co solid solution upon isochronal annealing is described. The precipitation reaction was followed by DSC and (HR)TEM. Kinetic parameters were obtained from an analytical modular model approach of phase transformation kinetics. A special case of the application of this approach is presented.

In *chapter 5* the microstructural evolution of the allotropic *hcp*-to-*fcc* phase transformation in bulk Co upon isochronally conducted thermal cycling experiments as well as the corresponding kinetics were investigated. Therefore, differential scanning calorimetry (DSC), X-ray diffractometry (XRD) and light optical microscopy (LM) were applied. The phase transformation kinetics was described by an appropriate modular model approach accounting for the nucleation, growth and impingement modes. The evolution of the microstructure upon annealing and the kinetics, depending on the thermal pre-treatment, were successfully described.

References

[1] J. W. Cahn, *Proc Int Conf Solid-Solid Phase Transformations (JIMIC-3)*, The Japan Institute of Metals (1999).

[2] M. F. Ashby, *Materials Selection in Mechanical Design*, 2nd ed. (Butterworth-Heinemann, Oxford, 1999).

[3] E. J. Mittemeijer and F. Sommer *Z Metallkd* **93** (2002) 352.

[4] F. Liu et al., *Int Mat Rev* **52** (2007) 193.

[5] E. J. Mittemeijer, *J Mat Sci* **27** (1992) 3977.

[6] G. W. H. Höhne, W. F. Hemminger, and H.-J. Flammersheim, *Differential Scanning Calorimetry*, 2nd ed. (Springer, Berlin, 2003).

[7] A. T. W. Kempen, F. Sommer, and E. J. Mittemeijer, *J Mat Sci* **37** (2002) 1321.

[8] M. J. Starink, *J Mat Sci* **36** (2001) 4433.

[9] F. S. Ham, *J Phys Chem Solids* **6** (1958) 335.

[10] J. B. Austin and R. L. Rickett, *Trans Am Inst Min Metall Eng* **135** (1939) 396.

[11] E.-S. Lee and Y. G. Kimm, *Acta Metall Mater* **38** (1990) 1669.

[12] E.-S. Lee and Y. G. Kimm, *Acta Metall Mater* **38** (1990) 1677.

[13] M. J. Starink, *J Mat Sci* **32** (1997) 4061.

[14] C. Wert and C. Zener, *J Appl Phys* **21** (1950) 5

[15] H. Nitsche et al., *Z Metallkd* **96** (2005) 1341.

[16] R. F. Egerton, *Electron Energy-Loss Spectroscopy in the Electron Microscope*, 2nd ed. (Plenum Press, New York, 1996).

[17] B. Fultz and J. M. Howe, *Transmission Electron Microcopy and Diffractometry of Materials*, (Springer, Berlin, 2001).

[18] H. Okamoto et al., *Bulletin of Alloy Phase Diagrams* **6** (1985) 449.

[19] J. B. Hess and C. S. Barrett, *J Met* **4** (1952) 645.

[20] *Cobalt Monograph*, Centre d'Information du Cobalt (Brussels, 1960).

[21] F. Sebilleau, and H. Bibring, *In: The Mechanism of Phase Transformation in Metals*. Edited. London, Institute of Metals. 18 (1955) 209.

[22] J. W. Christian, *The Theory of Transformations in Metals and Alloys* (Pergamon, Amsterdam, 2002).

[23] A. Y. Liu, and J. Singh, *J Appl Phys* **73** (1993) 6189.

[24] G. A. Prinz, *Physical Review Letters* **54** (1985) 1051.

[25] P. Villars and L. D. Calvert. *Pearson's Handbook of Crystallographic Data for Intermetallic Phases* **2**, ASM International (Materials Park, Ohio, 1996).

[26] H. Hesemann, *PhD-Thesis*, Universität Stuttgart (2002).

[27] D. A. Porter and K. E. Easterling, *Phase Transformations in Metals and Alloys*. 2nd ed., (Nelson Thornes Ltd, 2001).

[28] T. Nishizawa and K. Ishida, *Bulletin of Alloy Phase Diagrams* **5** (1984) 161.

2 Natural Formation of *bcc* Co; The Initial Stage of Co Precipitation in Supersaturated $Au_{90}Co_{10}$ Alloy

R. Bauer, E. Bischoff and E. J. Mittemeijer

Abstract

Natural formation of the *bcc* modification for Co was demonstrated to occur upon precipitation of Co in supersaturated $Au_{90}Co_{10}$ alloy. The microstructural evolution was investigated by high resolution transmission electron microscopy. Co precipitation starts with the formation of very thin coherent plates along $\{100\}_{Au}$. This initially precipitated Co was shown to be a hitherto unknown metastable *bcc* modification of Co exhibiting a Bain-type orientation relationship with the matrix: $(100)_{Au,fcc}//(100)_{Co,bcc}$ and $[001]_{Au,fcc}//[011]_{Co,bcc}$ (three variants). Prolonged annealing causes the *bcc* Co to transform according to a Bain-type transformation into *fcc* Co, exhibiting the (cube-on-cube) orientation relationship $(100)_{Au,fcc}//(100)_{Co,fcc}$ and $[001]_{Au,fcc}//[001]_{Co,fcc}$ (three variants), in association with loss of coherency and a morphological change from Co platelets to equiaxed Co particles. A delicate balance of interface energy and bulk energy upon precipitation and subsequent growth/coarsening governs the successive appearance of the *bcc* and *fcc* modifications of Co.

2.1 Introduction

Au-Co alloys play an important role as contact material in microelectronic systems, as dental casting alloy and are also of interest as a material exhibiting giant magnetoresistance (GMR) [1 - 3]. The until now known naturally occurring crystalline phases of cobalt have either the hexagonal closed packed (*hcp*) crystal structure, stable below 695 K (at 1 atm), and the face centered cubic (*fcc*) crystal structure, stable above 695 K (at 1 atm) [4]. The investigation of the kinetics and microstructure changes, and the underlying mechanisms of the allotropic *hcp-fcc* phase transformation in bulk and thin layer systems has been subject of research since decades [5 - 16].

Artificially made thin layers of Co on a substrate can occur in a metastable (usually distorted) *bcc* modification likely as a consequence of prevailing very large strains in the concerned (multi) layer / substrate system [17 – 21]. The occurrence of pure *bcc* Co precipitates in the bulk of a supersaturated alloy upon precipitation has not been observed before.

This work provides the first experimental evidence of naturally occurring *bcc* Co precipitates in the early stage of precipitation in bulk $Au_{90}Co_{10}$ alloy. The precipitation process was followed by differential scanning calorimetry (DSC) applying a step-by-step isochronal annealing treatment in combination with (high resolution) transmission electron microscopy (HR)TEM at each step.

2.2 Experimental

A cylindrical ingot of Au - 10.12 at.% Co (further indicated as $Au_{90}Co_{10}$) with a diameter of 8 mm was produced by melting Au (99.95 at.%) and Co (99.995 at.%) in a protective argon atmosphere. The ingot was annealed in an evacuated silica capsule in a protective argon atmosphere (250 mbar at RT) and homogenized within a compensation body at 1233 K for 236 h. The ampoule was quenched in ice water by breaking the capsule. The ingot was hammered down to a diameter of 5 mm and subsequently cut into discs of 500 µm thickness. The specimen discs were recrystallized at 1233 K for 24 h applying the same protective procedure as for the ingot, followed by quenching in ice water by breaking the capsules.

Isochronal annealing experiments were performed applying a differential scanning calorimeter (DSC) Pyris1 from PerkinElmer. The DSC was calibrated using the temperature and enthalpy of melting of In, Pb and Zn. Each specimen disc investigated was encapsulated in Al pans closed and sealed with an Al lid. As reference an empty Al pan with two lids was used to reach a heat capacity similar to that of the Al pan with the specimen. Isochronal annealing was performed with a heating rate of 20 K min^{-1} starting from room temperature. Such DSC runs were interrupted at 550 K, 633 K, 668 K and 773 K by fast cooling of the specimen at a rate of 180 K min^{-1}. The Vickers micro-hardness of the thus (partly) precipitated systems was measured using a micro-hardness tester LEICA VMHT MOT applying a load of 1 gf for 10 s. The microstructure of these specimens was investigated by (HR)TEM.

Specimens for (HR)TEM were prepared by cutting out a stripe from the disc, clamping and glueing it between two Al blades fixed by a Cu ring and cutting again a thin disc. After dimpling the disc to 100 µm, ion thinning was applied using a GATAN precision ion polishing system (PIPS) with a voltage of 3 kV, a current of 10 µA, an incident angle of 9° and a LN_2 cooling unit. TEM was performed using a Philips CM200 instrument operating at 200 kV, and HRTEM was performed using a JEOL 4000FX instrument operating at 400 kV. The images and the selected area electron diffraction patterns were recorded with a CCD camera. The composition of the Au matrix after completed precipitation (at 773 K) was determined by energy-dispersive X-Ray (EDX) microanalysis in a VG501 STEM instrument.

2.3 Results

The baseline-corrected [22] isochronal DSC scan (heating rate of 20 K min^{-1}) of an initially supersaturated $Au_{90}Co_{10}$ is shown in the top part of Fig. 2.1 together with the associated hardness changes in the bottom part of Fig. 2.1.

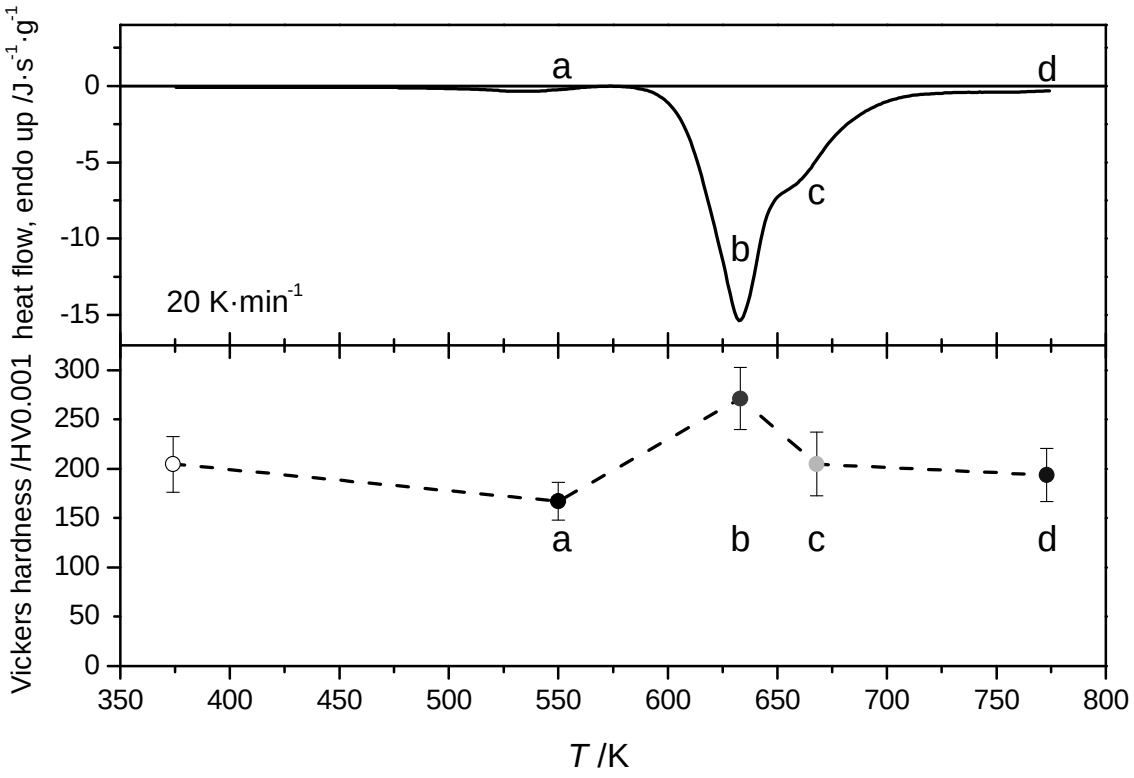

Fig. 2.1: Isochronal baseline-corrected DSC scan (heating rate of 20 K min^{-1}) of initially supersaturated $Au_{90}Co_{10}$ (top part of figure) and the corresponding hardness measurements (bottom part of FIGURE; dashed line has been drawn to guide the eye; the experimental error in the hardness data (each data point is the average of 25 measurements) results from a 10 % uncertainty in the determination of the diagonal length (2 – 5 µm) of the indents). "a": Relaxation of stresses due to quenching after homogenization/recrystallisation (very weak exothermic pre-precipitation peak and decrease of hardness); "b": The formation of *bcc* Co precipitates takes place at temperatures higher than 580 K, leading to a distinct exothermic peak and an increase of hardness; "c": The shoulder in the DSC scan at the high temperature side of the strong exothermic peak is assigned to the *bcc*-to-*fcc* transformation of the Co precipitates in association with elastic (misfit) stress relaxation reaction (loss of coherency); "d": Above 700 K only incoherent *fcc* Co particles occur within a Co-depleted Au matrix.

The microstructure after quenching to room temperature exhibits a high number density of dislocations (as observed with TEM). No other structural defects (stacking faults, twins, "rod-like" defects) were found after intensive analysis. The very small exothermic pre-precipitation peak "a" is due to the relaxation of quenched-in thermal stresses. At the same stage of isochronal annealing, a hardness decrease had occurred from 205±28 HV (as-quenched) to 167±19 HV (annealed to 550 K). The precipitation of Co starts at about 580 K leading to the second exothermic main peak ("b" + "c"). The exothermic main reaction consists of two parts: (i) a sharp, strong peak with a peak maximum at 633 K and a corresponding hardness increase to 271±31 HV ("b") followed by (ii) a shoulder at higher temperatures around 668 K in combination with a hardness decrease to 205±32 HV ("c"). Similar observations were made using several fresh specimens applying heating rates in the range from 5 to 40 K min^{-1} (not shown here).

TEM bright-field and HRTEM images and corresponding selected area diffraction patterns (SADPs) taken after isochronal annealing up to 633 K with 20 K min^{-1} (corresponding with exothermic peak maximum (Fig. 2.1 top) and hardness maximum (Fig. 2.1 bottom)), are shown in Fig. 2.2.

Evidently very thin Co plates only 0.5 to 1 nm thick and with a lateral extension between 5 to 10 nm have developed. The habit plane of the precipitates is of {100} type: In case of a [001] zone axis of the Au-rich matrix two sets of mutually perpendicular precipitate plates along (100) and (010) planes of the Au-rich matrix are observed (Fig. 2.2a); note the streaks in [100] and [010] directions in the SADP. In case of a [011] zone axis of the Au-rich matrix only one variant of the three possible precipitate plate sets can be observed in Fig. 2.2b; note the pronounced contrast due to the strain field surrounding the precipitates (see also the HRTEM image shown in Fig. 2.2d).

If the electron beam is parallel to the [001] and [011] zone axes of the Au-rich matrix (Fig. 2.2a and Fig. 2.2b) the corresponding SADPs show no separate reflections which could be ascribed to the precipitates: The precipitates reveal their presence in the SADPs by streak formation along [100] and [010] (note the thinness of the platelets in these directions).

The morphology and orientation of the coherent platelets appears not compatible with the usual *fcc* and *hcp* modifications of Co. It will be demonstrated immediately below that the observations can be explained adopting a *bcc* modification of Co and a Bain orientation relationship of the platelets with the matrix. Upon tilting the specimen by 9.7° from [011] towards [001], i.e. into an approximate [034] zone axis of the Au-rich matrix, small extra spots become visible next to the 111_{Au} reflections in the SADP (i) (see FIG. 2(c)). The measured *d*-spacing for these extra reflections is 0.206±0.002 nm (ii). From (i) and (ii) it follows that these extra spots are compatible with {110} reflections due to the presence of *bcc* Co precipitates satisfying a $[-111]_{Co,bcc}$ zone axis (see further discussion below). This is compatible with a Bain orientation relationship between the *fcc* Au-rich matrix and the *bcc* Co precipitates: $(100)_{Au,fcc}//(100)_{Co,bcc}$ and $[001]_{Au,fcc}//[011]_{Co,bcc}$. By performing similar tilting experiments these results could be validated: e. g. tilting into the $[-113]_{Co,bcc}$ zone axis, which is close to the $[012]_{Au,fcc}$ zone axis, clear evidence for the 1-21 and $2\text{-}11_{Co,bcc}$ diffraction spots at the appropriate locations in the SADP was obtained.

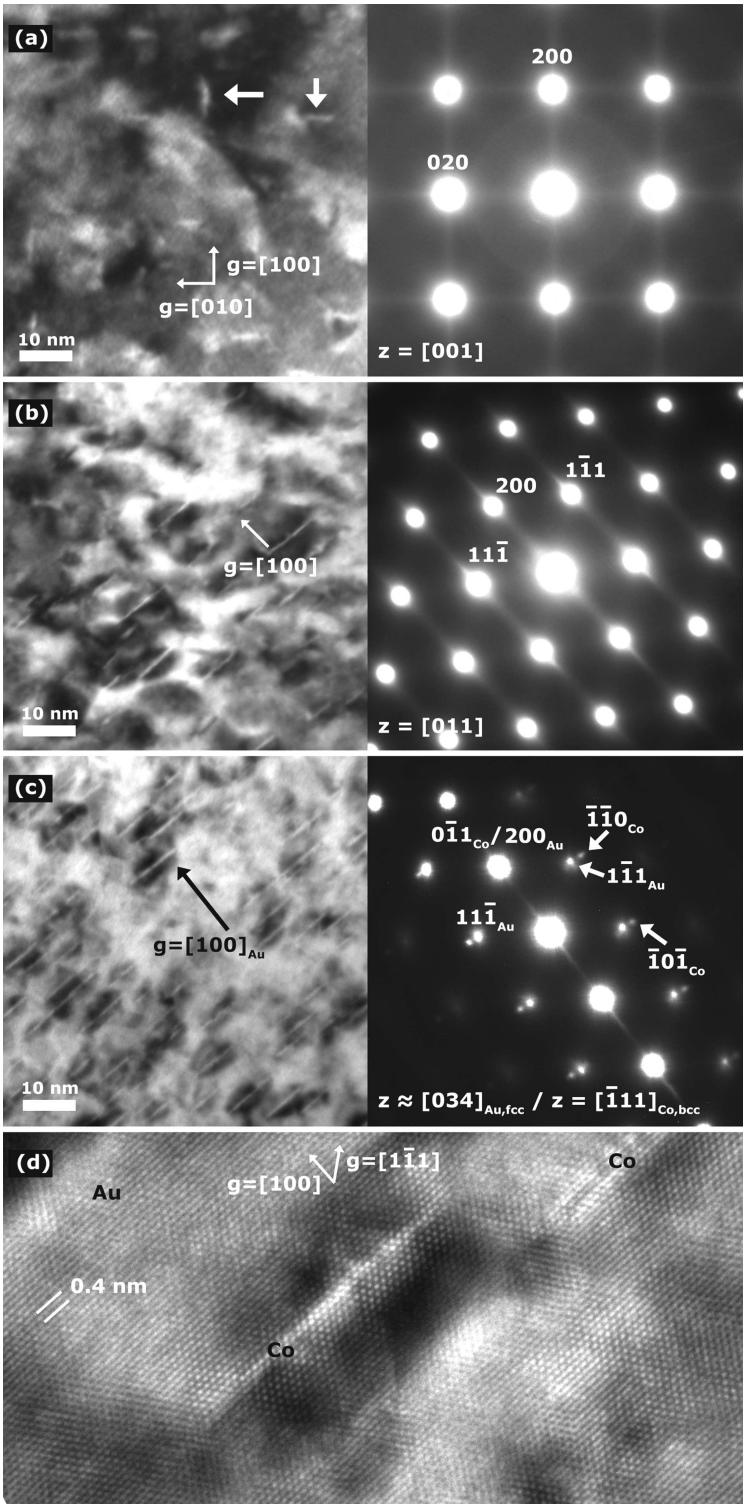

Fig. 2.2: TEM bright field and HRTEM images of $Au_{90}Co_{10}$ after isochronal annealing to 633 K with 20 K min^{-1} (cf. "b" in Fig. 2.1). (a) TEM image: [001] zone axis of the Au-rich matrix, small Co precipitates (arrows) are visible; streak formation along [100] and [010] directions in the SADP shown at the right side in (a) are due to very thin Co precipitates; extra spots due to incoherently diffracting Co precipitates are not observed. (b) TEM image: [011] zone axis of the Au-rich matrix; streak formation along [100] directions in the SADP shown at the right side in (b) (cf. (a)); extra spots due to incoherently diffracting Co precipitates are not observed. (c) Tilted by 9.7° from [011] zone axis of the Au-rich matrix towards the [001] zone axis of the Au-rich matrix: Streak formation along [100] directions in the SADP shown at the right side in (c) (cf. (a)); extra spots due to the *bcc* crystal structure of the Co precipitate plates near the {111} Au-matrix spots (see arrows in the SADP) are compatible with a [-111] zone axis for the *bcc* Co precipitates. (d) HRTEM image: [011] zone axis of Au-rich matrix; Co has precipitated as very thin coherent plates about 0.5 to 1 nm thick and 5 to 10 nm in width.

A HRTEM image, for the case of an [011] zone axis of the Au-rich matrix is shown in the Fig. 2.2d. The Co precipitate plates, two to three atomic layers thick and 5 to 10 nm long, exhibit a coherent interface along {100} lattice planes of the surrounding Au-rich matrix.

A plate-like morphology as revealed for the precipitates developing in the initial stage of precipitation has been observed before, but the crystal structure of the precipitate was not investigated [23, 24] or was assumed to be *fcc* [25].

TEM bright-field and HRTEM images and the corresponding SADP, taken after isochronal annealing up to 668 K with 20 K min^{-1} (corresponding with the shoulder at the high temperature side of the main exothermic peak (Fig. 2.1 top) and hardness decrease after peak hardness (Fig. 2.1 bottom)) are shown in Fig. 2.4.

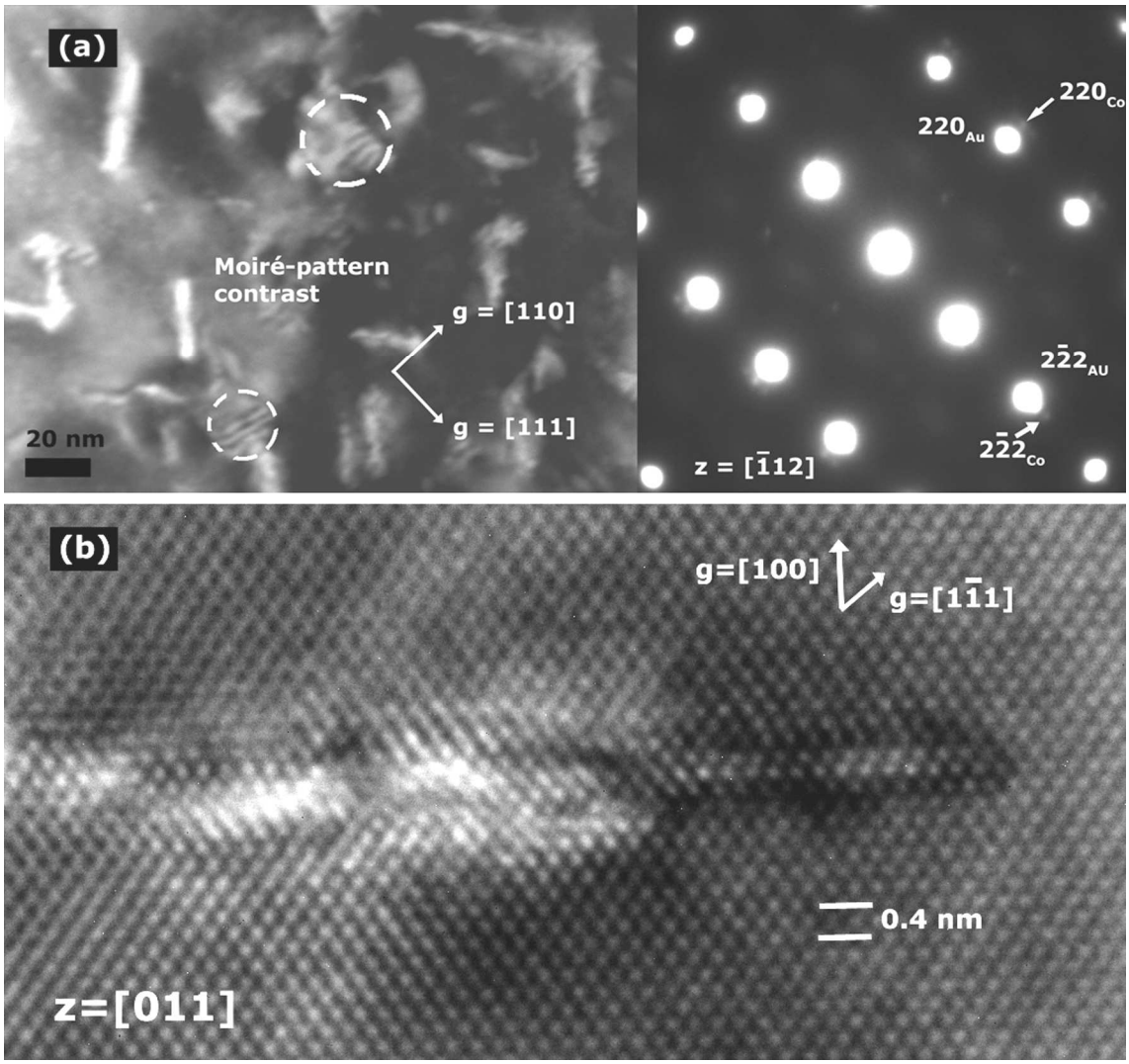

Fig. 2.3: (a) TEM bright field and (b) HRTEM images of $Au_{90}Co_{10}$ showing the precipitate morphology after isochronal annealing to 668 K with 20 K min^{-1} (cf. "c" in Fig. 2.1). (a) TEM image: [-112] zone axis of the Au matrix; the diffraction pattern shows very intensive spots of *fcc* Au and weak spots of *fcc* Co. Some of the plate-like Co precipitates show a Moiré-pattern contrast as well, indicating the beginning stage of the *bcc* to *fcc* transformation. (b) HRTEM image: [011] zone axis of the Au matrix showing the bulging of a Co plate revealing the beginning stage of the *bcc*-to-*fcc* transformation.

As compared to the stage of peak hardness with *bcc* Co precipitates, coarsening of the plate-like precipitates has occurred. Some precipitates show locally a Moiré-pattern contrast indicating a loss of coherency. The diffraction pattern ([-112] zone axis of the Au matrix) shows spots consistent with the occurrence of the *fcc* structure for the Co precipitates (a = 0.354 nm) in accordance with a $(110)_{Au,fcc}$ // $(110)_{Co,fcc}$, $[-112]_{Au,fcc}$ // $[-112]_{Co,fcc}$ (cube-on-cube) epitaxial orientation relationship between the *fcc* Au matrix and the (now) *fcc* Co precipitates. The HRTEM image presented in Fig. 2.3b ([011] zone axis of the Au matrix) shows a Co plate which has just started to bulge out in the begin of the process of transformation of *bcc* Co precipitate plate to *fcc*, more or less equiaxed Co precipitate.

A TEM image of $Au_{90}Co_{10}$ and the corresponding SADP, taken after isochronal heating to 773 K with 20 K min^{-1} (stage "d" in Fig. 2.1) are shown in Fig. 2.4. Bulky, more or less equiaxed Co precipitates are revealed by the locations of distinct Moiré-pattern contrast as a result of the presence of double diffraction spots near „*000*" (see diffraction pattern in Fig. 2.4a).

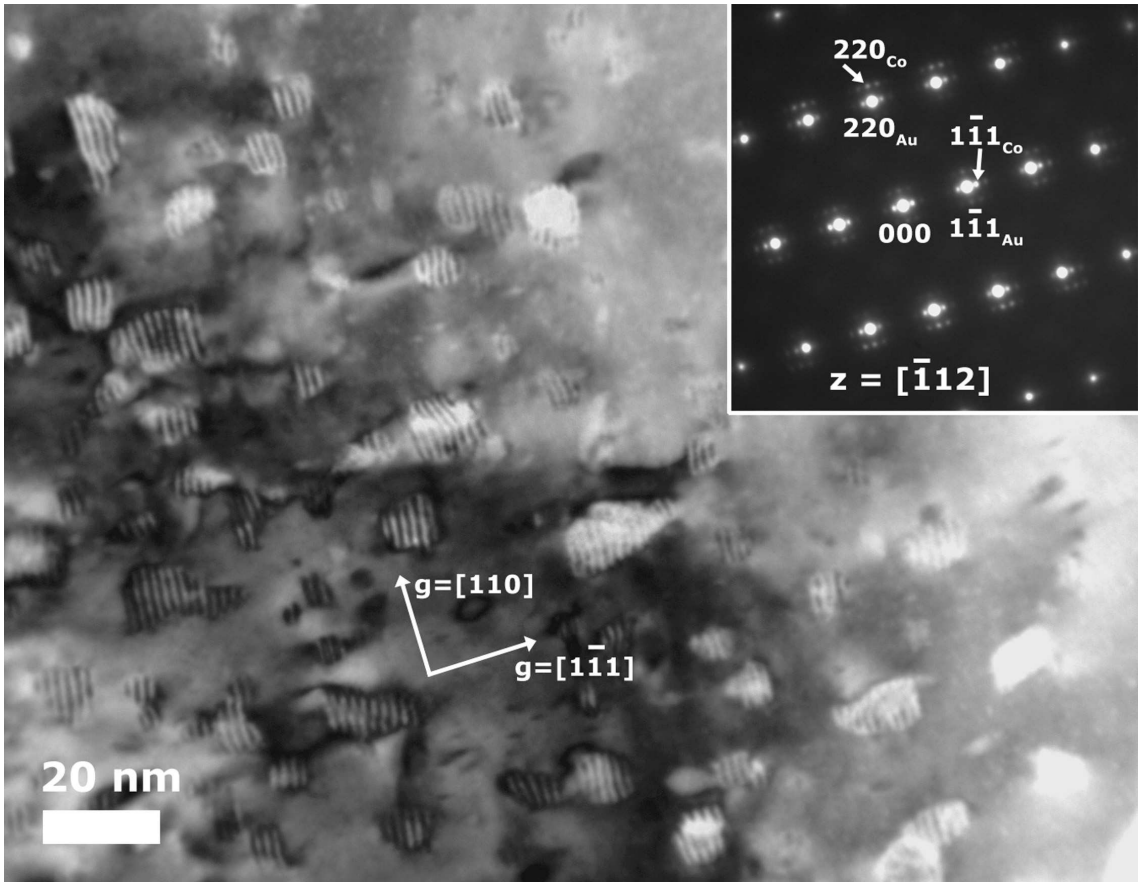

Fig. 2.4: TEM bright field image ([-112] zone axis of the Au matrix) showing the Co precipitates in $Au_{90}Co_{10}$ after isochronal heating to 773 K with 20 K min^{-1} (cf. "d" in Fig. 2.1). Moiré fringes caused by double diffraction crossing the equiaxed *fcc* Co precipitates can be seen. The diffraction pattern (top right) reveals the cube-to-cube epitaxial orientation relationship between the *fcc* Au matrix and the from *bcc* to *fcc* transformed Co precipitates. Extra spots visible around „000" in the SADP are caused by double diffraction and are responsible for the Moiré-pattern contrast in the bright field image.

A cube-on-cube, epitaxial orientation relationship between the *fcc* Co precipitate and the *fcc* Au matrix is fully compatible with the position of the reflections of Au and Co in the diffraction pattern. The residual Co concentration in the depleted Au matrix at this stage, as measured with EDX, is about 0.7 at.%, in good agreement with the published phase diagram [4]. Hence, the precipitation reaction has been completed at this stage.

2.4 Discussion

The here presented observations on the initial plate-like precipitates are fully consistent with a *bcc* crystal structure for the initial Co precipitates with a lattice parameter $a_{Co,bcc} = 0.288 \pm 0.003$ nm (derived from the measured lattice spacing for the $011_{Co,bcc}$ reflections (see above) and confirmed by tilting experiments, e. g. tilting to the [-113] zone axis of Co). This equals the value of $a_{Co,bcc} = 0.288 \pm 0.001$ nm for Co found in artificial Co/Au layer structures (cf. Refs. 19, 20). Further, the theoretical *d*-spacing for *bcc*-Co {110} is 0.204 nm, which is in agreement with the value found in this work.

A Bain-type orientation relationship [26] exists between the *bcc* Co precipitates and the *fcc* Au-rich matrix (with lattice parameter $a_{Au,fcc} = 0.408$ nm). The habit plane is $(100)_{Au,fcc} // (100)_{Co,bcc}$ (three variants). The above crystallographic data strongly suggest that the *bcc* Co precipitates are coherent with the Au-rich matrix, at least along the habit plane: The value of $a_{Co,bcc} \cdot \sqrt{2}$ closely resembles the value of $a_{Au,fcc}$. Hence, along the $\{100\}_{Au,fcc}$ habit planes no significant lattice mismatch between *bcc* Co and *fcc* Au occurs. However, perpendicular to the habit planes a mismatch of $|a_{Co,bcc} - a_{Au,fcc}|/a_{Au,fcc} \cdot 100\% = 29\%$ occurs.*

On this basis, as a consequence of the *bcc* crystal structure of the initial precipitates, the occurrence of the plate-like morphology can be understood. The absence of separate diffraction spots originating from the *bcc* Co precipitates in the SADPs with <001>-type zone axes of the Au-rich matrix and the presence of streaks in the SADPs (see Fig. 2.2) indicates that the Co plates are diffracting coherently with the Au-rich matrix (distorted by misfit strain in the plate-normal direction); see discussion for the case of plate-like VN precipitates in an α-Fe matrix in Ref. 27.

* Within the experimental accuracy (e. g. the measured spacing for $\{110\}_{Co,bcc}$ equals 0.206±0.002 nm, whereas a value of 0.204 nm is expected for *bcc* Co with $a = 0.288$ nm) only a very small tetragonal distortion might be possible. Theoretical calculations suggest that the *bcc* modification of bulk Co cannot be truly metastable [30]. For an explanation of the (meta)stability of the tiny *bcc* Co platelets in a Au-rich matrix see later in this paper.

Three sets of *bcc* Co plates occur in the Au-rich matrix according to the determined orientation relationship: Two sets ($(100)_{Au,fcc}$ // $(100)_{Co,bcc}$, $[001]_{Au,fcc}$ // $[011]_{Co,bcc}$ and $(010)_{Au,fcc}$ // $(100)_{Co,bcc}$, $[001]_{Au,fcc}$ // $[011]_{Co,bcc}$) are visible in Fig. 2.2a (electron beam direction $z = [001]_{Au,fcc}$); the third variant ($(100)_{Au,fcc}$ // $(110)_{Co,bcc}$, $[001]_{Au,fcc}$ // $[001]_{Co,bcc}$) concerns plates parallel to the TEM foil surface and is out of contrast because of the coherent nature of the plate/matrix interface. Also the tilting experiment shown in Fig. 2.2c validates the *bcc* crystal structure for the initial Co precipitates. Additional diffraction spots appear which can be indexed as $\{011\}_{Co,bcc}$, in association with the [-111] zone axis of *bcc* Co, expected for one of the above indicated three sets of precipitates after such tilting.

The natural formation of *bcc* Co, as in the course of precipitation process in a supersaturated solid solution, has not been reported before. Instead, in case of man-made multilayer/sandwich structures, Co layers could appear in *bcc* [17 – 19] or *bct* [20, 21] modifications, likely as consequence of the misfit strains imposed at the layer/layer and layer/substrate interfaces in these structures.

During the DSC measurements a small shoulder at the high temperature side of the exothermic main peak appeared, at about $T = 668$ K (Fig. 2.1). The accompanying microstructural TEM investigation (Fig. 2.3) indicates that this shoulder can be associated with the occurrence of a *bcc*→*fcc* transformation of the Co precipitates.

The equiaxed *fcc* Co particles start to develop from the initial *bcc* Co plates; no indication for a separate (*fcc* Co particle) nucleation process was obtained (Fig. 2.3a).

Such local crystal-structure transformation, i.e. without long-range diffusion of Co as would occur in a process of dissolution (of *bcc* Co) and re-precipitation (of *fcc* Co), can be realized in the present case by a Bain transformation [28] from *bcc* to *fcc* Co. This transformation involves contracting two axes within the habit plane (e.g. the axes along the [011] and [01-1] directions in the (100) habit plane) and elongating a third axis perpendicular to the habit plane (i.e. the axis along the [100] direction perpendicular to the (100) habit plane). As a consequence the here observed cube-on-cube orientation relationship is established.

After the transformation the *fcc* modification of the Co phase is preserved down to room temperature. The expected *hcp* Co phase, being stable below 695 K, was not observed in the $Au_{90}Co_{10}$ alloy investigated. This may reflect the very small difference in bulk energy of the *fcc* and *hcp* modifications [29].

The initial formation of *bcc* instead of *fcc* Co is a result of the delicate interplay, upon Co precipitation, of the Gibbs chemical energy released per unit volume precipitate and the Gibbs interface energy absorbed per unit area precipitate/matrix interface. The Gibbs chemical energy released upon precipitation of one unit volume precipitate is larger for the *fcc* modification than for the metastable *bcc* modification. However, the Gibbs interface energy per unit area interface is smaller for the coherent *bcc* precipitates than for the incoherent *fcc* precipitates. The high supersaturation, i.e. the high driving force for cobalt precipitation, in supersaturated $Au_{90}Co_{10}$ and the relatively low diffusivity of Co in the Au-rich matrix at the precipitation temperature, lead to the formation of many small precipitates and thus a high interface density (see Fig. 2.2). As a consequence, the *bcc* modification can be (thermodynamically) favored over the more stable *fcc* modification. This can be illustrated by the following estimate.

The chemical Gibbs energies released upon precipitation of *bcc* Co and *fcc* Co, in a Au – 10 at.% Co alloy at 633 K, can be assessed using the data given in Ref. 31 and 32. The misfit strain to be accommodated upon precipitation of Co can be estimated adopting elastic isotropy and a rigid matrix, according to Ref. 33. The interface energy for a (coherent) interface of *bcc* Co with the matrix and for an (incoherent) interface of *fcc* Co with the matrix can be crudely estimated as 0.2 J m^{-2} and 1.0 J m^{-2}, respectively. The dimensions of the Co precipitate platelets are taken as 10 x 10 x 1 nm^3 (see Fig. 2.2). It then follows that the net Gibbs energy released upon precipitation of *bcc* Co is about two times larger than the net Gibbs energy released upon precipitation of *fcc* Co, for the platelet dimension considered.

Upon prolonged annealing (or by increasing the temperature) growth/coarsening of the precipitate particles take place and consequently a reduction of the interface-to-volume ratio of the precipitate particles occurs. As a consequence, the Gibbs chemical energy becomes the controlling energy term and thus the transformation of the *bcc* to the *fcc* Co crystal structure is induced, albeit accompanied with an increase of the interfacial energy per unit area interface (coherent → incoherent interface).

2.5 Summary

Natural formation of, according to bulk thermodynamics, metastable *bcc* Co, with a plate-like morphology and a Bain-type orientation relationship with the Au-rich matrix, occurs in the initial stage of precipitation of supersaturated Au - 10.12 at.% Co alloys. The metastable *bcc* modification happens because the high initial interface-to-volume ratio promotes the development of precipitates of low interface energy (as holds for the *bcc* Co precipitates coherent with the Au-rich matrix). Upon continued annealing growth/coarsening of the precipitate particles takes place. Then, by a Bain transformation of metastable *bcc* Co, the *fcc* Co modification can be formed which then exhibits a cube-on-cube orientation relationship with the Au-rich matrix. The low interface-to-volume ratio for the precipitate phase in an advanced stage of annealing makes possible an overcompensation of an unfavorable interfacial energy (incoherent vs. coherent interface) by a more favorable chemical bulk energy (*fcc* vs. *bcc* modification).

References

[1] J. Bernardi et al., *Phys Status Solidi A* **147** (1995) 165.
[2] A. Hütten et al., *Scr Metall Mater* **33** (1995) 1647.
[3] J. Bernardi, A. Hütten, and G. Thomas, *J Magn Magn Mater* **157/158** (1996) 153.
[4] ASM International, Materials Park, Ohio 44073 (1996).
[5] H. Hesemann, Ph.D. thesis, University of Stuttgart, 2002.
[6] F. Sebilleau and H. Bibring, *The Mechanism of Phase Transformation in Metals* (Institute of Metals, London, 1956).
[7] J. E. Bidaux, R. Schaller, and W. Benoit, *J Phys* **46** (1985) 601.
[8] G. D. Hibbard et al., *Philos Mag* **86** (2006) 125.
[9] J. Y. Huang et al., *Nanostr Mater* **6** (1995) 723.
[10] E. A. Owen and D. M. Jones, *Proc Phys Soc London Sec B* **67** (1954) 456.
[11] H. Sato et al., *J Appl Phys* **81** (1997) 1858.
[12] J. Sort et al., *Philos Mag* **83** (2003) 439.
[13] B. Strauss et al., *Phys Rev B* **54** (1996) 6035.
[14] P. Tolédano et al., *Phys Rev B* **64** (2001) 144104.
[15] J.C. Zhao and M.R. Notis, *Scr Metall Mater* **32** (1995) 1671.
[16] A.R. Trojano and J.L. Tokich, *Trans Am Inst Min Metall Eng* **175** (1948) 728.
[17] G.A. Prinz, *Phys Rev Lett* **54** (1985) 1051.
[18] J. Dekoster et al., *J Magn Magn Mater* **121** (1993) 69.
[19] L. J. Wu et al., *J Phys Condes Matter* **5** (1993) 6515.
[20] S. K. Kim et al., *Phys Rev B* **54** (1996) 2184.
[21] N. Spiridis et al., *Surf Sci* **566** (2004) 272.
[22] G. W. H. Höhne, W. F. Hemminger, and H.-J. Flammersheim, *Differential Scanning Calorimetry* (Springer-Verlag, Berlin, Heidelberg, 2003, 2nd edition).
[23] C. G. Lee et al., *IEEE Trans Magn* **35** (1999) 2856.
[24] V. Y. Zenou et al., *J Mat Sci* **38** (2003) 2679.
[25] N. Kataoka et al., *J Magn Magn Mater* **140** (1995) 621.
[26] E.C. Bain, *Trans Metall Soc AIME* **70** (1924) 25.
[27] N. E. V. Vives Díaz et al., *Acta Mater* **56** (2008) 4137.
[28] J. Rifkin, *Philos Mag A* **49** (1984) L31.
[29] A. Fernandez Guillermet, *Int J Thermophys* **8** (1987) 481.
[30] A. Y. Liu and J. Singh, *J Appl Phys* **73** (1993) 6189.
[31] H. Okamoto et al., *Bulletin of Alloy Phase Diagrams* **6** (1985) 449.
[32] A. T. Dinsdale, *Calphad* **15** (1991) 317.
[33] J. D. Eshelby, *Roy Soc Proc London A* **241** (1957) 376.

3 Precipitation of Co from Supersaturated $Au_{90}Co_{10}$: Microstructure and Kinetics

R. Bauer, E. Bischoff and E. J. Mittemeijer

Abstract

The kinetics of the precipitation of Co from a supersaturated solid solution of Au - 10.12 at. % Co was investigated by differential scanning calorimetry (DSC) upon isothermal annealing at temperatures in the range from 567 K to 612 K and upon isochronal annealing at heating rates between 5 K min^{-1} and 40 K min^{-1}. The microstructural evolution during the course of precipitation was traced by (high-resolution) transmission electron microscopy [(HR)TEM], scanning electron microscopy (SEM), X-ray diffraction (XRD), and hardness measurements. First the exothermic formation of 0.5 - 1 nm thin platelike *bcc* Co precipitates takes place parallel to {100} habit planes of the Au-matrix. Upon continued annealing equiaxed *fcc* Co particles in epitaxial orientation with the Au lattice occur by a Bain-type transformation of the Co particles from the *bcc* to the *fcc* lattice structure associated with loss of coherency. Fitting of a modular model of transformation kinetics (Liu et al., *Int Mat Rev*, **52** (2007) 193) simultaneously to the first peak of all isothermal DSC runs and simultaneously to the first peak of all isochronal DSC runs demonstrated that the nucleation of *bcc* Co plates is governed by site saturation in case of isothermal annealing and continuous nucleation in case of isochronal annealing and by interface-controlled growth for both isothermal and isochronal annealing. The activation energy for growth is remarkably small due to the presence of quenched-in vacancies. Recovery prior to precipitation leads to a change of the nucleation mechanism from site saturation to continuous nucleation as well as an increase of the activation energy for growth.

3.1 Introduction

Au-Co alloy is of great interest as dental casting alloy, as contact material in microelectronic systems and as a material of giant magnetoresistance. The Au-rich phase exhibits a face-centered cubic (*fcc*) crystal structure. The Co-rich phase can experience an allotropic phase transformation at $T_a = 690 \pm 7$ K, [1] with a hexagonal close-packed (*hcp*) crystal structure below T_a and a *fcc* crystal structure above T_a. Below T_a the solubility of Co in *fcc* Au less is than 0.2 at. % and the solubility of Au in *hcp* Co is less than 0.05 at. % [2].

The microstructural evolution during the precipitation of Co in Au-rich Au-Co solid solutions of varying Co content was investigated previously by several groups. After annealing in a temperature range from 743 K to 838 K of initially homogeneous and quenched Au-Co alloys, the formation of disc-shaped Co precipitates claimed to be of *fcc* crystal structure was found with the platelets aligned along $\{001\}_{Au}$ planes in the majority of cases [3 - 9], but also along $\{111\}_{Au}$ planes [10].

Recently it was proven by experiment that the initially formed disc-shaped Co precipitates exhibit a *bcc* crystal structure [11].

Very little information on the kinetics of the Co precipitation reaction is available. The classical Johnson-Mehl-Avrami approach was applied [12], which can only yield an overall, effective activation energy and does not allow identification of nucleation and growth mechanisms.

The present project is devoted to arriving at an understanding of the microstructural evolution and the kinetics of the separate nucleation and growth modes during the early stage of the precipitation of Co in Au-rich Au-Co alloy. Such work is deemed timely in view of (i) the recent recognition that the initial precipitates have a *bcc* (rather than a *fcc*) crystal structure [11], and (ii) the recent availability of a modular model for transformation kinetics that is much less constrained than the classical JMA approach [13, 14]. The kinetics of the Co precipitation process in a supersaturated solid solution of Au - 10.12 at. % Co has been deduced from both isothermal and isochronal annealing experiments performed in a differential scanning calorimeter (DSC). The microstructural evolution upon both isothermal and isochronal annealing has been followed by (high resolution) transmission electron microscopy [(HR)TEM], scanning electron microscopy (SEM), X-ray diffractometry (XRD), and hardness measurements.

3.2 Theoretical Considerations

3.2.1 Thermodynamics

3.2.1.1 Transformation Enthalpy

In order to calculate the driving force for decomposition, ΔG_{decomp}, involving the precipitation of Co from the supersaturated Au-Co solid solution, the initial and end states have to be defined. The initial state is the solid solution of Au and Co at the beginning of the precipitation reaction in supersaturated (undercooled) state. The end state corresponds with completed decomposition of the solid solution of Au and Co into its (nearly) pure components. Hence, the end state can be treated as a mechanical mixture. Thus:

$$\Delta H_{\text{decomp}} = H_{\text{mechanical mixture}} - H_{\text{solid solution}} = -\Delta H_{\text{mix}} \tag{3.1}$$

where ΔH_{mix} is the enthalpy of mixing in the solid solution. The solid solution of Au and Co can be described by the regular solution model plus an additive magnetic (excess) energy term accounting for the Gibbs energy difference between the para- and ferromagnetic states [2]. Hence:

$$\Delta H_{\text{mix}}\left(x_{\text{Co}}, T\right) = \Omega\left(x_{\text{Co}}, T\right) \cdot x_{\text{Co}} \cdot \left(1 - x_{\text{Co}}\right) \tag{3.2}$$

with x_{Co} as the atomic fraction of solute, T as the absolute temperature and $\Omega(x_{Co},T)$ as the interaction parameter. From Eqs. (3.1) and (3.2) it follows

$$\Delta H_{\text{decomp}} = -\Omega \cdot \left(1 - x_{\text{Co}}\right) \cdot x_{\text{Co}}\,. \tag{3.3}$$

Alloy systems with a decomposition tendency, like the Au-Co alloy system, possess an interaction parameter $\Omega > 0$. The interaction parameter Ω is a function of the composition and temperature; the value $\Omega = 30293 \pm 4871$ J mol^{-1} [6] pertains to the temperature range in this work. It follows for the alloy Au - 10.12 at. % Co used in this work: $\Delta H_{\text{decomp}} = -2.73 \pm 0.44$ kJ mol^{-1} (note: the total heat released is given by $-\Delta H_{\text{decomp}}$).

3.2.1.2 Gibbs Energy Barrier for Nucleation

An assessment of the energy barrier for homogeneous and heterogeneous nucleation of Co particles from supersaturated Au-Co solid solution, exhibiting either a coherent or an incoherent interface, can be made applying classical nucleation theory [14, 15]. The formation of a particle of a new phase is associated with release of chemical Gibbs energy ΔG_v (per unit volume), and an energy uptake owing to the creation of a particle/matrix interface with the energy σ (per unit area) and a (misfit-)strain energy ΔG_S (per unit volume). The act of nucleation involves the transition from a particle of subcritical size (an "embryo") to a particle of supercritical size, which, for the particle, leads to a release of energy. Homogeneous and heterogeneous nucleation can be distinguished.

For homogeneous formation of a spherical nucleus the Gibbs energy barrier, ΔG^*, can be expressed as

$$\Delta G^*_{\text{hom}} = \frac{16\pi\sigma^3 V_m^2}{3\left(\Delta G_V - \Delta G_S\right)^2} \tag{3.4}$$

with the molar volume of the alloy V_m. The interface energy σ for a coherent and for an incoherent interface of *fcc* Co with the matrix can be estimated as 0.25±0.05 J m^{-2} [6] and 1 J m^{-2}, respectively. The chemical Gibbs energies, ΔG_v, per unit volume released upon precipitation of *fcc* Co, for the Au - 10.12 at.% Co solid solution of this study, can be assessed using the data given in Ref. 2. The misfit strain to be accommodated upon precipitation of Co can be estimated adopting elastic isotropy and a rigid inclusion, according to Ref. 17 in case of coherency and according to Ref. 18 in case of incoherency.

Heterogeneous nucleation takes place at defects like vacancies, dislocations and grain boundaries, thereby releasing corresponding defect energy. In case of heterogeneous nucleation at grain boundaries with a contact angle, θ, between the precipitate-matrix interface and the grain boundary, the Gibbs energy barrier for heterogeneous nucleation according to Ref. 15 is given as

$$\Delta G^*_{\text{het}} = \Delta G^*_{\text{hom}} \frac{2 - 3\cos\theta + \cos^3\theta}{2}. \tag{3.5}$$

For the Au - 10.12 at. % Co solid solution of this study, the Gibbs energy barrier for heterogeneous nucleation of incoherent particles at grain boundaries is found to be smaller than for homogeneous nucleation of coherent or incoherent spherical Co particles within the Au-rich matrix (see Fig. 3.1). The whether or not occurrence of a Gibbs energy barrier for heterogeneous nucleation on dislocations depends on the value of a parameter, α, [21] that is calculated for screw and edge dislocations as follows

$$\alpha_{screw} = \frac{-\Delta G_v}{\pi V_m \sigma^2} \cdot \frac{G_{Au} b^2}{4\pi} \tag{3.6a}$$

$$\alpha_{edge} = \frac{\alpha_{screw}}{(1-\nu_{Au})} \tag{3.6b}$$

with the Burgers vector b (= $a_{Au}/\sqrt{2}$) and the shear modulus G_{Au} of Au. If $\alpha > 1$ no energy barrier for nucleation occurs. For $0 < \alpha < 1$ a finite energy barrier for nucleation does occur. The precipitation of Co in this work occurs in a temperature range where $\alpha > 1$ and, hence, no Gibbs energy barrier is predicted for heterogeneous nucleation at edge or screw dislocations (see Fig. 3.1) (for a detailed discussion of such heterogeneous nucleation, see Ref. 22).

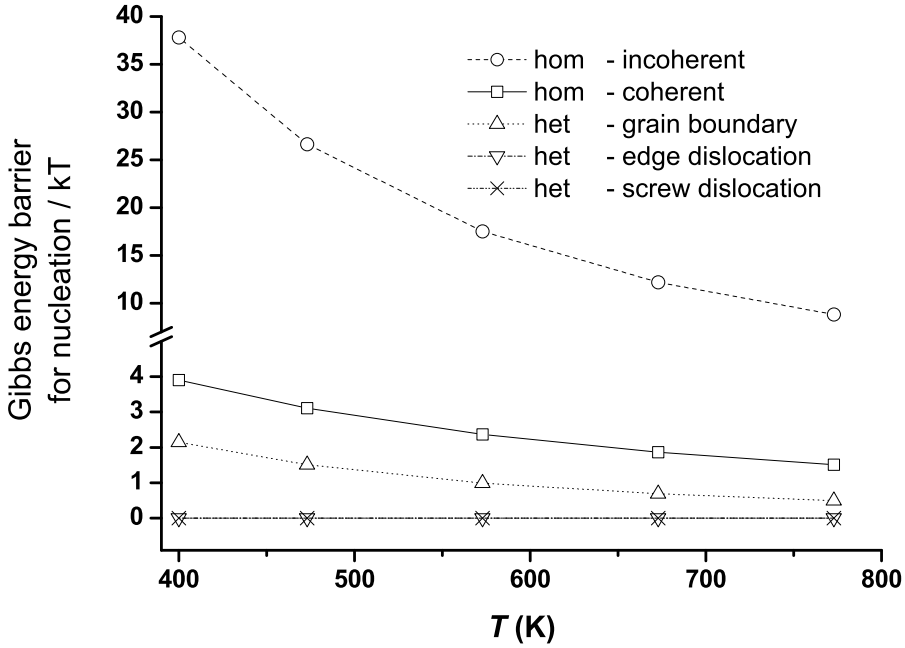

Fig. 3.1: Gibbs energy barriers for nucleation of Co particles in a Au – 10.12 at. % Co solid solution. The Gibbs energies have been normalized by division by the factor kT (k: Boltzmann constant). Cases of homogeneous (*hom*) nucleation and of heterogeneous (*het*) nucleation of disc shaped platelets at grain boundaries and/or at dislocations are shown as function of temperature (using $\sigma_{coherent}$ = 0.25 J mol^{-1} and $\sigma_{incoherent}$ = 1 J mol^{-1}). The temperature range (400 K to 773 K) has been chosen in accordance with the experiments performed in this work. In case of heterogeneous nucleation at dislocations no energy barrier for nucleation occurs. In case of heterogeneous nucleation at grain boundaries with a contact angle $\theta = 37°$ as reported in Ref. 6 for precipitation of Co in a Au – 6.5 at. % Co alloy, a nucleation barrier in the range from 2.1 kT to 0.5 kT for the formation of incoherent precipitates must be overcome, which is much smaller than the Gibbs energy barrier for homogenous nucleation of both, coherent (3.9 kT - 1.5 kT) and incoherent (37.8 kT - 8.8 kT) particles.

3.2.2 Transformation Kinetics; The Modular Model

Solid state phase transformations can generally be considered as the outcome of three (overlapping) mechanisms: Nucleation, growth and impingement. This leads to a modular approach for modelling the transformation kinetics, for both isothermally and isochronally (i. e. with constant heating / cooling rate) conducted experiments, as described in Refs. 13 and 14 and applied successfully in, for example, Refs. 23 and 24. Only in special cases of nucleation, growth and impingement an analytical solution, as the Johnson-Mehl-Avrami (JMA) equation, is available [14, 15]. Generally the model can be applied in a numerical way to fit experimental data and thereby exhibits greatest flexibility concerning the possible description of phase transformations.

3.2.2.1 Extended Transformed Fraction

If all nuclei are supposed to form and grow into an infinitely large parent phase, in the absence of other product particles, the volume transformed within a time range dt is obtained by accumulation of the volume increases of all particles nucleated at times $\tau < t$ and grown from t to t + dt. The thus calculated total product volume at time t is called the extended volume, i. e. here the extended precipitate volume $V_{\mathrm{p,e}}$. In case of a precipitation reaction the maximal precipitate volume reached, at the end of the precipitation reaction, is denoted $V_{\mathrm{p,end}}$. The so-called extended precipitate volume fraction, $x_{\mathrm{e}} = V_{\mathrm{p,e}}/V_{\mathrm{p,end}}$, thus is given by:

$$x_{\mathrm{p,e}} = \frac{V_{\mathrm{p,e}}}{V_{\mathrm{p,end}}} = \frac{V}{V_{\mathrm{p,end}}} \int_0^t \dot{N}\left(T\left(\tau\right)\right) Y\left(T\left(t\right)\right) d\tau \tag{3.7}$$

where V is the specimen volume, $\dot{N}$ is the nucleation rate of product-phase particles per unit volume and per unit time and Y is the volume of a particle at time t nucleated at time τ.

For a wide range of nucleation and growth modes the following analytical expression for $x_{\mathrm{p,e}}$ can be given for isothermally, Eq. (3.8), and isochronally, Eq. (3.9), conducted transformations [14]:

$$x_e = \frac{V}{V_{\mathrm{p,end}}} K_0^n t^n \exp\left(-\frac{nQ}{RT}\right) \tag{3.8}$$

$$x_e = \frac{V}{V_{\mathrm{p,end}}} K_0^n \left(\int_0^t \exp\left(-\frac{nQ}{RT(t)} \right) dt \right) \cong \frac{V}{V_{\mathrm{p,end}}} \left(\frac{K_0}{Q} \right)^n \left(\frac{RT^2}{\Phi} \right)^n \exp\left(-\frac{nQ}{RT(t)} \right) \quad (3.9)^*$$

with the growth exponent n and the effective activation energy Q:

$$Q = \frac{(d/m)Q_G + (n - d/m)Q_N}{n}. \quad (3.10)$$

The overall activation energy Q in Eq. (3.10) represents a weighted sum of the activation energies for nucleation Q_N and growth Q_G, with the ratio of the growth dimension d (1, 2 or 3) and the growth mode m ($m = 1$ in case of linear growth (i. e. for isothermal transformations the transformed volume grows proportional with t; this usually (but not always; see what follows in this paper) corresponds with interface controlled growth); $m = 2$ in case of "parabolic", (diffusion controlled) growth (i. e. for isothermal transformations the transformed volume grows proportional with $t^{1/2}$)) as well as the growth exponent n as weighting factors. The kinetic parameters in Eqs. (3.8) and (3.9) are K_0, Q and n, which in principle can be time (isothermal annealing) or temperature (isochronal annealing) dependent. Expressions for K_0, Q and n for a wide range of nucleation and growth modes, including those relevant to the present paper, have been listed in Tables 1 to 3 of Ref. 14.

3.2.2.2 Impingement Modes

Impingement involves that no product phase particles can nucleate in already transformed volume ("hard" impingement) and accounts for the effect of solute depletion around product particles ("soft" impingement). In order to derive the real transformed fraction, f, from the extended fraction, $x_{\mathrm{p,e}}$, a so-called impingement correction has to be incorporated. Obviously interface-controlled growth is associated with hard impingement, whereas diffusion-controlled growth can lead to soft impingement. Further, the nucleus/particle distribution (random or not) and possible anisotropy of growth can drastically effect the impingement.

In case of randomly dispersed nuclei throughout the total volume of the specimen and isotropically growing particles, the degree of transformation f is given by [14]

$$f = 1 - \exp\left(-x_{\mathrm{p,e}}\right). \quad (3.11)$$

---

* Note that Eqs. (3.8) and (3.9) differ from Eqs. (30) and (31) in Ref. 15: because of the different normalization of f (and $x_{\mathrm{p,e}}$), i. e. with respect to $V_{\mathrm{p,end}}$ (not V) in the current paper, the fraction $V/V_{\mathrm{p,end}}$ appears in Eqs. (3.8) and (3.9). Equation (3.9) differs in one further aspect from Eq. (31) in Ref. 15: the factor K_0 in Eq. (31) in Ref. 15 is equal to K_0/Q in the present Eq. (3.9), because in Ref. 15 the factor $1/Q$ has been incorporated in the expressions for K_0 given for isochronal annealing in Tables 1 to 3 in Ref. 15.

It was shown in Refs. 14 and 23 that JMA-like equations are obtained from Eq. (3.11) for a wide range of nucleation and growth modes. Indeed, a lot of experimental kinetic data on phase transformations have been interpreted on JMA basis. However, in many cases no good description for the entire transformation is obtained [27] and fitting with a JMA-like equation has to be restricted to the first part of the transformation [15, 28]. This hints at the inappropriateness of the correction for impingement given by Eq. (3.11).

To account for growth anisotropy (relevant to many solid-solid phase transformations) the following impingement correction has been proposed [29 - 32]

$$f = 1 - \left[1 + (\xi - 1)\, x_{\mathrm{p,e}}\right]^{-1/(\xi - 1)} \tag{3.12}$$

with the impingement parameter $\xi > 1$. For the case $\xi \to 1$ Eq. (3.12) approaches Eq. (3.11).

Equations (3.11) and (3.12) have originally been given for hard impingement. A rigorous treatment of soft impingement does not exist. It can be inferred [33] that Eq. (3.11) also halts for soft impingement (in case of randomly dispersed nuclei and isotropic growth). This may be understood as that for the case of "soft impingement" each precipitate/product particle is supposed to be surrounded, effectively, by an outer solute depleted shell of size such that upon completed precipitation all precipitate particles with their surrounding solute depleted shells occupy the whole volume of the specimen. Similarly it can be expected that in case of anisotropic growth Eq. (3.12) can also be used as a viable approximation for soft impingement as shown in Refs. 27, 30, 31 and 32.

3.2.2.3 Determination of Kinetic Parameters

After having chosen specific nucleation, growth and impingement mechanisms, fitting of the corresponding, specific version of the modular transformation model, to experimental, e. g. transformation-rate, data, in principle leads to determination of the kinetic (fit) parameters, including, Q_N and Q_G, provided that the fit parameters are independent (see Ref. 14).

Independent of adopting specific models for nucleation and growth, the overall, effective activation energy, Q, and the growth parameter, n, can be determined for phase transformations subjected to isothermal or isochronal heat treatments according to methods and procedures presented and discussed in Refs. 14 and 25. The basic requirement for these methods is that the nucleation and growth modes are thermally activated according to an Arrhenius-type equation. This holds remote from equilibrium (high supersaturation) as is the case for the present experiments.

3.3 Experimental

3.3.1 Alloy Production

An ingot of Au - 10 at. % Co alloy was produced by melting appropriate amounts of Au (99.95 at. %) and Co (99.995 at. %) in an inductive furnace. The ingot was homogenized at 1233 K for 236 h in an argon atmosphere and quenched into ice water. Disc shaped specimens were produced by hammering the cylindrical ingot to a diameter of 5 mm and cutting pieces with a thickness of 500 µm. These specimens were recrystallized and solution-annealed at 1233 K for 24 h and quenched into ice water. Then the composition was determined by Inductively Coupled Plasma – Optical Emission Spectrometry (ICP-OES) to be Au - 10.12±0.13 at. % Co.

Next, both sides of the specimen discs were prepared by grinding with SiC-paper and subsequently polishing using diamond paste down to 0.25 µm. All specimens were then cleaned ultrasonically in isopropyl.

3.3.2 Differential Scanning Calorimetry

The isothermal and isochronal annealings were carried out with a power-compensated differential scanning calorimeter (DSC) Pyris1 from Perkin Elmer. The temperature and heat flow were calibrated by using the melting temperature and the heat of fusion of In, Pb and Zn, respectively, measured for each heating rate used (extrapolated to 0 K min^{-1} for isothermal annealing). Aluminum was used as pan material for the specimen and reference container, in which the reference pan contained two Al covers, in order to obtain a heat capacity similar to that of the specimen. Pure argon gas with a constant flow was used as protective gas atmosphere.

The isochronal anneals were conducted with various heating rates in the range of 5 K min^{-1} to 40 K min^{-1}. The isothermal anneals were conducted in the range of 567 K to 612 K (reached after rapid heating at a heating rate of about 500 K min^{-1}). The specimens were subjected to two successive, identical anneals. In the first run an exothermic signal due to the precipitation of Co was measured. The second run showed no such signal and served as measurement of the baseline, representing the thermal properties of the device, pans and equilibrated specimens. Upon the precipitation of cobalt (in the first run) no change of the heat capacity was observed, opposite to results obtained for the crystallization of amorphous alloys (e.g. [24]). Therefore, the two consecutive runs are congruent in the pre- and post-effect range.

After baseline correction of the measured DSC curves (see above), the degree of transformation, *f*, was determined from the resulting differential enthalpy signal dΔH/dt as follows

$$f(t) = \frac{\Delta H(t)}{\Delta H_{tot}} \tag{3.13}$$

with the cumulative transfromation enthalpy $\Delta H(t)$ calculated by integration of the DSC signal, dΔH/dt, leading also to a value for the total transformation enthalpy ΔH_{tot}.

Specimens for the analysis of the phase composition, microstructural evolution and hardness were subjected to isochronal annealing with a heating rate of 20 K min^{-1} starting from room temperature. Such DSC runs were interrupted at 550 K, 633 K, 668 K and 773 K, respectively, by fast cooling of the specimen at a rate of 180 K min^{-1}.

3.3.3 X-Ray Diffraction

X-ray diffraction measurements were performed employing a Bruker D8 Discover diffractometer operating in parallel-beam geometry equipped with an X-ray lens in the incident beam, a parallel-plate collimator in the diffracted beam and an energy-dispersive detector selecting Cu Kα radiation. The 2θ-range of 10°-140° was measured with a step size of 0.04° and a time per step of 7s.

3.3.4 Hardness Measurement

The Vickers microhardness was measured in the center of the grains, observed in a specimen section using a micro-hardness tester Leica VMHT Mot applying a load of 1 gf for 10 s. At least 25 indentations per specimen were performed for the calculation of a mean microhardness value. The measurements were performed on mechanically polished specimens to avoid the influence of any surface roughness on the hardness measurements. The grain centers used as locations for hardness measurement had been marked by indentations applying a high load of 500 gf at the etched specimen surface before the mechanical polishing.

The Vickers micro hardness was measured using a micro-hardness tester Leica VMHT Mot applying a load of 1 gf for 10 s. The microstructure of these specimens was investigated by (HR)TEM.

3.3.5 Electron Microscopy – SEM, TEM and HRTEM

The microstructures of specimens at different stages of precipitation were analysed using electron-microscopical techniques. Specimens for (HR)TEM were prepared by cutting out a stripe from the disc, clamping and glueing it between two Al blades fixed by a Cu ring and cutting out a thin disc. After dimpling this disc to a thickness of 100 µm, ion thinning was applied using a Gatan precision ion polishing system (PIPS) with a voltage of 3 kV, a current of 10 µA, an incident angle of 9° and a LN_2 cooling unit. TEM was performed using a Philips CM200 instrument operating at 200 kV. HRTEM was performed using a Jeol 4000FX instrument operating at 400 kV. The composition of the Au matrix, in-between Co precipitates, during and after completed precipitation was determined by energy-dispersive X-ray (EDX) microanalysis applied in a VG501 STEM instrument operating at 100 kV.

Scanning electron microscopy (SEM) was performed using a Jeol JSM 6400 SEM. The specimen discs for SEM (the same as used for DSC) were prepared after the DSC treatment by grinding the disc surfaces with SiC-paper and subsequent polishing using diamond paste down to 0.25 µm and etching with aqua regia for 30 s.

3.4 Results and Evaluation

3.4.1 Differential Scanning Calorimetry

A baseline corrected (see section 3.3.2) isochronal DSC scan of supersaturated Au - 10.12 at. % Co at a heating rate of 20 K min^{-1} is shown, exemplarily for all heating rates used, in Fig. 3.2. The small exothermic valley-like signal, before the appearance of the strong exothermic signal, is ascribed to relaxation of quenched-in strains [10]. This small exothermic relaxation peak, exhibiting a heat release of about -80 J mol^{-1} for all heating rates applied, has been substituted by a zero heat signal in the following graphs of DSC results (see Fig. 3.3), because, as shown in section 3.3.4, no precipitation (related effect) takes place during relaxation.

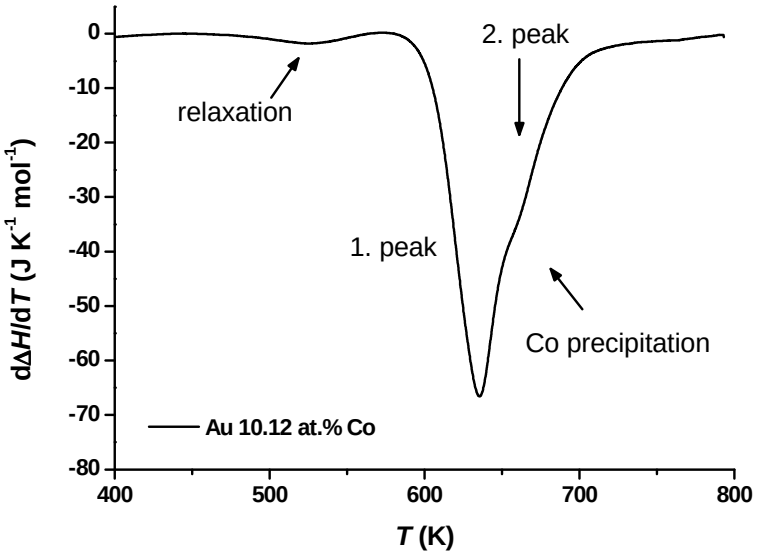

Fig. 3.2: Isochronal baseline corrected DSC scan of supersaturated Au - 10.12 at. % Co measured at a heating rate of 20 K min^{-1}.

The strong exothermic peak of the baseline corrected isochronal scans for the precipitation of Co in supersaturated Au - 10.12 at. % Co is shown in Fig. 3.3 for the heating rates of 5 K min^{-1}, 10 K min^{-1}, 20 K min^{-1} and 40 K min^{-1}. Evidently, the strong exothermic peak consists actually of two overlapping peaks: See shoulder at high temperature side. With increasing heating rate the peaks broaden and the shoulder at the high-temperature side becomes less distinct.

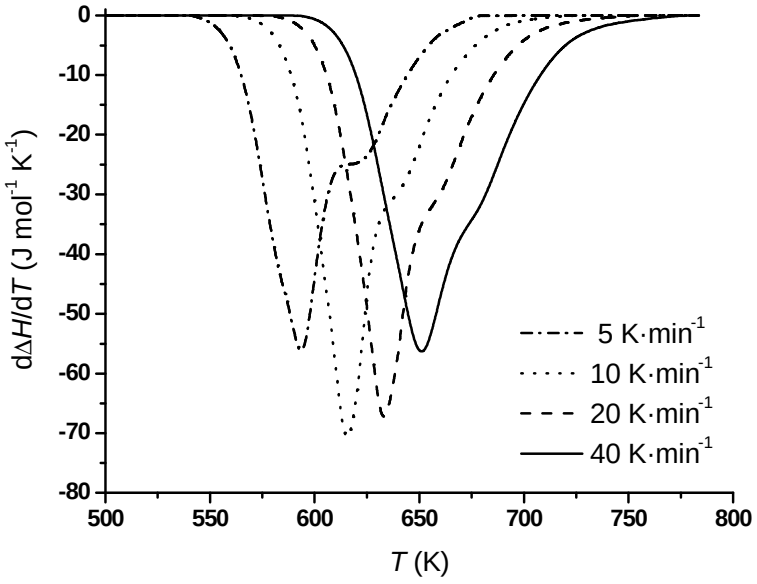

Fig. 3.3: Isochronal baseline corrected DSC-scans of supersaturated Au – 10.12 at. % Co measured at varying heating rates as indicated.

The measured values for the total precipitation, transformation enthalpy ΔH_{tot} have been listed in Table 3.1 for the heating rates applied; the mean value is about -2.8 kJ mol^{-1}.

Table 3.1: Total transformation enthalpy, ΔH_{tot}, for supersaturated Au - 10.12 at. % Co as measured by *isochronal* annealing at different heating rates as indicated.

dT/dt (K min^{-1})	ΔH_{tot} (J mol^{-1})
5	-2582
10	-2800
20	-2825
40	-3054

Isothermal annealing of initially supersaturated Au - 10.12 at. % Co was performed in the temperature range from 567 K to 612 K. The baseline corrected isothermal DSC scans are shown in Fig. 3.4.

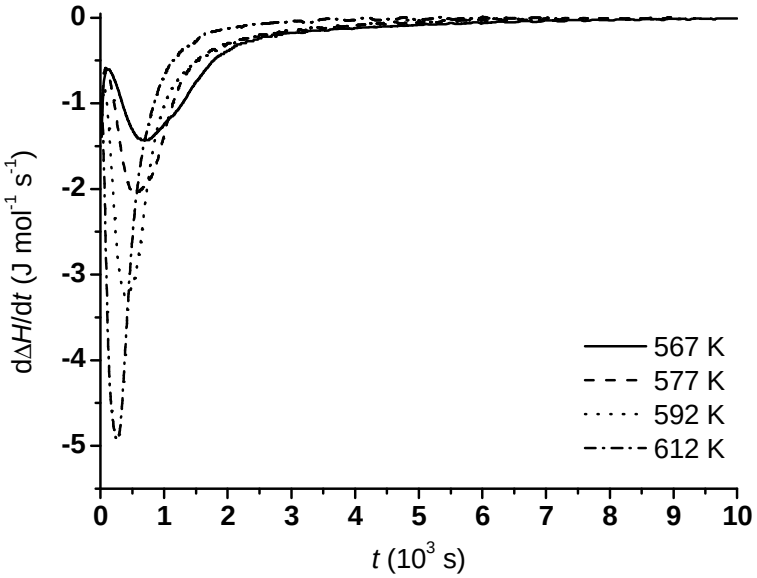

Fig. 3.4: Isothermal DSC-scans of supersaturated Au - 10.12 at. % Co recorded at different annealing temperatures as indicated.

The measured values for the total precipitation, transformation enthalpy ΔH_{tot} have been listed in Table 3.2 for the isothermal annealing temperature applied. The measured values of ΔH_{tot} yield a mean value of about -2.8 kJ mol^{-1}, as for the isochronal anneals (cf. Table 3.1). The peak maximum in the isothermal scans decreases with decreasing isothermal annealing temperature, balanced by an increase of the peak width.

Table 3.2: Total transformation enthalpy, ΔH_{tot}, for supersaturated Au - 10.12 at. % Co as measured by *isothermal* annealing at different temperature as indicated.

T (K)	ΔH_{tot} (J mol^{-1})
567	-2522
577	-2612
592	-3107
612	-2934

The variation of the measured total transformation enthalpy values (cf. Table 3.1 and Table 3.2) and the peak maximum heights (see Fig. 3.3) can result from slight microstructural differences between the specimens, e. g. different amounts of strains induced upon quenching [10] and due to measurement errors in particular at low heating rate and at low isothermal temperature (small signals).

The transformation enthalpy predicted for the precipitation of Co by application of the regular solution model equals -2.73±0.44 kJ mol^{-1} (see section 3.2.1.1). This predicted value very well agrees with the transformation enthalpies as determined in this work for both the isothermal and the isochronal annealing experiments at varying annealing temperatures and heating rates, respectively (see above).

In order to follow the evolution of the microstructure during the precipitation, isochronal DSC scans, taken from different freshly quenched specimens, at a heating rate of 20 K min^{-1}, were interrupted at 550 K, 633 K, 668 K and 773 K as presented in Fig. 3.5 (see section 3.3.2).

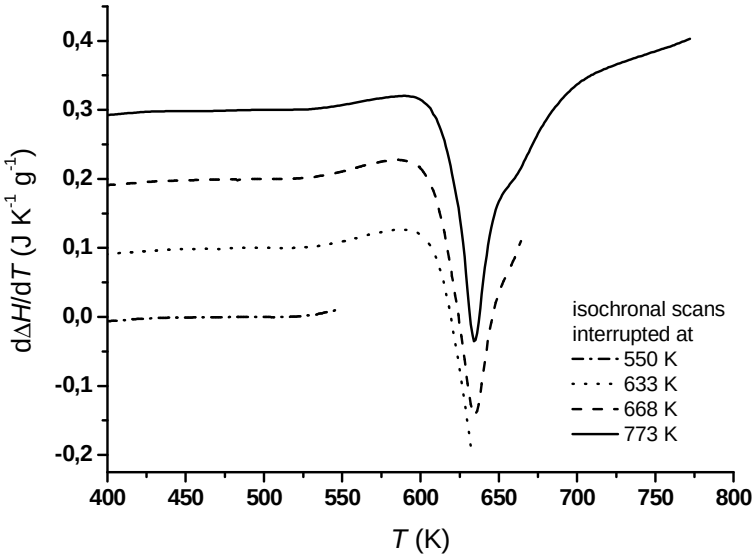

Fig. 3.5: Isochronal DSC scans of four supersaturated Au - 10.12 at. % Co specimens measured with a heating rate of 20 K min^{-1} and interrupted at defined temperatures.

3.4.2 X-Ray Diffractometry

XRD diffractograms of as-quenched and isochronally annealed (up to a specified temperature) initially supersaturated Au - 10.12 at. % Co solid solution are shown in Fig. 3.6. Card 65 - 2870 for Au of the powder diffraction file [34] was used for indexing the Bragg peaks of Au. In all XRD diffractograms only Bragg reflections of the Au-rich phase and no Co reflections were found.

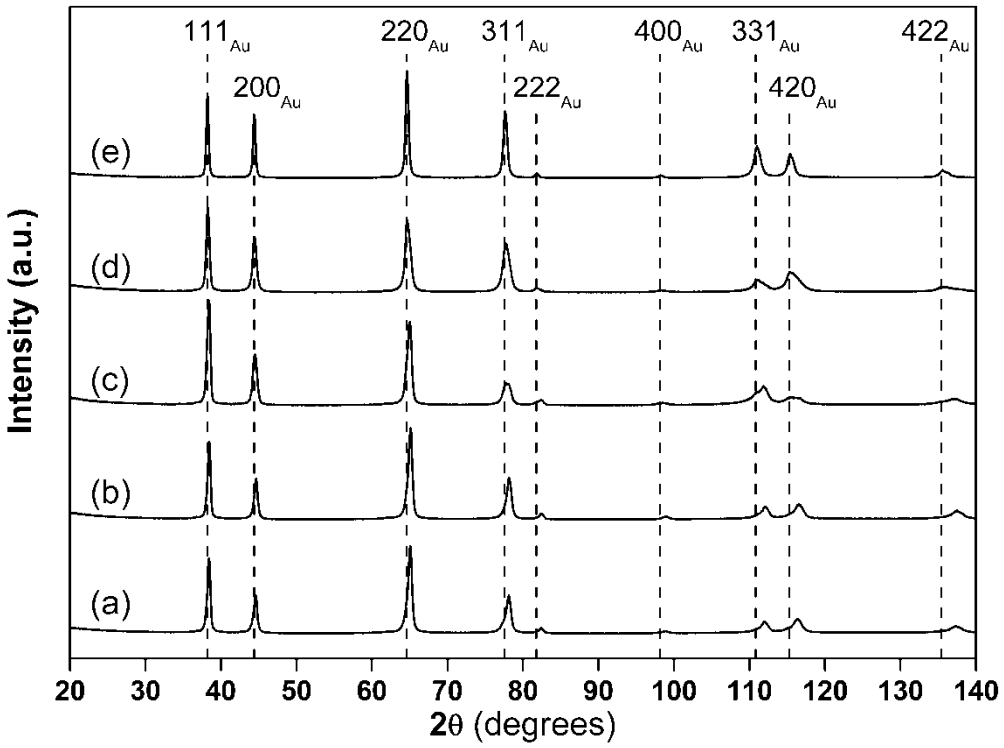

Fig. 3.6: XRD-patterns of Au - 10.12 at. % Co in the (a) as-quenched state and after a defined isochronal heat treatment at a heating rate of 20 K min^{-1} up to (b) 550 K, (c) 633 K, (d) 668 K and (e) 773 K. Card 65-2870 for pure Au of the powder diffraction file [34] was used for indexing the Bragg peaks of Au (the peak positions of pure Au have been marked with dashed lines). All observed Bragg peaks can be ascribed to *fcc* Au. Reflections from Co could not be detected. The depletion of the Au-matrix during the precipitation is revealed by the shift of the Au-matrix Bragg peaks towards the peak positions of pure Au, upon increasing temperature.

With advancing depletion of Co from the Au-matrix, the Bragg peaks of the Au-rich matrix phase shift towards smaller 2θ values, i. e. the lattice parameter of the Au-rich phase increases towards the value of pure Au (see dashed lines in Fig. 3.6). The absence of Bragg peaks from the precipitated Co-rich phase during the initial stage of precipitation is ascribed to the small coherent *bcc* Co plates (see section 3.4.4) diffracting coherently with the matrix (cf. Ref. 35). The absence of Bragg peaks in also an advanced stage of precipitation is ascribed to a very large intrinsic broadening of *fcc* Co (see section 3.1) diffraction lines, caused by the very small size (< 15 nm) of the Co precipitates (see Fig. 3.10). In the as-quenched specimens the Bragg peaks observed show a modest but significant broadening. This is due to thermal stresses and lattice defects evolving upon quenching as (i) dislocations [10] and (ii) quenched-in vacancies [36].

3.4.3 Hardness Measurement

The results of the microhardness measurement of specimens after isochronal heating with 20 K min^{-1} to 550 K, 633 K, 668 K and 773 K (see Fig. 3.5), respectively, are shown in Fig. 3.7. Isochronal annealing from room temperature to 550 K induces a structural relaxation associated with a decrease of the hardness from the initial value 205±28 HV of the strained supersaturated solid solution to 167±19 HV.

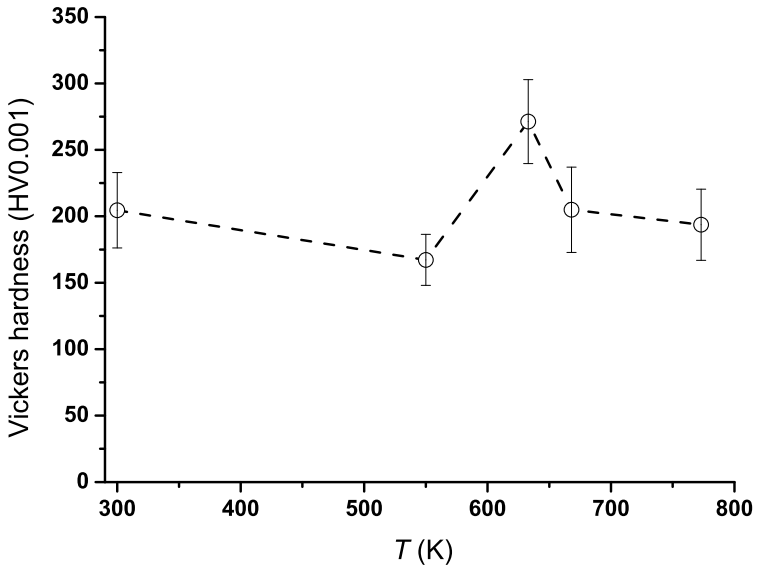

Fig. 3.7: Age hardening of initially supersaturated Au - 10.12 at. % Co solid solution (see the DSC scans shown in Fig. 3.5) after isochronal annealing at a heating rate of 20 K min^{-1} up to 550 K, 633 K, 668 K and 773 K (the dashed line has been drawn to guide the eye). The structural relaxation of quenched-in stresses is followed by a precipitation, transformation and coarsening process (see text). The hardness variation as indicated by the error bars does not result from an inhomogeneous microstructure, e.g. concentration gradients. The measured mean diagonal values left by the pyramid after indentation are in the range from 2 to 5 µm. The determination of the diagonal length is limited by the maximal usable magnification. Hence, the measured accuracy equals about ±20%.

Isochronal annealing from room temperature to 633 K leads to an increase of hardness to 271±31 HV, due to the precipitation reaction, followed by a drop to 205±32 HV upon isochronal annealing to 668 K. This decrease is typical for a precipitation sequence consisting of the initial formation of coherent particles (relatively high hardness), followed by transformation to incoherent, larger particles (drop of hardness; see section 3.4.3). Upon isochronal annealing to 773 K a slight (further) decrease of the hardness to 194±27 HV occurs.

3.4.4 Electron Microscopy – SEM, TEM and HRTEM

3.4.4.1 As-quenched

A TEM bright field image and the corresponding selected area diffraction pattern (SADP) of the microstructure of Au - 10.12 at. % Co solid solution after quenching from 1233 K to room temperature is shown in Fig. 3.8.

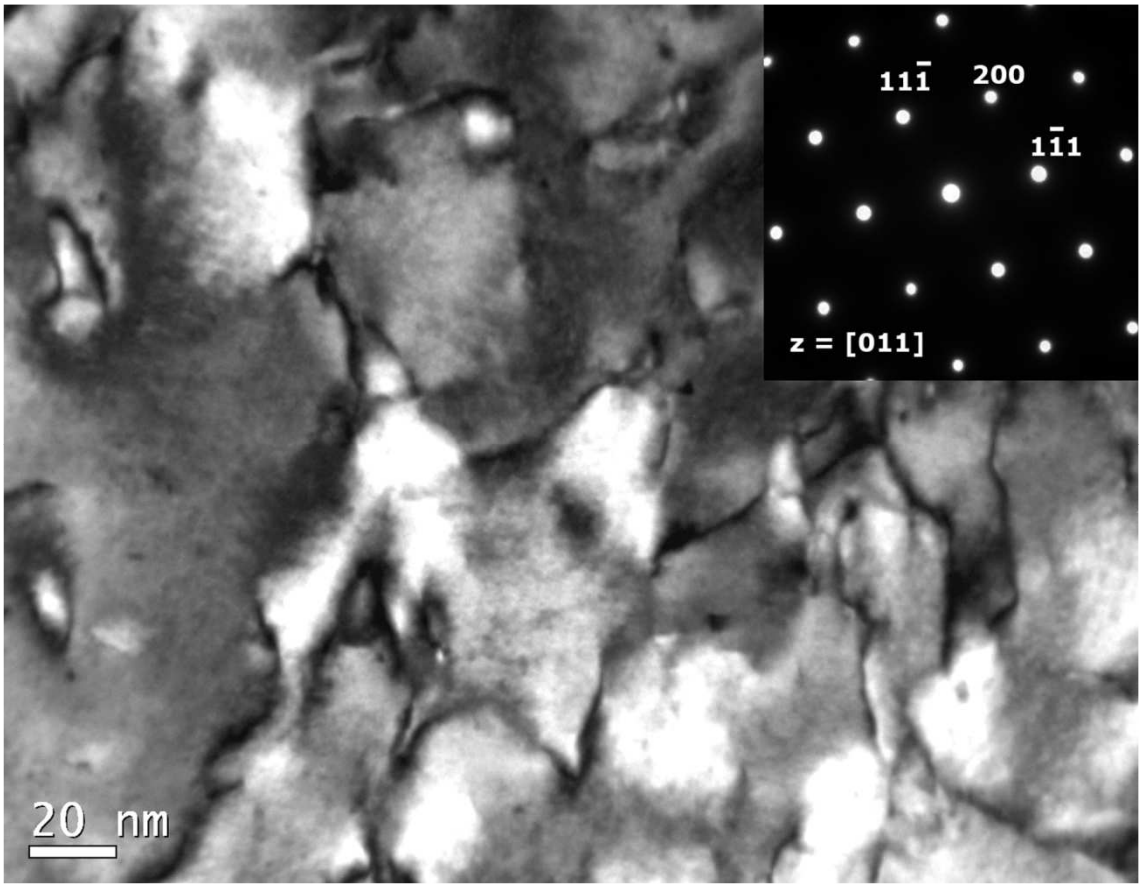

Fig. 3.8: TEM image and SADP of Au - 10.12 at. % Co ([011] zone axis of Au) of the supersaturated Au-rich matrix after quenching from 1233 K into ice water. The dark contrast lines are attributed to a network of dislocations which formed as result of emerging thermal stresses during quenching.

The as-quenched, initial microstructure exhibits a high density network of lines of dark contrast in the bright field TEM image which are attributed to dislocations. The dislocation density was roughly estimated by measuring the length of the dislocation lines per unit area and taking for the thickness of the foil about 100 nm as an upper estimate. On this basis the dislocation density can be given with $5 \cdot 10^{14}$ m^{-2} as an underestimate.

3.4.4.2 Isochronal Annealing

SEM images, TEM bright field images and corresponding SADPs, and HRTEM images taken after isochronal anneals to 550 K, 633 K, 668 K and 773 K at a heating rate of 20 K min^{-1} are shown in Fig. 3.9, Fig. 3.10 and Fig. 3.11, respectively.

The SEM image presented in Fig. 3.9a shows that the microstructure after isochronal annealing with 20 K min^{-1} up to 550 K consists of a homogeneous granular structure with a grain size in the range from 500 to 1000 µm. A TEM bright field image, and the corresponding SADP, of the same specimen are shown in Fig. 3.10a. Besides lines of dark contrast caused by dislocations (cf. Fig. 3.8 and its discussion in section 3.4.4.1) no indication of a precipitation product can be observed. The dislocation density was estimated at $3 \cdot 10^{14}$ m^{-2} (same procedure as described above), i. e. about 40 % lower than in the as-quenched state.

After isochronal annealing up to 633 K, in contrast with the microstructure observed after annealing to 550 K, a few grain boundaries have become decorated with a thin edge of about 4 to 5 µm thickness exhibiting discontinuous precipitation. TEM and HRTEM images (Fig. 3.10b and Fig. 3.11a) show, in the bulk of the grains, the presence of very thin (semi-)coherent *bcc* Co plates along $\{001\}_{\text{Au-matrix}}$ planes (see Ref. 11 where it has been proven that these platelets present a *bcc* modification of Co) only 0.5 to 1 nm (two or three atomic layers) thick, with a lateral extension from 5 to 10 nm. Streaks are observed in the SADP in [100] an [010] directions, compatible with the presence of the Co plates diffracting coherently with the Au-rich matrix [35]. The habit plane is of {100} type: In case of a [001] zone axis of the Au-rich matrix two sets of mutually perpendicular precipitate platelets along (100) and (010) planes of the Au-rich matrix are observed exhibiting the orientation relationships $(100)_{Au,fcc}$ // $(100)_{Co,bcc}$, $[001]_{Au,fcc}$ // $[011]_{Co,bcc}$ and $(010)_{Au,fcc}$ // $(100)_{Co,bcc}$, $[001]_{Au,fcc}$ // $[011]_{Co,bcc}$ (Fig. 3.10b), i. e. two variants of the Bain orientation relationship. The third variant ($(100)_{Au,fcc}$ // $(110)_{Co,bcc}$, $[001]_{Au,fcc}$ // $[001]_{Co,bcc}$) concerns plates parallel to the TEM foil surface and is out of contrast because of the coherent nature of the platelet/matrix interface.

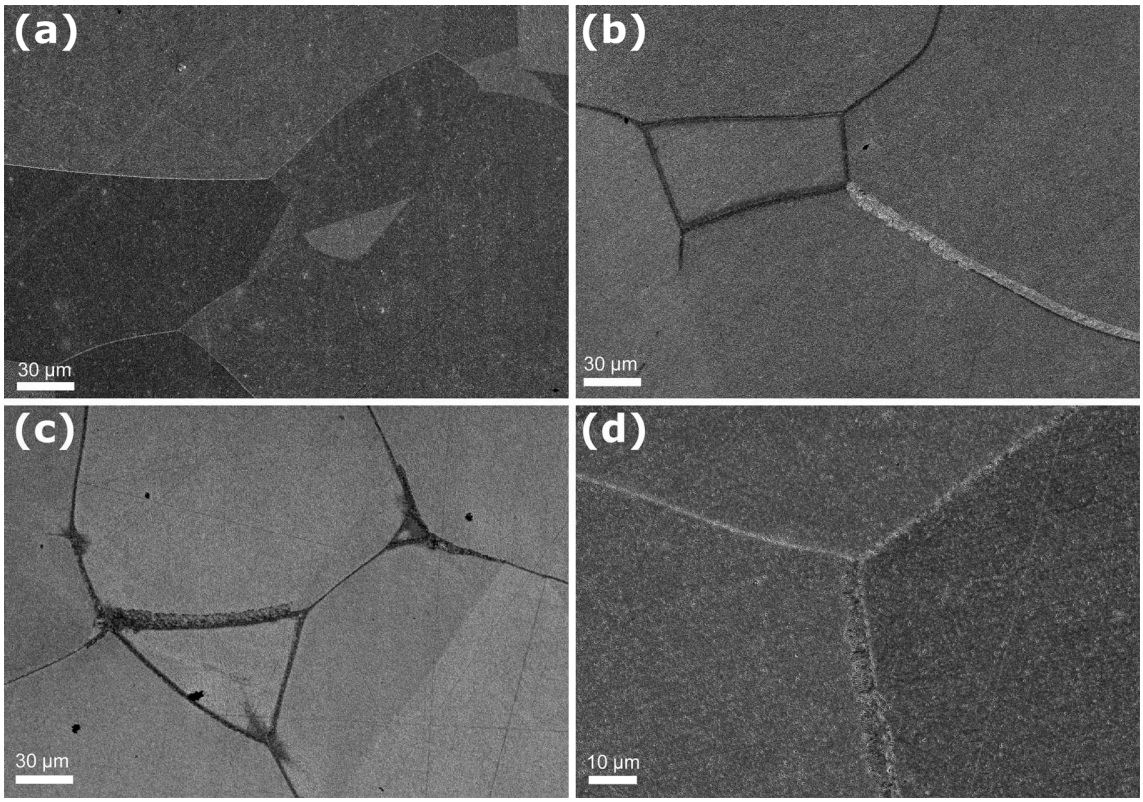

Fig. 3.9: SEM image (secondary electron contrast images) of etched Au - 10.12 at. % Co after isochronal heating with 20 K min^{-1} up to (a) 550 K, (b) 633 K, (c) 668 K, (d) 773 K. (b) Some grain boundaries of the Au-matrix grains have become decorated with a thin edge due to discontinuous precipitation (DP). (c, d) The growth of the DP edge has stopped at a temperature close to 633 K.

Upon isochronal annealing up to 668 K, the discontinuous precipitation edge at grain boundaries has not grown further, as compared to the annealing up to 633 K (cf. Fig. 3.9b and Fig. 3.9c). Some coarsening of the platelike precipitates in the bulk of the grains has occurred (cf. Fig. 3.10b and c and, in particular, Fig. 3.11a and b). At this stage some precipitates establish locally a Moiré pattern diffraction contrast (see locations marked with a dashed circle and the inset in Fig. 3.10c), which indicates a loss of coherency (matrix and precipitate diffract incoherently). The extent of the strain fields surrounding the precipitates, as exhibited by the corresponding strain contrast visible in Fig. 3.10b for the anneal up to 633 K, has decreased considerably for the anneal up to 668 K. The concentration of (dissolved) Co in the Au-rich matrix at this stage (largely completed main DSC peak; cf. Fig. 3.5) was measured with EDX to be about 5.3±2.3 at. %.

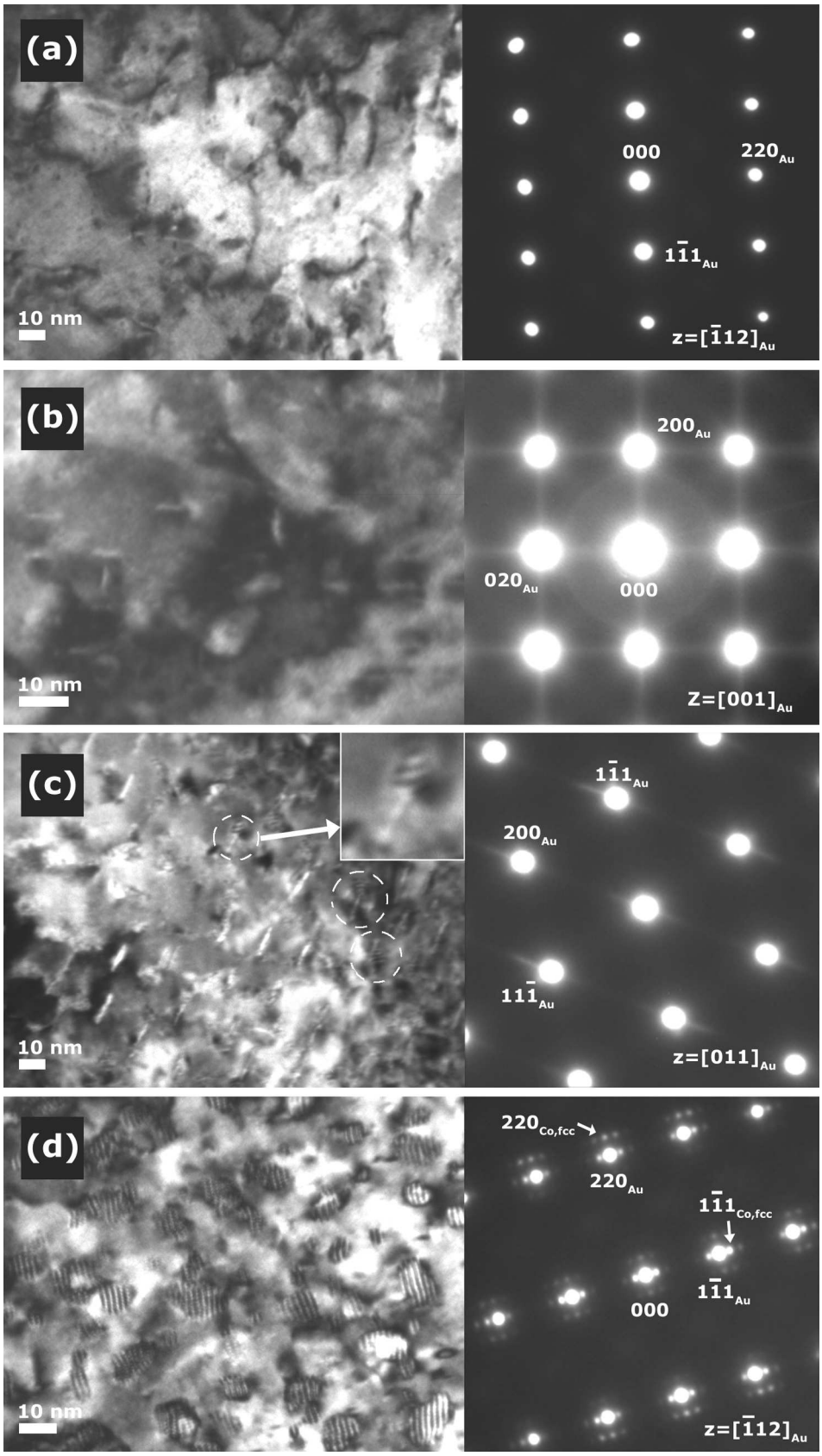

Fig. 3.10: TEM bright field images and the corresponding SADPs of Au - 10.12 at. % Co after isochronal heating with 20 K min^{-1} to (a) 550 K in $[-112]_{Au}$ zone axis, (b) 633 K in $[001]_{Au}$ zone axis, (c) 668 K in $[011]_{Au}$ zone axis and (d) 773 K in $[-112]_{Au}$ zone axis.

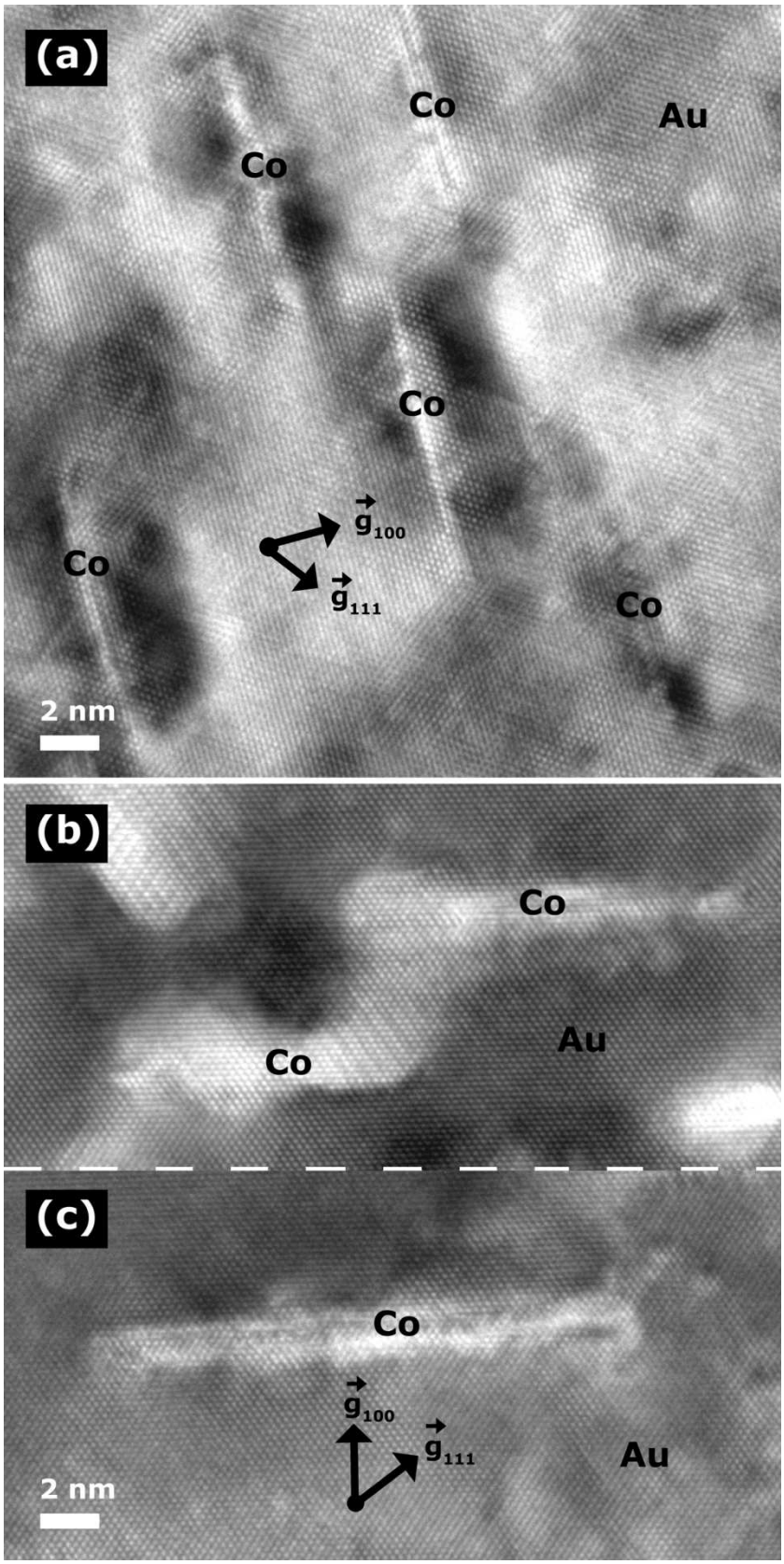

Fig. 3.11: HRTEM images of Au - 10.12 at. % Co after isochronal heating with 20 K min^{-1} to (a) 633 K and (b, c) 668 K. (a) $[011]_{Au}$ zone axis; Co has precipitated as very thin coherent, *bcc* plates about 0.5 to 1 nm thick and 5 to 10 nm in width. (b, c) $[011]_{Au}$ zone axis showing two examples of Co plates having become thicker upon prolonged isothermal heating up to 668 K.

Upon heating to 773 K, also no further growth of the discontinuous precipitation edge has occurred (Fig. 3.9d). In this stage incoherent, bulky, equiaxed Co precipitates have formed with an *fcc* crystal structure, as revealed by the small diffraction spots close to the Au spots in the SADP (see Fig. 3.10d). This leads to the distinct areas of Moiré contrast at the lateral positions of the precipitates in Fig. 3.10d. The *fcc* Co precipitates exhibit a cube-on-cube, epitaxial orientation relationship with the *fcc* Au matrix.

(a) The concentration of (dissolved) Co in the Au-rich matrix after heating to 773 K was measured with EDX to be about 0.9±0.9 at. % which well agrees with the equilibrium concentration indicated by the phase diagram [2].

(b) The second isochronal DSC runs, conducted directly after the first runs, do not show any further heat release.

It can be concluded from (a) and (b) that the precipitation process has been completed after the first isochronal annealing run. This conclusion is supported by the observed shift of the X-ray diffraction-line positions (Fig. 3.6).

3.4.4.3 Isothermal Annealing

TEM bright field images and the corresponding SADPs after isothermal annealing for 4 h at 567 K are shown in Fig. 3.12. Platelike coherent *bcc* Co and incoherent *fcc* Co particles can be discerned. The *bcc* Co platelets are surrounded by strain-field contrast, as a result of the associated coherency strains in the surrounding Au-matrix, and identified in particular by the positions of the separate small diffraction spots occurring close to $1\text{-}11_{Au}$ indicating a *bcc* Co crystal structure (see SADPs of Fig. 3.12a and b; see also Ref. 11). Some platelets exhibit a strain-field contrast which is less distinct. This is due to an *fcc* crystal structure of Co for these precipitate particles which is associated with an incoherent platelet/Au-rich matrix interface (see Ref. 11 for more details). The *bcc* / *fcc* precipitate platelets were found to be oriented parallel to {100} planes of the Au-rich matrix.

The initially *bcc* Co precipitates which passed the transformation from *bcc* to *fcc* crystal structure are revealed (also) by the emergence of a Moiré pattern diffraction contrast compatible with a cube-on-cube epitaxial orientation of the *fcc* Co particles with respect to the Au matrix. The morphology of some precipitates, e. g. the particle in Fig. 3.12a marked with the dashed, curved line, suggests how the eventual shape change from initially platelike *bcc* precipitates into equiaxed *fcc* precipitates at the end of precipitation takes place: The marked, platelike *bcc* particle has started to bulge out in the center as exhibited by the Moiré pattern contrast.

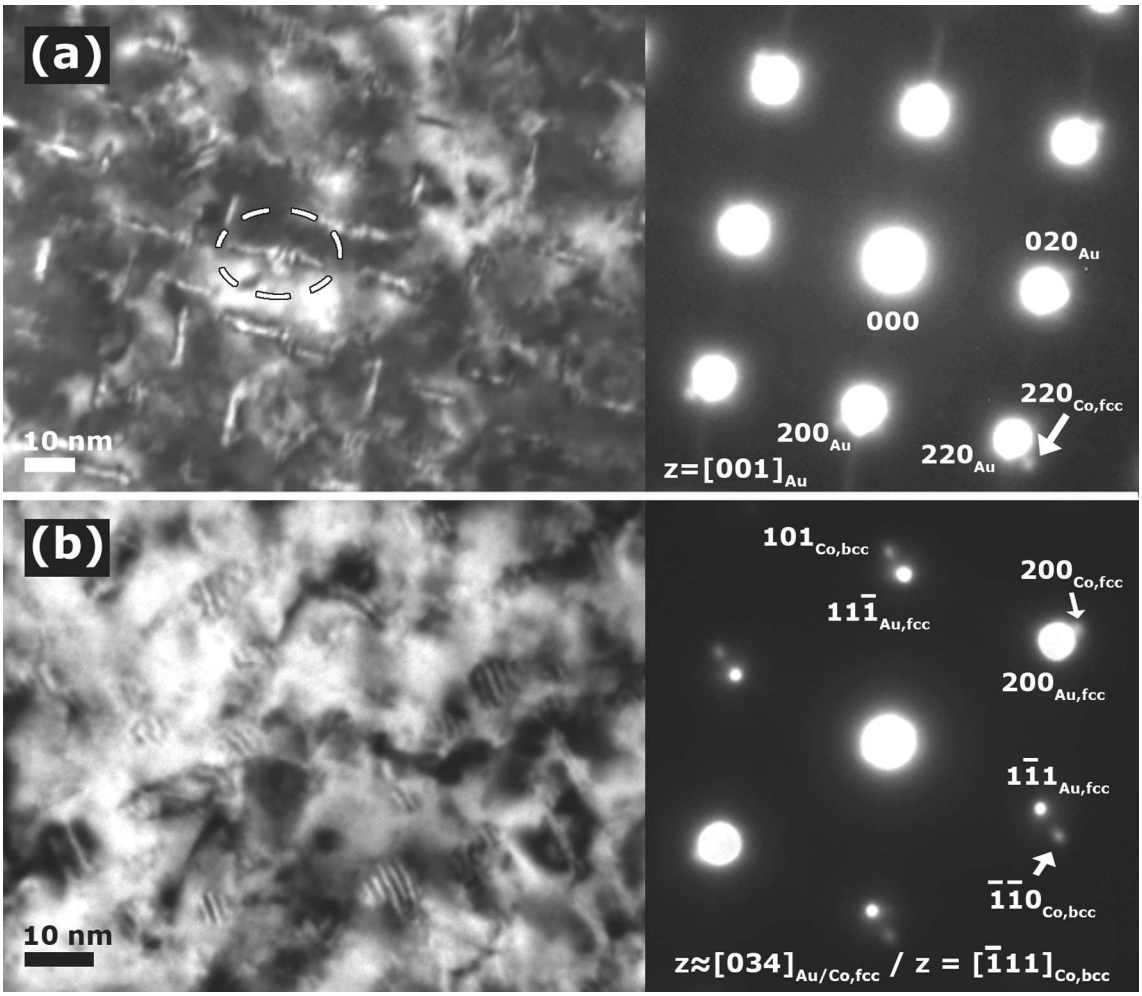

Fig. 3.12: TEM bright field images and SADPs of Au - 10.12 at. % Co after isothermal annealing at 567 K. (a) $[001]_{Au}$ zone axis and (b) tilted by 9.7° from $[011]_{Au}$ zone axis towards the $[001]_{Au}$ zone axis (see also Ref. 11). Platelike *bcc* and *fcc* Co particles have developed. The *bcc* Co platelets (SADP in (b): See the $(\text{-}1\text{-}10)_{Co,bcc}$ spot close to the $(1\text{-}11)_{Au,fcc}$ spot) are visible due to strain-field contrast resulting from coherency strains. The *fcc* Co particles (SADP in (a): See $(220)_{Co,fcc}$ spot close to $(220)_{Au}$; SADP in (b): See $(200)_{Co,fcc}$ spot close to $(200)_{Au}$) exhibit a cube-on-cube, epitaxial orientation with the Au-matrix leading to a Moiré pattern contrast in the bright field image due to double diffraction causing spots close to 000 (see, in particular, bright field (b)). Some *bcc* Co plates just have passed the transformation from *bcc* to *fcc* as visible by a local bulging and Moiré pattern contrast (see particle marked with a dashed, curved line in (a)).

3.4.5 Kinetic Analysis

3.4.5.1 Model Fitting Procedure

The precipitation of Co, as exhibited by the release of heat in the DSC scans, proceeds by two reactions as illustrated by the occurrence of a first main peak followed by a second minor peak or shoulder in the DSC scans recorded for both, isochronal annealing (distinctly visible, see Fig. 3.5) and isothermal annealing (in particular see in Fig. 3.4 the curve recorded at 567 K).

SEM and TEM results shown in section 3.4.4 indicate that upon isochronal annealing in the temperature range of the first peak (i) a dominant continuous precipitation takes place in the bulk of the grains and (ii) a minor discontinuous precipitation occurs in small regions along some grain boundaries. This leads to the interpretation that the major, first peak in the isochronal DSC scans is due to the precipitation of coherent, fine *bcc* Co platelets. TEM results also indicated that in the temperature range of the second peak the transition from coherent *bcc* Co platelets to incoherent *fcc* Co particles occurs (see section 3.4.4.2). The second peak can thus be ascribed to the *bcc*-to-*fcc* transformation accompanied by a transition from coherent to incoherent precipitate/matrix interfaces associated with a release of strain energy. Because the highest temperature applied for the isothermal annealing experiments is lower than the end temperatures reached in the isochronal annealing experiments, a less complete (coherent) *bcc* to (incoherent) *fcc* transition occurs in the isothermal anneals and the Co particles maintain a largely platelike morphology (see section 3.4.4.3). Thus, a slight indication of a second process (heat effect) is also obtained for the isothermal anneals.

The above discussion indicates that an explicit kinetic analysis of the precipitation of the coherent platelike *bcc* Co precipitates is possible on the basis of the first, main peak of heat evolution. In the following the procedure for fitting an appropriate kinetic model to the first peaks as recorded for both, the isothermal and isochronal annealings, is described.

First the first peak has to be extracted from the composite (two overlapping peaks) curves. This separation has been achieved subject to two constraints: (1) The sum of the areas (heat effects) enclosed by the separated first and second peaks must equal the area enclosed by the measured, composite curve. (2) The areas (heat effects) assigned to the first and second peak must be the same for all annealing temperatures or heating rates (here it is assumed that the transformation enthalpy is practically constant in the temperature range where precipitation occurs; this is validated by the results presented in section 3.4.1). The cumulative transformation enthalpy, $\Delta H(T(t))$ for isochronal and $\Delta H(t)$ for isothermal annealing, is described by the total transformation enthalpies of the first and second processes, $\Delta H^1_{\mathrm{tot}}$ and $\Delta H^2_{\mathrm{tot}}$, respectively, with the corresponding degrees of transformation, f_1 and f_2, as weighting factors:

$$\Delta H = f_1 \Delta H^1_{\mathrm{tot}} + f_2 \Delta H^2_{\mathrm{tot}} . \qquad (3.14)$$

The approach represented by Eq. (3.14) is only intended as a possibility to correct for the occurrence of (i. e. to subtract) the second, minor process (peak): In the following only the kinetics of the first dominant process (peak) is interpreted quantitatively in physical terms. To correct for the second process (peak) the modular transformation model is adopted for both processes, i. e. in case of the second process only as a tool to fit the second peak.

Adopting Eq. (3.14), the extended transformed volume fractions, $x_{e,1}$ and $x_{e,2}$, pertaining to transformations 1 and 2, are taken as described by Eqs. (3.8) and (3.9) for isothermal and isochronal annealing, respectively. Impingement modes according to either Eqs. (3.11) and (3.12) are considered. The kinetic parameters in Eqs. (3.8) and (3.9) are K_0, Q and n, which in principle can be time (isothermal annealing) or temperature (isochronal annealing) dependent, which is compatible with Eqs. (3.8) and (3.9) (see discussion in section 3.2.2.1). The analysis of the kinetic data in the present case demonstrates (see below) that it suffices to adopt K_0, Q and n as constants, the values of which can be determined by fitting (results of fitting this model will be denoted with "general"). If the anisotropic impingement mode as given by Eq. (3.12) is adopted, the anisotropy parameter ξ is added to the fit parameters.

Values for the fit parameters, for both f_1 and f_2, have been determined by fitting to $\Delta H(t)$ or $\Delta H(T(t))$. Again note that at this stage the parameters for process 2 only serve to effectively extract the heat effect of the dominant first heat effect from the total heat effect.

All isothermal and all isochronal scans were fitted simultaneously. The mean square error (MSE) was defined as the sum of the squared differences between the calculated (f_{calc}) and experimental (f_{exp}) transformed fraction curves normalized with the latter and summarized for all heating rates (in case of isochronal annealing) and temperatures (in case of isothermal annealing) and minimized by varying the respective fit parameters using a multidimensional unconstrained nonlinear minimization fitting routine [37] as implemented in MATLAB for each, i^{th}, of the applied heating rates

$$MSE = \sum_{i=1}^{n_\Phi, n_T} \left[\sum_{\text{data points}} \left(\frac{f_{exp} - f_{calc}}{f_{exp}} \right)^2 \right] \tag{3.15}$$

with n_Φ as the number of applied heating rates and n_T as the number of isothermal annealing temperatures.

3.4.5.2 Fitting the Data

The experimental *isothermal* DSC scans (symbols; to keep the figure transparent not all data points have been plotted) and the results of the kinetic model fitting (lines) are shown in Fig. 3.13a and Fig. 3.13b. The kinetic parameters K_0, Q and n for the initial precipitation of *bcc* Co platelets from the Au - 10.12 at. % Co solid solution, were determined applying an impingement correction according to either Eq. (3.11) or Eq. (3.12); the results are shown in Table 3.3.

The above applied kinetic model, denoted by "general" in Table 3.3, is described by the combination of Eq. (3.8) with Eqs. (3.11) or (3.12). For specific nucleation and growth modes explicit expressions for K_0, Q and n have been given in Tables 1 to 3 in Ref. 14. It can be shown that, adopting site saturation (at $t = 0$) as nucleation mode and linear growth as growth mode (this fixes n: $n = d/m = 2$ ($d = 2$: lateral growth of platelets; $m = 1$); cf. Table 3 in Ref. 14), good fits to the experimental data are obtained as well: See the agreement of the results, given in Table 3.3, for Q and n as obtained for the general analysis and for Q_G (= Q in case of site saturation with $n = d/m = 2$; cf. Eq. (3.10)) and n as obtained (Q_G) and used (n) for this specific analysis. Additionally, the specific analysis yields a value for the number of nuclei present at $t = 0$, N^* (see Table 3.3), which, strikingly, is of the same order of magnitude as the dislocation density number of the as-quenched state (see section 3.4.4.1). It is thus suggested that the isothermal precipitation of the *bcc* Co platelets can be described by site saturation ($t = 0$) and linear growth.

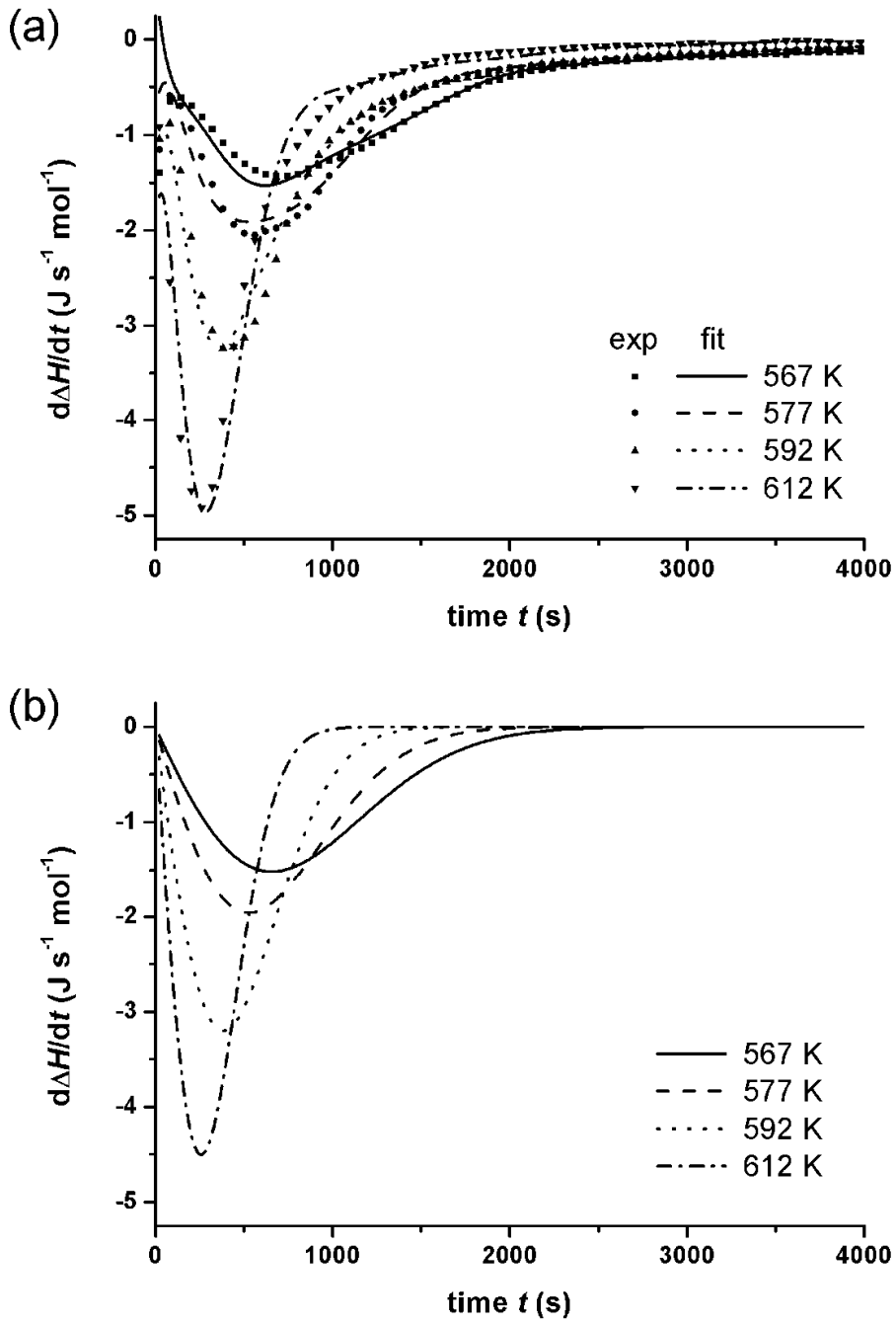

Fig. 3.13: Isothermal DSC curves (symbols) and results of the fitting (lines) of the modular phase transformation model to simultaneously all isothermal DSC scans; the "general" case (see text and Table 3.3). (a) plot of ΔH_{tot} vs. *t*. (b) plot of $f_1 \Delta H_{tot}^1$ vs. *t*.

Table 3.3: Overview of the values determined for the kinetic parameters for the precipitation of the *bcc* Co platelets by fitting to, *simultaneously*, all *isothermal* DSC scans using a version of the modular transformation model as indicated; *MSE* is the mean square error of the fit. Values for the overall activation energy *Q* and the growth exponent *n* as determined independently (Fig. 3.15b and Fig. 3.16b) have also been included.

model	**Impingement**	K_0 (s^{-1})	N^* (m^{-3})	Q (kJ mol^{-1})	Q_G (kJ mol^{-1})	n	ξ	*MSE* (%)
general	Eq. (3.11)	194	-	57.3	-	1.8	-	1.9
	Eq. (3.12)	190	-	57.2	-	1.8	1.0	2.0
site saturation + interface controlled growth	Eq. (3.11)	-	$4.3\cdot10^{14}$	-	61.3	2/1	-	17.6
	Eq. (3.12)	-	$2.6\cdot10^{14}$	-	60.0	2/1	1.0	15.0
procedure for *Q*; Kissinger-like analysis [25]				58±2				
procedure for *n* [14]						1.9±0.1		

The experimental *isochronal* DSC scans (symbols; to keep the figure transparent not all data points have been plotted) and the results of the kinetic model fitting (lines) are shown in Fig. 3.14a and Fig. 3.14b. The kinetic parameters K_0, Q and n for the initial precipitation of *bcc* Co platelets from the Au - 10.12 at. % Co solid solution were determined applying an impingement correction according to Eq. (3.11); the results are shown in Table 3.4.

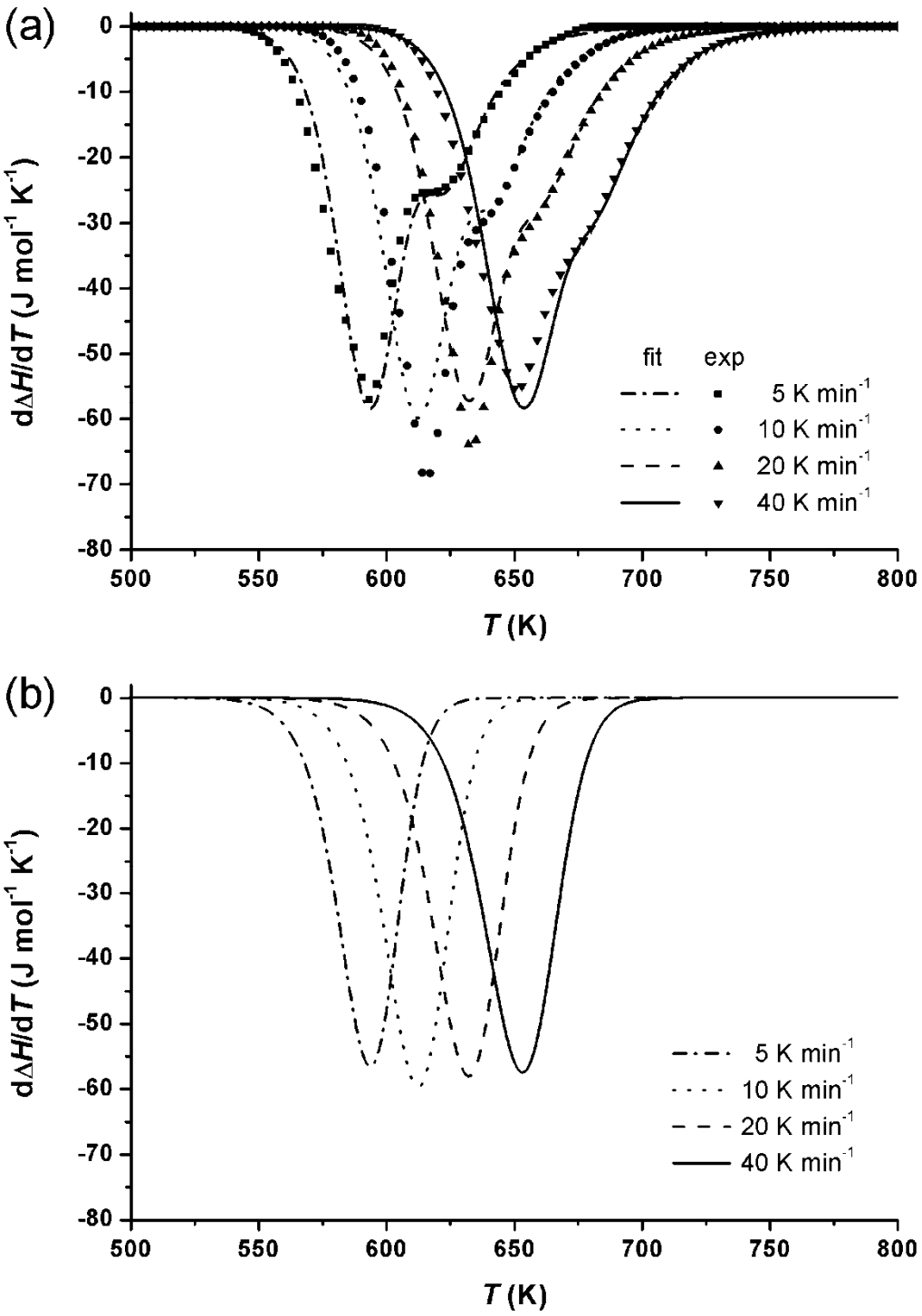

Fig. 3.14: Isochronal DSC curves (symbols) and results of the fitting (lines) of the modular phase transformation model to simultaneously all isochronal DSC scans; the "general" case (see text and Table 3.4). (a) plot of ΔH_{tot} vs. T. (b) plot of $f_1 \Delta H_{tot}^1$ vs. T.

The above applied kinetic model, denoted by "general" in Table 3.4 is described by the combination of Eq. (3.8) with Eq. (3.12). For specific nucleation and growth modes explicit expressions for K_0, Q and n have been given in Tables 1 to 3 in Ref. 14. It can be shown that, adopting continuous nucleation as nucleation mode and interface-controlled growth as growth mode (this fixes n: $n = d/m + 1 = 3$ ($d = 2$: lateral growth of platelets; $m = 1$); cf. Table 3 in Ref. 14), good fits to the experimental data are obtained as well: See the agreement of the results, given in Table 3.4, for Q and n as obtained for the general analysis and for Q_N and Q_G (yields Q with $n = d/m + 1 = 3$; cf. Eq. (3.10)) and n as obtained (Q) and used (n) for this specific analysis. It is thus suggested that the isochronal precipitation of the *bcc* Co platelets can be described by continuous nucleation and anisotropic linear growth.

Table 3.4: Overview of the values determined for the kinetic parameters for the precipitation of the *bcc* Co platelets by fitting to, *simultaneously*, all *isochronal* DSC scans using a version of the modular transformation model as indicated; *MSE* is the mean square error of the fit. Values for the overall activation energy Q and the growth exponent n as determined independently (Fig. 3.15a and Fig. 3.16a) have also been included.

model	K_0 (s^{-1})	Q (kJ mol^{-1})	n	ξ	*MSE* (%)
general	$2.8 \cdot 10^6$	102	2.8	1.4	5.2
continuous nucleation + interface controlled growth	$2.6 \cdot 10^6$	102	2/1 + 1 (fixed)	1.7	5.3
procedure for Q; Kissinger-like analysis [25]		110±15			
procedure for n [14]			2.9±0.1		

For determination of the effective activation energy, Q, full modular transformation model fitting needs not to be performed. A value of Q can be determined without recourse to any specific model using procedures given in Refs. 14 and 25. A value for the growth exponent, n, can also be determined without specifying specific nucleation and growth modes, but in this case an impingement mode has to be selected [14].

Then, for isochronal anneals of variable heating rate, Φ, the effective activation energy Q can be deduced from the temperatures, T_f, where a specific, chosen degree of transformation is attained: The activation energy can be determined, according to the Kissinger-like analysis [25], from the slope of the straight line fitted to the data in a plot of $\ln(T_f^2/\Phi)$ vs. $(RT_f)^{-1}$ with R as the gas constant (see Fig. 3.15a). For isothermal anneals of variable temperature, T, the effective activation energy Q can be deduced from the times, t_f, needed to attain a specific, chosen degree of transformation: The activation energy can be determined from the slope of the straight line fitted to the data in a plot of $\ln(t_f)$ vs. $1/T$ (see Fig. 3.15b) [25].

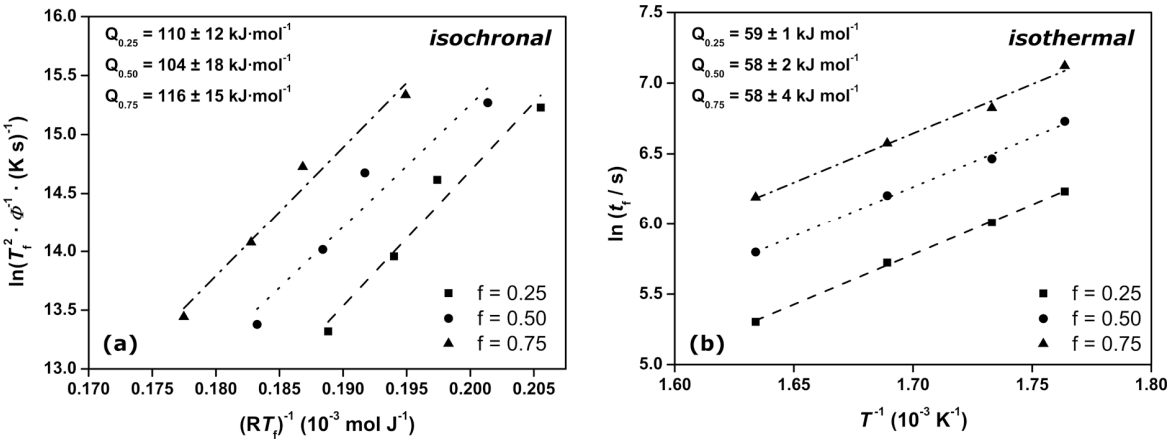

Fig. 3.15: Determination of the effective activation energy for (a) isochronal annealing (Kissinger-like analysis [25])and (b) isothermal annealing [25]: Plot of (a) $\ln(T_f^2/\Phi)$ vs. $(RT_f)^{-1}$ with Φ as the heating rate and with T_f as the temperature at which the degree of transformation attains a specific, chosen value, and (b) $\ln(t_f)$ vs. $1/T$ with t_f as the time needed to attain a specific chosen value of f. Results for f = 0.25, 0.50 and 0.75 are shown. The slope of the straight line fitted to the data points for constant f yields a value for the effective activation energy Q. The corresponding values of Q have been indicated in the figure.

For isochronal anneals of variable heating rate, Φ, a value for the growth exponent n can be deduced from the degree of transformation, f_T, where a specific chosen temperature is attained [14]: The growth exponent can be determined from the slope of the straight line fitted to the data in a plot of $\ln[((1-f_T)^{1-\xi} - 1)/(\xi - 1)]$ vs. $\ln(\Phi)$ with impingement according to Eq. (3.12) (see Fig. 3.16a) using $\xi = 1.4$ as obtained from the "general" kinetic model fitting (see Table 3.4). For isothermal anneals of variable temperature T a value for the growth exponent n can be deduced [14] from the slope of the straight line fitted to the data in a plot of $\ln(-\ln(1-f))$ vs. $\ln(t)$ with impingement according to Eq. (3.11) (see Fig. 3.16b).

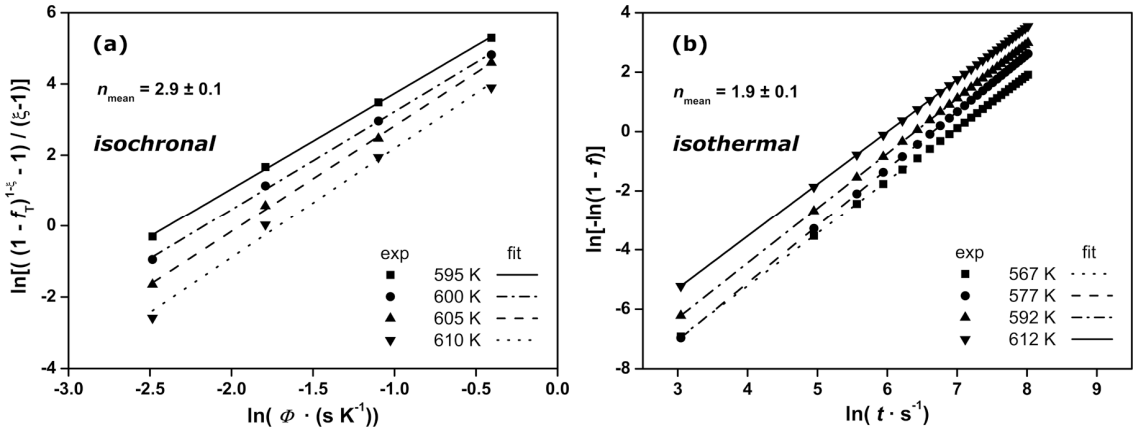

Fig. 3.16: Determination of the growth exponent according to procedures for (a) isochronal and (b) isothermal annealing given in [14]: (a) plot of $\ln[((1-f_T)^{1-\xi} - 1)/(\xi - 1)]$ vs. $\ln\Phi$ with Φ as the heating rate and with f_T as the transformed fraction at which the temperature attains a specific, chosen value. (b) plot of $\ln(-\ln(1 - f))$ vs. $\ln t$. ξ = impingement parameter (equals 1.4; see Table 3.4). Results for T = 595 K, 600 K, 605 K and 610 K are shown. The slope of the straight line fitted to the data points for constant temperature yields a value for the growth exponent n. The corresponding values of n have been indicated in the figure.

The values for the effective activation energy, Q, and the growth exponent, n, as determined by these separate methods have also been included in Table 3.3 and Table 3.4. Evidently (see Table 3.3 and Table 3.4) the values of Q and n as obtained from (i) full fitting of the modular phase transformation model and (ii) application of the separate methods, independent of a specific model, agree well.

3.5 Discussion

3.5.1 Microstructural Evolution

Lattice defects are created during quenching from 1233 K to room temperature: Dislocations were found with an estimated density of $5 \cdot 10^{14}$ m^{-2} (Fig. 3.8); in accordance with observed broadening of the X-ray diffraction lines of the Au-rich phase. Upon subsequent isochronal annealing recovery occurs as exhibited by heat evolution in the temperature range from 450 K to 575 K with a total amount of heat released of about +80 J mol^{-1}, which compares well with the value found for the similar recovery process in, for example, pure deformed iron [38]. Compatible with the occurrence of recovery, in the same temperature range both, the hardness (Fig. 3.7) and the diffraction-line broadening (Fig. 3.6), decrease.

A comparison of the microstructure after quenching with that after isochronal annealing to 550 K, i. e. after the recovery discussed above, shows a distinct decrease (of about 40 %) of the dislocation density to a value of about $3 \cdot 10^{14}$ m^{-2}, but this dislocation density is still six orders of magnitude larger than that for the annealed, stress-free state with a typical dislocation density of about 10^8 m^{-2}. Assuming that the heat released during recovery is predominantly due to the released elastic strain energy U_e, due to the dislocation annihilation, the number density of annihilated dislocations can be estimated, using the standard expression $1.5Gb^2$ for the dislocation-line energy (per unit length) with G as the shear modulus of the Au-matrix (G = 27 GPa) and b as the magnitude of the Burgers vector of the dislocations (b = 0.288 nm). It thus follows that the number density of annihilated dislocations, during the recovery, is about 10^{15} m^{-2}. This value is indeed of the same order of magnitude, but larger (see below), as determined by TEM (see above) for the decrease of the dislocation density by recovery.

Besides the existence of a high density of dislocations in the as-quenched and also in the as recovered microstructures, additionally a high density of single and/or double vacancies and their agglomerates can be present. During recovery an annihilation of quenched-in vacancies can take place [36] which, in addition to the decrease of the dislocation density, can lead to a small heat release. Therefore, the density of annihilated dislocations as estimated from the released heat (see above) can indeed be larger than the corresponding value derived from the TEM measurements.

The results of the kinetic analysis reveal the role of the (retained) lattice defects discussed above (see section 3.5.2).

The decomposition of the supersaturated solid solution of Au – 10.12 at. % Co is largely realized by the coherent precipitation / continuous precipitation (CP) of tiny *bcc* Co platelets. A small part of the process is realized in a discontinuous fashion: A lamellar morphology of Co and Au plates in small regions adjacent to grain boundaries (see Fig. 3.9 in section 3.4.2). In fact a negligible volume fraction of the specimen experienced this discontinuous precipitation (DP): 0.5 vol. %. The growth of the DP stops between 550 K and 633 K. The limited extent of the DP can have various causes: (a) continued movement of the reaction front is obstructed by Co particles, developed by CP, in front of the DP reaction front [39]; (b) the driving force for the reaction-front migration decreases due to a decreasing supersaturation of the matrix (by the continuing CP) [40].

The *bcc* Co platelets (formed by CP) exhibit a coherent $\{100\}_{Au,fcc}$ habit plane (Fig. 3.11). The initial formation of *bcc* instead of *fcc* Co is a result of the delicate interplay, upon Co precipitation, of the Gibbs chemical energy released per unit volume precipitate, the misfit-strain energy per unit volume precipitate and the Gibbs interface energy absorbed per unit area precipitate/matrix interface [11]. A Bain-type orientation relationship [41] exists between the *bcc* Co precipitates and the *fcc* Au-rich matrix (with lattice parameters $a_{Au,fcc} = 0.408$ nm and $a_{Co,bcc} = 0.288$ nm). The habit plane is $(100)_{Au,fcc}$ // $(100)_{Co,bcc}$ (three variants). The above crystallographic data strongly suggest that the *bcc* Co precipitates are coherent with the Au-rich matrix, at least along the habit plane: The value of $a_{Co,bcc}\cdot\sqrt{2}$ closely resembles the value of $a_{Au,fcc}$. Hence, along the $\{100\}_{Au,fcc}$ habit planes no significant lattice mismatch between *bcc* Co and *fcc* Au occurs. However, perpendicular to the habit planes a mismatch of $|a_{Co,bcc} - a_{Au,fcc}|/a_{Au,fcc} \cdot 100\% = 29\%$ occurs. Further, the elastic anisotropy of *fcc* Au with the elastic softest <100> direction supports this type of precipitate orientation and morphology. On this basis, as a consequence of the *bcc* crystal structure of the initial precipitates, the occurrence of the plate-like morphology can be understood.

Upon further annealing, due to the associated growth/coarsening of the Co precipitates, (i) the interface-to-volume ratio of the precipitate particles decreases and (ii) the coherency of the interface cannot be maintained. Consequently, the transformation from the *bcc* to the *fcc* Co crystal structure can now be induced, as the increase of the interfacial energy per unit area interface (coherent → incoherent interface) now can be overcompensated by the gain in chemical Gibbs energy due to the *bcc*-to-*fcc* transformation. A further decrease of the interface energy can be accomplished by a change of the *fcc* particle morphology from platelike to equiaxed.

Whereas formation of coherent precipitates leads to an increase of the hardness, the subsequent loss of coherency during the transformation from *bcc* to *fcc* Co leads to a decay of the hardness (see Fig. 3.7).

The measured total transformation enthalpy pertains to an end stage of precipitation including relatively large, incoherent, equiaxed fcc Co precipitates. Thereby the effects of interface energies and energy release by nucleation on defects have become negligible. Thus the good agreement of the thermodynamically predicted (considering chemical, bulk Gibbs energies only) and experimentally recorded values for the total transformation enthalpy (cf. section 3.4.1) can be understood.

3.5.2 Kinetics

The values found for the overall, effective activation energy, Q, and the growth exponent, n, by application of the "general" approach well agree with those of the model independent procedures. Although the kinetic parameters (K_0, Q and n) fully describe the observed transformation kinetics, an identification of the operating nucleation and growth modes is only possible using additional information: The formation of platelike precipitates (Fig. 3.10, Fig. 3.11 and Fig. 3.12) suggests 2-dimensional growth ($d = 2$). The growth exponents n as determined by the model independent analysis (Fig. 3.16) equal 1.9±0.1 and 2.9±0.1 for isothermal annealing and isochronal annealing, respectively. Within experimental accuracy these values are only compatible in case of isothermal annealing with site saturation and interface-controlled ($m = 1$) growth satisfying the equation $n = d/m = 2/1$ and in case of isochronal annealing with continuous nucleation and interface-controlled growth ($m = 1$) satisfying the equation $n = d/m + 1 = 2/1 + 1$ [13]. Diffusion controlled lateral growth of precipitate platelets can be consistent with linear growth [43].

The occurrence of different nucleation modes, site saturation for isothermal annealing and continuous nucleation for isochronal annealing, can be understood considering the role of the quenched-in defects. After quenching from the homogenization temperature 1233 K in ice water the specimens contain a high density of lattice defects like dislocations and vacancies (cf. section 3.4.2 and Refs. 10 and 36).

In case of isothermal annealing Co nuclei can form rapidly at dislocations without the necessity of overcoming a nucleation-energy barrier (see section 3.2.1.2). The presence of quenched-in excess vacancies facilitates relatively fast diffusion of dissolved Co and thus formation of these nuclei takes place largely already during the rapid heating (at a heating rate of about 500 K min^{-1}), before the isothermal annealing temperature has been reached. Hence, the isothermal annealing is characterized by site saturation at $t = 0$. The Co precipitation reaction at the isothermal annealing temperature is thus only controlled by growth.

The incorporation of a Co atom in the crystal structure of a platelike Co precipitate at the platelet rim is associated with the constraint of maintaining coherency of the platelet with the surrounding Au-rich matrix. The activation energy for the jump of a Co atom through the Au-rich matrix/Co platelet interface at the platelet rim may be larger than the activation energy for the jump of a Co atom dissolved in the Au-rich matrix remote from the precipitate particle, and thus the growth rate can be interface controlled.

In case of isochronal annealing the specimens were heated up from room temperature to 773 K at a heating rate in the range from 5 K min^{-1} to 40 K min^{-1}, i. e. a much lower heating rate than in case of the isothermal annealing experiments where heating up to the annealing temperature occurred at a heating rate of about 500 K min^{-1}. This implies for the isochronal annealing experiments that the time needed for passing the temperature range from room temperature to 567 K (i. e. the lowest temperature used in the isothermal annealing experiment) requires 7 min (Φ = 40 K min^{-1}) to 54 min (Φ = 5 K min^{-1}). Consequently, for the isochronal annealing experiments, recovery could take place considerably before the onset of the precipitation reaction. Indeed, a significant decrease of the defect concentration had taken place before Co precipitation was initiated in the isochronal annealing experiments: note (i) a corresponding heat evolution discussed in section 3.4.1 and (ii) pronounced decrease of the dislocation density (40 %) in case of isochronal heating with 20 K min^{-1} to 550 K (discussed in section 3.4). Further it is remarked that the highest isothermal annealing temperature is lower than the peak temperatures for the precipitation reaction upon isochronal annealing with 10 K min^{-1} to 40 K min^{-1} (cf. Fig. 3.13 and Fig. 3.14). On this basis it can be understood that the nucleation mode upon isochronal annealing can be described as “continuous nucleation”, as compared to “site saturation at $t = 0$” upon isothermal annealing. The effective activation energy, Q = 102 kJ mol^{-1} (see Table 3.4) must be conceived as the weighted sum of Q_N and Q_G (cf. Eq. (3.10)). Estimates for the separate activation energies for nucleation, Q_N, and growth, Q_G, are obtained as follows. In view of the presence of a still large amount of dislocations during the isochronal anneals (see above) it can be expected that the nucleation-energy barrier for nucleation is negligible (see section 3.2.1.2). Then the activation energy for nucleation is given by the activation energy for the jump of a Co atom through the Co-particle/Au-rich matrix interface for a Co particle of *critical size* [13, 14]. Taking, as a crude estimate, the value of this activation energy the same as the value of the activation energy for the jump of Co through this interface at the growth stage of this particle (see discussion in Ref. 14), which equals Q_G, it follows $Q = Q_N = Q_G$ (as $n = d/m + 1$; see Eq. (3.10)) and thus $Q_N \approx Q_G \approx$ 100 kJ mol^{-1} (see Table 3.4). Indeed, (i) this estimate for Q_G is larger than the value determined for the isothermal anneals ($\approx$ 60 kJ mol^{-1}), compatible with a lesser role of defects, and (ii) this estimate is smaller than the activation energy for diffusion of Co in equilibrated Au (174 kJ mol^{-1} [42]), compatible with the state of only partial annihilation of quenched-in defects pertaining to the precipitation reaction upon isochronal annealing.

3.6 Conclusions

- Platelike coherent *bcc* Co nanoparticles (thickness ≈ 0.5 - 1 nm, length ≈ 5 - 10 nm) develop in the initial stage of precipitation from quenched supersaturated Au - 10.12 at. % Co solid solution, in the bulk of the grains, exhibiting a Bain-type orientation relationship $[(100)_{Au,fcc}//(100)_{Co,bcc}$ and $[001]_{Au,fcc}//[011]_{Co,bcc}$ (three variants)], upon both isothermal annealing and isochronal annealing. Prolonged annealing leads to a transition from coherent *bcc* Co to incoherent *fcc* Co precipitates epitaxially oriented with respect to the *fcc* Au matrix $[(100)_{Au,fcc}//(100)_{Co,fcc}$ and $[001]_{Au,fcc}//[001]_{Co,fcc}$ (three variants)]. This *bcc*-to-*fcc* transition is associated with a minor heat effect represented by a shoulder at the DSC peak. During further (isochronal) annealing an equiaxed morphology develops for the precipitated particles.

- A minor amount of discontinuous precipitation (DP) occurs in small regions adjacent to grain boundaries (< 0.5 vol. %). The DP halts in an early stage due to (i) the continuous nucleation in the bulk of the grains accompanied with blocking of the migrating DP reaction front and (ii) the decrease of the driving force for DP due to a decreasing supersaturation upon prolonged precipitation.

- The nucleation and growth modes for the precipitation of the coherent *bcc* Co platelets can be described by a modular phase transformation model. The kinetic parameters can be determined by fitting this model simultaneously to all isothermal DSC runs and simultaneously to all isochronal DSC runs.

- Adopting a two-dimensional growth mode for the Co platelets, the values found for the growth exponent, *n*, lead to the following selection of possible nucleation and growth modes:

    - In case of isothermal annealing the kinetics of the precipitation is governed by site saturation (pre-existing nuclei at $t = 0$) in combination with linear growth. The effective activation energy of the transformation is thus given solely by the activation energy for growth which equals about 60 kJ mol^{-1}.

    - In case of isochronal annealing the kinetics of the precipitation is governed by continuous nucleation in combination with linear growth. The effective activation energy equals about 100 kJ mol^{-1}, which is generally given by a weighted sum of the activation energy for nucleation and the activation energy for growth. In the present case the activation energies for nucleation and growth may be about equal, implying that their values are about 100 kJ mol^{-1}.

- The difference in nucleation mode for the isothermal and isochronal anneals is a direct consequence of quenched-in defects as vacancies and dislocations during quenching and the difference in the extent of recovery before the onset of precipitation. Whereas in case of isothermal annealing most of the quenched-in lattice defects are present at the onset of precipitation, in case of isochronal annealing a partial recovery takes place prior to the begin of precipitation. As a consequence a smaller amount of excess vacancies and dislocations operates during precipitation in the isochronal anneals. This implies for the isochronal annealing experiments, as compared to the isothermal annealing experiments, a different nucleation mode (site saturation → continuous nucleation) and a larger activation energy for growth.

References

[1] J. B. Hess and C. S. Barrett, *J Met* **4** (1952) 645.
[2] H. Okamoto et al., *Bulletin of Alloy Phase Diagrams* **6** (1985) 449.
[3] P. Gaunt and J. Silcox, *Philosphical Magazine* **6** (1961) 1343.
[4] C. J. Clipstone, and P. Gaunt, *Phi Mag* **20** (1969) 173.
[5] N. Kataoka et al., *J Magn Magn Mater* **140-144** (1995) 621.
[6] A. Hütten et al., *Scr Metall Mater* **33** (1995) 1647.
[7] J. Bernardi, A. Hütten, and G. Thomas, *Nanostr Mater* **7** (1996) 205.
[8] J. Bernardi, A. Hütten, and G. Thomas, *J Magn Magn Mater* **157/158** (1996) 153.
[9] C. G. Lee et al., *IEEE Trans Magn* **35** (1999) 2856.
[10] R. B. Campbell and L. Muldawer, *Phil Mag* **6** (1961) 531.
[11] R. Bauer, E. Bischoff, and E. J. Mittemeijer, *Phys Rev B* **81** (2010) 094113-1.
[12] F. Schlawne and H. Alexander, *Z Metallkd* **72** (1981) 105.
[13] E. J. Mittemeijer and F. Sommer, *Z Metallkd* **93** (2002) 352.
[14] F. Liu et al., *Int Mat Rev* **52** (2007) 193.
[15] J. W. Christian, *The Theory of Transformations in Metals and Alloys*, Oxford, Pergamon, (2002) Part 1.
[16] H. I. Aaronson and F. K. LeGoues, *Metal Trans A* **23A** (1992) 1915.
[17] J. D. Eshelby, *Proc Roy Soc London: Series A* **241** (1957) 376.
[18] F. R. N. Nabarro, *Proc Roy Soc London: Series A* **175** (1940) 519.
[19] W. F. Gale and T. C. Totemeier, *Smithells Metals Reference Book*, 8th edt. Oxford, GB, Elsevier Butterworth-Heinemann (2004)
[20] P. Villars and L. D. Calvert. *Pearson's Handbook of Crystallographic Data for Intermetallic Phases* **1**, ASM International, Materials Park, Ohio, (1997).
[21] J. W. Cahn, *Acta Metall* **5** (1957) 169.
[22] M. H. Biglari et al., *Met Mat Trans A* **26A** (1995) 765.
[23] A. T. W. Kempen, F. Sommer, and E. J. Mittemeijer, *J Mat Sci* **37** (2002) 1321.
[24] H. Nitsche et al., *Z Metallkd* **96** (2005) 1341.
[25] E. J. Mittemeijer, *J Mat Sci* **27** (1992) 3977.
[26] F. Liu et al., *Acta Mater* **57** (2009) 6176.
[27] M. J. Starink, *J Mat Sci* **36** (2001) 4433.
[28] F. S. Ham, *J Phys Chem Solids* **6** (1958) 335.
[29] J. B. Austin and R. L. Rickett, *Trans Am Inst Min Metall Eng* **135** (1939) 396.
[30] E.-S. Lee and Y. G. Kimm, *Acta Metall Mater* **38** (1990) 1669.
[31] E.-S. Lee and Y. G. Kimm, *Acta Metall Mater* **38** (1990) 1677.
[32] M. J. Starink, *J Mat Sci* **32** (1997) 4061.
[33] C. Wert and C. Zener, *J Appl Phys* **21** (1950) 5.
[34] *International Centre of Diffraction Data*. Newton Square, PA, USA., (1997-2007).
[35] N. E. V. Vives Díaz et al., *Acta Mater* **56** (2008) 4137.
[36] M. Feller-Kniepmeier and J. Gobrecht, *Acta Metall* **19** (1971) 569.
[37] J. A. Nelder and R. Mead, *Comp J* **7** (1965) 308.
[38] F. Scholz, J. H. Driver, and E. Woldt, *Scr Mater* **40** (1999) 949.
[39] W. Gust, R. Wurster-Scheiffele, and B. Predel, *J less-com. Met* 79 (1981) P11.

[40] I. Manna, S. K. Pabi and W. Gust, *Int Mat Rev* **46** (2001) 53.
[41] E. C. Bain, *Trans Metall Soc AIME* **70** (1924) 25.
[42] D. Duhl, K. I. Hirano, and M. Cohen, *Acta Metall* **11** (1963) 1.
[43] R. Trivedi: *Met. Trans*. **1** (1970) 921.

4 The Kinetics of the Precipitation of Co from Supersaturated Cu-Co Alloy

R. Bauer, B. F. Rheingans, and E. J. Mittemeijer

Abstract

The kinetics of the precipitation of Co from a supersaturated solid solution of Cu - 0.95 at. % Co was investigated by isochronal annealing applying differential scanning calorimetry (DSC) with heating rates in the range $5\ \mathrm{K\ min^{-1}}$ to $20\ \mathrm{K\ min^{-1}}$. The corresponding microstructural evolution was investigated by (high-resolution) transmission electron microscopy [(HR)TEM] in combination with electron energy loss spectroscopy (EELS). Upon isochronal annealing spherical Co precipitates of *fcc* crystal structure form. Kinetic analysis by fitting of a modular phase transformation model to, simultaneously, all DSC curves of variable heating rate measured for Cu - 0.95 at. % Co showed that the precipitation-process mechanism can be described within the framework of this general phase transformation model by continuous nucleation and diffusion-controlled growth. By introducing additional microstructural information (the precipitate-particle density), for the first time values for the *separate* activation energies of nucleation and growth could be deduced from the transformation kinetics.

4.1 Introduction

Knowledge on the nucleation and growth processes involved in a solid-solid phase transformation resulting in a microstructure with specific properties, e. g. mechanical, electric or magnetic properties, is of great interest both from a fundamental scientific point of view and with regard to practical applications. In order to follow the progress of the transformation reaction, a global, macroscopic parameter as the degree of transformation f ($0 \leq f \leq 1$) can be determined experimentally as function of time and temperature. However, it is no easy task to extract from such experimental data quantitative information on the operating modes of nucleation, growth and impingement. To this end a modular phase transformation model [1] has been developed recently that allows separate determination of kinetic data for nucleation, growth and impingement. This model has until now been successfully applied to a variety of phase transformations: crystallization of amorphous metal alloys [2 - 7], the austenite-ferrite transformation in Fe-based alloys [8 - 10] and the polytypic transformations of Laves phases [11].

To explore the applicability of this general description of transformation kinetics to the precipitation of a second, product phase in a supersaturated parent, matrix phase, the precipitation of Co from an initially supersaturated dilute solid solution of Cu - 0.95 at. % Co was investigated as a model system.

At lower temperatures, Cu and Co show only very small mutual solubility [12]. Upon annealing of supersaturated Cu-rich Cu-Co alloys Co-rich precipitates of *fcc* structure form within the *fcc* Cu matrix. During the early stages of the precipitation reaction, these particles show full coherency with the Cu matrix and are of spheroidal shape [13]. Pure Co exhibits an allotropic reaction at the equilibrium temperature T_a = 690±7 K (at 1 atm) [14] with the *hcp* modification as low temperature phase and the *fcc* modification as high temperature phase. Yet, the coherent Co precipitates developing upon precipitation in Cu-rich Cu-Co alloys are generally of *fcc* structure both above and below T_a.

With conventional transmission electron microscopy (TEM), the small Co-rich precipitates are only indirectly visible due to the strain contrast resulting from the lattice misfit, δ, between the lattices of *fcc* Co and *fcc* Cu [13, 15] ($\delta = (a_{Co} - a_{Cu}) / a_{Cu} \cdot 100\% \approx -1.9\%$; with the lattice-parameter of Co, a_{Co} = 0.35447 nm, and of Cu, a_{Cu} = 0.36146 nm, Ref. 16). In bright field zone axis (BFZA) TEM mode, the local distortion of the matrix around a Co particle leads to a well-defined circular strain contrast ring, which center-line corresponds within ± 0.2 nm with the real particle diameter [17, 18].

The kinetics of Co precipitation from dilute Cu-Co alloys has been the subject of a large number of investigations over the last decades aimed at testing the validity of diverse kinetic descriptions, as those based on classical or non-classical nucleation theories (e. g. Ref. 19), sometimes in combination with presumed diffusion-controlled growth (e. g. Ref. 20), based on cluster-dynamics models (e. g. Ref. 21) and on Monte-Carlo simulations (e. g. Ref. 22). Most of these studies showed fair to good agreement or compatibility of the adopted theoretical approach with presented experimental data. However, all experiments were restricted to isothermal annealing and cases of medium or low supersaturation in order to assure moderate reaction rates, which are experimentally accessible by microscopic and/or scattering techniques.

In the present project non-isothermal, but isochronal (i.e. with constant heating rate) annealing experiments, applying differential scanning calorimetry (DSC), have been performed, i.e. the experiments start at a low temperature, where the degree of supersaturation is very high, but the rate of the thermally activated reaction is virtually nil. Upon heating thermal activation eventually becomes substantial enough to induce precipitation from the highly supersaturated solid solution. Thus isochronal heating DSC experiments allow experimental access to data for the formation and growth of Co precipitate particles in the presence of very large driving forces. Large, as compared to small, driving forces can substantially affect the modes of nucleation and growth. Against this background the present work is focused on kinetic analysis, applying a modular phase-transformation model [23], to the precipitation of Co from a highly supersaturated Cu – 0.95 at. % Co solid solution in order to identify the separate nucleation and growth mechanisms and to determine the associated kinetic parameters. It will be shown that the kinetic analysis can be powerfully performed on the basis of isochronal (DSC) annealing experiments, provided the kinetic model is fitted to *simultaneously* all transformation curves measured at various heating rates. In combination with microstructural information (the product-particle density obtained by TEM investigation), separate values for the activation energies of nucleation and growth could be determined.

4.2 Theoretical Background of Transformation Kinetics

The modular phase transformation model comprises three modes – nucleation, growth and impingement – which can be dealt with separately [1, 23]. In the following those aspects of nucleation, growth and impingement which are relevant for the present work are indicated briefly.

According to classical nucleation theory, the steady state rate of nucleation of product phase particles per unit volume can be given as

$$\dot{N}\left(T\left(t\right)\right) = C\omega \exp\left(-\frac{\Delta G^{*} + Q_{\mathrm{N}}}{RT(t)}\right) \tag{4.1a}$$

with the gas constant R, the temperature T depending on time t, the number density of suitable nucleation sites C, a characteristic frequency factor ω, the critical Gibbs energy ΔG^{*} for the formation of a product-phase particle of critical size and the activation energy Q_{N} for the jump of an atom through the interface of a particle of critical size.

In case of large undercooling, i.e. high supersaturation of the parent phase, $\Delta G^{*} \ll Q_{\mathrm{N}}$ and the nucleation can be described by the so-called continuous nucleation rate with an Arrhenius temperature dependency

$$\dot{N}\left(T\left(t\right)\right) = N_{0} \exp\left(-\frac{Q_{\mathrm{N}}}{RT\left(t\right)}\right) \tag{4.1b}$$

with a temperature and time independent pre-exponential factor N_0.

The two possible extreme growth mechanisms, diffusion-controlled and interface-controlled growth, can be given in a compact expression as follows:

$$Y = g\left[\int_{\tau}^{t} \nu \,\mathrm{d}t'\right]^{\frac{d}{m}} \tag{4.2}$$

with Y as the volume of a particle at time t nucleated at time τ, g as the geometry factor describing the particle shape, d as the growth dimension, m as the growth mode (m = 1: “linear growth” at constant temperature, compatible with interface-controlled growth; m = 2: “parabolic growth” at constant temperature, compatible with diffusion-controlled growth), and ν as the growth rate. For large undercooling or overheating, an Arrhenius dependency holds for ν [23]

$$\nu = \nu_{0} \exp\left(-\frac{Q_{\mathrm{G}}}{RT}\right) \tag{4.3}$$

with Q_{G} as the temperature and time independent activation energy for growth. For interface-controlled growth, ν_0 is a temperature-independent interface-velocity constant and Q_{G} represents the energy barrier at the product/parent interface. For diffusion-controlled growth Q_{G} represents the activation energy for diffusion, Q_{D}. In this case, ν_0 is a factor depending on the pre-exponential factor for diffusion, D_0, and on the degree of supersaturation of the matrix phase [24].

Supposing that every product particle grows into an infinitely large parent phase, the precipitate volume of all product particles at time t is given by the so-called extended precipitate volume:

$$V_{\mathrm{p,e}} = \int_0^t V\dot{N}(\tau)Y(\tau,t)\,\mathrm{d}\tau \tag{4.4}$$

where $V_{\mathrm{p,e}}$ is the extended precipitate volume and V is the specimen volume. Note that Eqs. (4.1b) and (4.2) indeed pertain to nucleation and growth, respectively, in the absence of other precipitate particles.

For precipitation reactions the degree of transformation can be defined as the volume V_{p} occupied by precipitate particles normalized with respect to the volume $V_{\mathrm{p,end}}$ of the precipitate particles at the end of the reaction:

$$f \equiv \frac{V_{\mathrm{p}}}{V_{\mathrm{p,end}}} \tag{4.5}$$

with $0 \le f \le 1$. Thus the extended precipitate-volume fraction, $x_{\mathrm{p,e}}$, can be given as (cf. Eq. (4.4))

$$x_{p,e} = \frac{V_{p,e}}{V_{p,end}} = \frac{V}{V_{p,end}} \int_0^t \dot{N}(\tau)Y(\tau,t)\,\mathrm{d}\tau\,. \tag{4.6}$$

Evidently, product-phase particles cannot nucleate and grow in specimen volume that has already been occupied by other product-phase particles. This is called “hard impingement”. Further, if diffusion of solute towards precipitate/product-particles is necessary to establish growth, then a solute-depletion zone can develop around a growing product particle in which zone less likely further nucleation can take place (because of a lesser supersaturation) or even no further nucleation can occur at all (if the supersaturation has become negligible). This is called “soft impingement”. Various explicit modes for hard impingement have been given in the literature (see Ref. 23). A rigorous treatment for “soft impingement” does not exist. It can be inferred (see Ref. 25), for the case of randomly dispersed nuclei and isotropic growth, that a correction for impingement in case of growth controlled by solute diffusion in the matrix can be realized by equating the infinitesimal change $\mathrm{d}f$ with the infinitesimal change of $x_{\mathrm{p,e}}$ multiplied with the untransformed fraction $(1-f)$: $\mathrm{d}f = (1-f)\cdot \mathrm{d}x_{\mathrm{p,e}}$. This leads to

$$f \equiv \frac{V_{\mathrm{p}}}{V_{\mathrm{p,end}}} = 1-\exp\left(-x_{\mathrm{p,e}}\right) = 1-\exp\left(-\frac{V_{\mathrm{p,e}}}{V_{\mathrm{p,end}}}\right). \tag{4.7}$$

This result implies a formalism of "soft impingement" that parallels that for "hard impingement" (also in case of random nucleation and isotropic growth). This may be understood as that for the case of "soft impingement" each precipitate/product particle is supposed to be surrounded, effectively, by an outer solute depleted shell of size such that upon completed precipitation all precipitate particles with their surrounding solute depleted shells occupy the whole volume of the specimen.

For a wide range of nucleation and growth modes the following analytical expression for $x_{p,e}$ for isochronal heating can be given [23]:

$$x_{p,e} = \frac{V}{V_{p,end}} \left(\frac{RT^2}{\Phi} \right)^n \left(\frac{K_0}{Q} \right)^n \exp\left(-\frac{nQ}{RT} \right) \tag{4.8}$$

with the time and temperature independent rate K_0, the overall activation energy Q, the growth exponent $n = d/m + 1$ and $(V/V_{p,end})^{-1}$ as the volume fraction of particles at the end of the reaction.* For extreme cases of nucleation, as site saturation and continuous nucleation (see Eq. (4.1b)), in combination with interface-controlled and diffusion-controlled growth, the growth exponent n adopts values as listed in Table 4.1.

Table 4.1: Values for the growth exponent n in case of site saturation or continuous nucleation in combination with 3-dimensional (d = 3) interface-controlled (m = 1) or diffusion-controlled growth (m = 2).

	interface-controlled growth	diffusion-controlled growth
site saturation ($n = d/m$)	3	3/2
continuous nucleation ($n = d/m + 1$)	4	5/2

The overall activation energy Q can be expressed as a weighted sum of Q_N and Q_G using n and the ratio d/m as weighting factors [26]:

$$Q = \frac{\frac{d}{m} Q_G + \left(n - \frac{d}{m} \right) Q_N}{n}. \tag{4.9}$$

* Note that Eq. (4.8) differs in two aspects from Eq. (31) in Ref. 23: (i) because of the different normalization of f (and $x_{p,e}$), i. e. with respect to $V_{p,end}$ (not V) in the current paper, the fraction $V/V_{p,end}$ appears in Eq. (4.8); (ii) the factor K_0 in Eq. (31) in Ref. 23 is equal to K_0/Q in the present Eq. (4.8), because in Ref. 23 the factor $1/Q$ has been incorporated in the expressions for K_0 given for isochronal annealing in Tables 1 to 3 in Ref. 23.

Fitting the kinetic model by applying Eq. (4.8) in combination with an appropriate impingement correction, e. g. as given by Eq. (4.7), to phase-transformation data obtained from experiment allows for determination of the kinetic parameters K_0, Q and n, which can suffice for an identification of the probably governing nucleation and growth modes (see Table 4.1). In the following this type of kinetic analysis will be referred to as the "general" case.

The kinetic parameters K_0, Q and n can be substituted by analytical expressions, valid upon isothermal or isochronal annealing, as listed in Tables 1 to 3 in Ref. 23 for a range of specific nucleation and growth modes, which describe the transformation kinetics in terms of parameters as N_0, v_0, Q_N and Q_G. However, v_0 and N_0 cannot be determined separately in a subsequent fitting procedure to transformation-rate data, as they always appear in combined fashion, e. g. $(N_0 \cdot v_0^{d/m})$ (see Eq. (4.12a) below), in the expression for $(K_0/Q)^n$. Further, if Q_N and Q_G only appear in Q (see Eq. (4.9)), the fitting also cannot lead to determination of separate values for Q_N and Q_G. Upon isochronal annealing a further combination of Q_N and Q_G (in a way different from Eq. (4.9)) appears in the expression for $(K_0/Q)^n$ (see C_c in Eq. (4.12b) below). Then fitting to the transformation-rate data (here the DSC scans) could in principle lead to separate values of $(N_0 \cdot v_0^{d/m})$, Q_N and Q_G. However, the value of C_c (and thus the value of $(K_0/Q)^n$) is rather insensitive to changes of Q_N and Q_G. Therefore, extra experimental information depending in different ways on $(N_0 \cdot v_0^{d/m})$, Q_N and Q_G has to be incorporated in the model fitting. As demonstrated in this paper such experimental data is provided by e. g. the number density of product particles at the end of the transformation reaction.

4.3 Experimental

A cylindrical ingot with a diameter of 8 mm was produced by melting Cu (99.9995 at. %) and Co (99.995 at. %) under a protective argon atmosphere. The composition was determined to Cu - 0.95±0.01 at. % Co applying inductively coupled plasma – optical emission spectrometry (ICP-OES). The ingot was homogenized at 1333 K for 138 h within a silica capsule filled with a protective argon atmosphere, followed by a quench by breaking the capsules in ice water. Thereafter the ingot was hammered down to a diameter of 5 mm and subsequently cut into discs of about 500 µm thickness. The specimen discs were recrystallized at 1333 K for 48 h and quenched thereafter as described above. Next, the discs were ground and polished using 0.25 µm diamond paste as last step.

Isochronal annealing experiments (leading to Co precipitation) were performed with a differential scanning calorimeter (DSC) Pyris1 from Perkin Elmer. The DSC was calibrated using the temperature and enthalpy of melting of In, Zn and Al. Sample and (empty) reference pan were made of Y_2O_3. For each measurement a new specimen disc was used.

Starting from room temperature, isochronal annealing was performed at heating rates in the range from 5 K min^{-1} to 20 K min^{-1}. Two consecutive heating runs were performed in order to determine the baseline from the second run. In the second run no further reaction was observed.

The microstructure of the specimens prior to and after the DSC runs was investigated by transmission electron microscopy (TEM).

Electron transparent foils for TEM were prepared in three steps: first, the diameter of the discs was reduced from 5 mm to 3 mm by grinding. After this, in a second step, the disc thickness was reduced by grinding from initially 500 µm to about 120 µm. In a third step the discs were electrolytically etched with a D2 electrolyte by Struers using a Tenupol 5 device. TEM was performed using a Zeiss 912 Omega instrument at an accelerating voltage of 120 kV, which is equipped with an energy filter for electron energy loss spectroscopy (EELS). Bright field images in zone axis orientation were recorded with a Gatan digital camera. The particle density and the precipitate-volume fraction after isochronal annealing were calculated by counting the number and measuring the size of all particles visible in the bright field image. The thickness of the foil at the location where the measurements were made was determined by EELS applying the log-ratio method [27]. The accuracy of the thickness measurement with EELS is about ±20%.

Supplementary isothermal annealing experiments were performed for a Cu - 2.13 ±0.03 at. % Co alloy at 843 K. For this alloy, additional high resolution TEM (HRTEM) investigations were made using a Jeol FX 4000 at an acceleration voltage of 400 kV.

4.4 Results and Evaluation

4.4.1 Differential Scanning Calorimetry

The baseline-corrected isochronal DSC curves describing the precipitation of Co from supersaturated Cu - 0.95 at. % Co (for microstructural evidence, see section 4.4.2) measured at heating rates in the range from 5 K min^{-1} to 20 K min^{-1} are shown in Fig. 4.1.

The peak maximum of the resulting differential enthalpy signal $d\Delta H/dt$ shifts towards higher temperature with increasing heating rate. The measured total transformation enthalpy of the precipitation reaction, ΔH_{tot}, was found to be independent of the heating rate and temperature-range: $\Delta H_{tot} = -95 \pm 7$ J mol^{-1}.

The degree of transformation, *f*, was determined as follows

$$f(t) = \left(\frac{V_p(t)}{V_{p,end}} = \right) \frac{\Delta H(t)}{\Delta H_{tot}} \tag{4.10}$$

with ΔH as the cumulative transformation enthalpy obtained by integration of the heat signal $-d\Delta H/dt$ ($-\Delta H(t) > 0$ in case of an exothermic precipitation reaction which is the case here). In case of a precipitation reaction, the definition for *f* expressed by Eq. (4.10) is appropriate if a fixed reference state for the reaction can be assumed, i.e. if $V_{p,end}$, or ΔH_{tot}, is independent of heating rate and temperature.[†] Since ΔH_{tot} was indeed found to be independent of the heating rate (see above), this condition is satisfied.

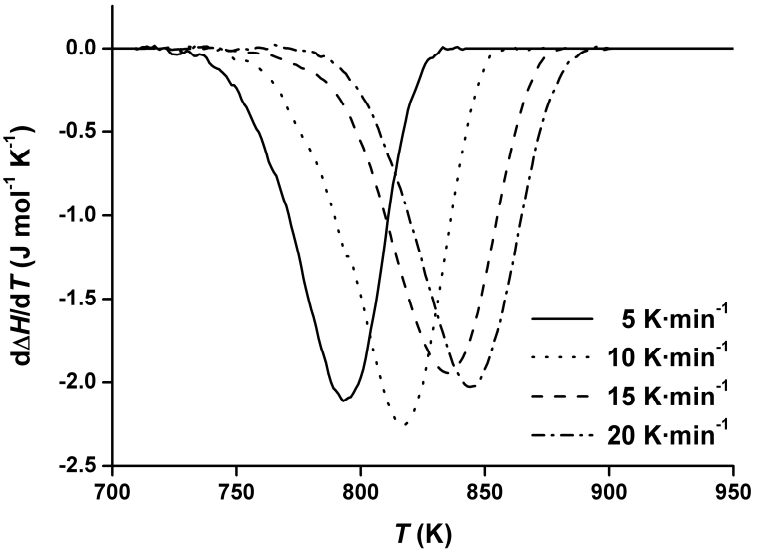

Fig. 4.1: Isochronal baseline corrected DSC-scans of the precipitation of Co at various heating rates for Cu - 0.95 at. % Co.

4.4.2 (HR)TEM

TEM bright-field images and the corresponding selected area diffraction patterns (SADPs) taken prior to and after isochronal annealing with 20 K min^{-1} up to about 900 K, i. e. immediately after the DSC peak (see Fig. 4.1), of Cu - 0.95 at. % Co are shown in Fig. 4.2a and Fig. 4.2b.

[†]This is equivalent to the assumption that the change of the mutual solubilities of Co and Cu is negligible in the temperature range of interest, which is also a prerequisite for adopting Arrhenius temperature dependencies for nucleation and growth (c. f. Ref. 28).

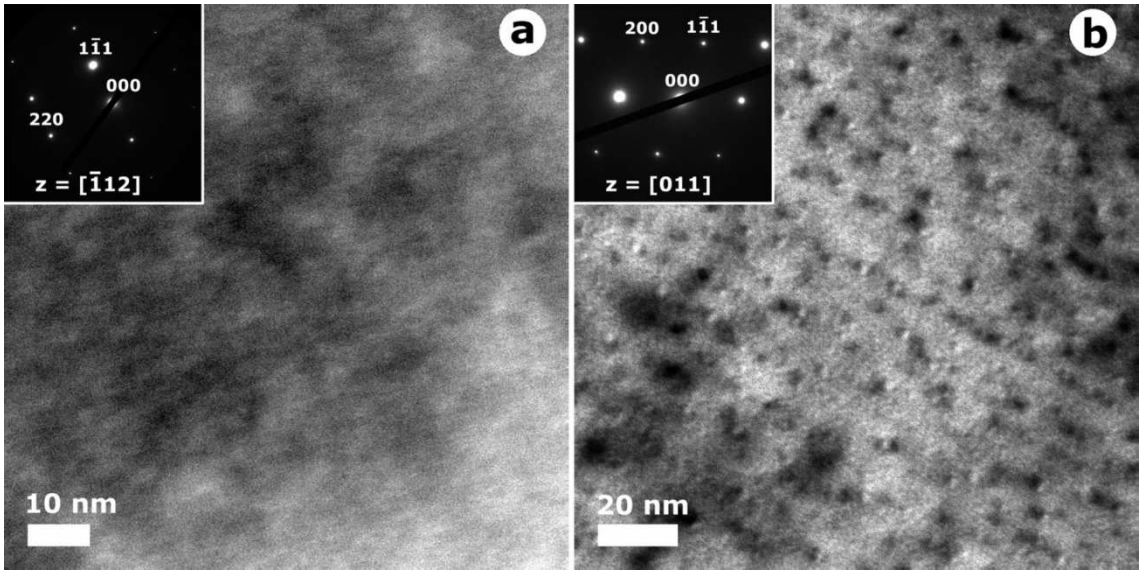

Fig. 4.2: TEM bright field images and the corresponding SADPs (a) prior to and (b) after isochronal annealing with 20 K min^{-1} up to about 900 K, i. e. immediately after the DSC peak (see Fig. 4.1), of Cu - 0.95 at. % Co. (a) No precipitates are visible in the as-quenched state ([-112]$_{Cu}$ zone axis). (b) Small coherent spherical *fcc* Co particles are observed in the annealed state with a particle density of $N_V = 7.19 \cdot 10^{23}$ m^{-3} and a mean particle diameter of $d_m = 1.6$ nm leading to a volume fraction of precipitate equal to 0.147 vol. % ([011]$_{Cu}$ zone axis).

After quenching from about 1333 K to room temperature no precipitation was observed in Cu - 0.95 at. % Co (see Fig. 4.2a). Then, upon isochronal annealing spherical coherent *fcc* Co particles developed in the matrix (see Fig. 4.2b and Fig. 4.3). The particle density was determined as $N_V = 7.19 \cdot 10^{23}$ m^{-3} and the mean particle diameter as $d_m = 1.6$ nm with a particle-diameter range from about 1 nm to 3 nm. This corresponds to a volume fraction of precipitate particles equal to 0.147 vol. % (see section 4.3).

An HRTEM image of a Co nanoparticle, formed in the Cu – 2 at. % Co alloy after isothermal annealing at 843 K for 60 min, is shown in Fig. 4.3. Evidently the nanoparticle has full coherency with the surrounding Cu-rich matrix and exhibits a *fcc* crystal lattice.

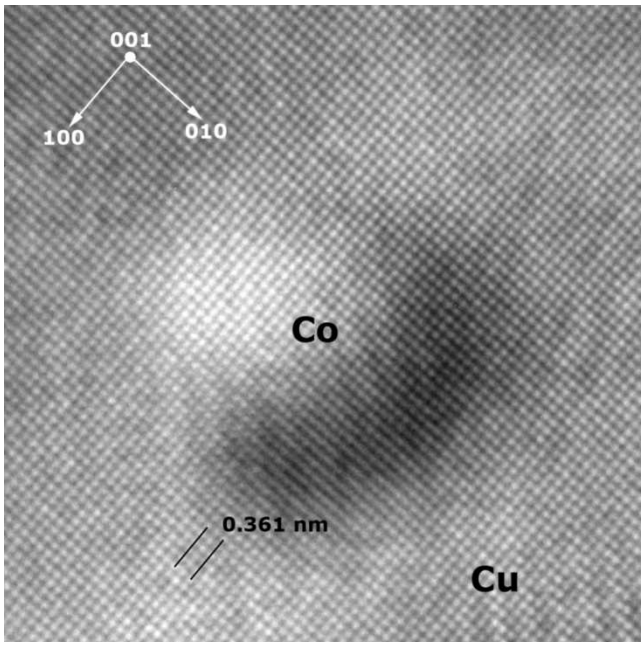

Fig. 4.3: HRTEM image of Cu – 2 at. % Co annealed at 843 K for 60 min ([001] zone axis). The image shows a spherical Co-rich particle fully coherent with the surrounding Cu-rich matrix. The precipitate particle has a *fcc* crystal structure, as well as the matrix.

4.4.3 Analysis of Transformation Kinetics

Values for Q and n can be determined without recourse to any specific model using procedures given in [23, 29]: For isochronal anneals of variable heating rate the effective activation energy Q can be deduced from the temperatures where a specific, chosen degree of transformation is attained, according to a Kissinger-like analysis [29] (Fig. 4.4), and a value for the growth exponent, n, can be deduced from the degree of transformation where a specific, chosen temperature is attained, according to a procedure presented in [23] (Fig. 4.5). The values for the effective activation energy, Q, and the growth exponent, n, as determined by these separate methods have been summarized in Table 4.2.

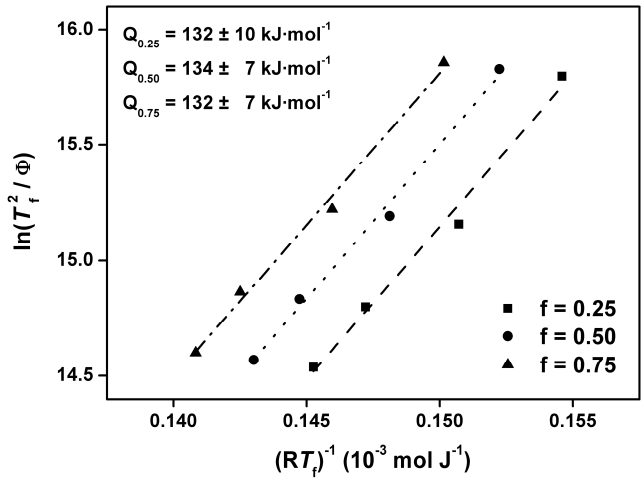

Fig. 4.4: Determination of the effective activation energy according to Kissinger-like analysis for isochronal annealing [29]: plot of $\ln(T_f^2/\Phi)$ vs. $(RT_f)^{-1}$ with Φ as the heating rate and T_f as the temperature at which the degree of transformation attains a specific, chosen value. Results for $f = 0.25$, 0.50 and 0.75 are shown. The slope of the straight line fitted to the data points for constant f yields a value for the effective activation energy, Q. The corresponding values of Q have been indicated in the figure.

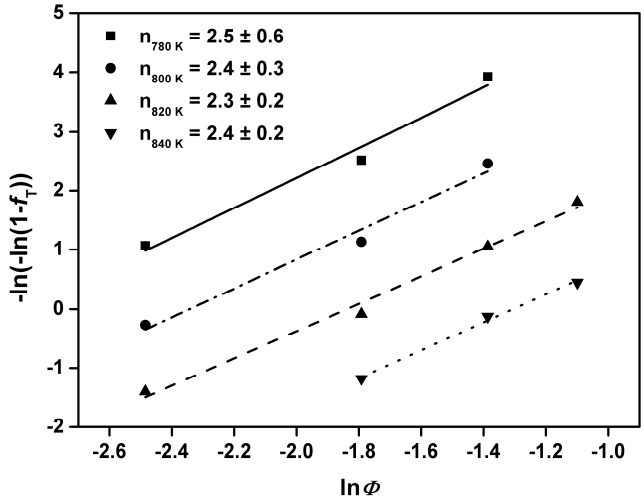

Fig. 4.5: Determination of the growth exponent according to a procedure for isochronal annealing given in [23]: plot of $-\ln(-\ln(1 - f_T))$ vs. $\ln\Phi$ with Φ as the heating rate and f_T as the transformed fraction at which the temperature attains a specific, chosen value. Results for $T = 780$ K, 800 K, 820 K and 840 K are shown. The slope of the straight line fitted to the data points for constant temperature yields a value for the growth exponent n. The corresponding values of n have been indicated in the figure.

The impingement mode can be deduced from a plot of the transformation rate df/dT versus the corresponding transformed fraction f [30]. Such a plot is shown for the present data in Fig. 4.6. All curves show a peak maximum at a value of about 0.6 for the transformed fraction. This value agrees very well with the theoretical value $f = 1 - 1/e$ for the case of an impingement correction as given by Eq. (4.7) (see also Ref. 30) and thereby validates this choice of impingement mode.

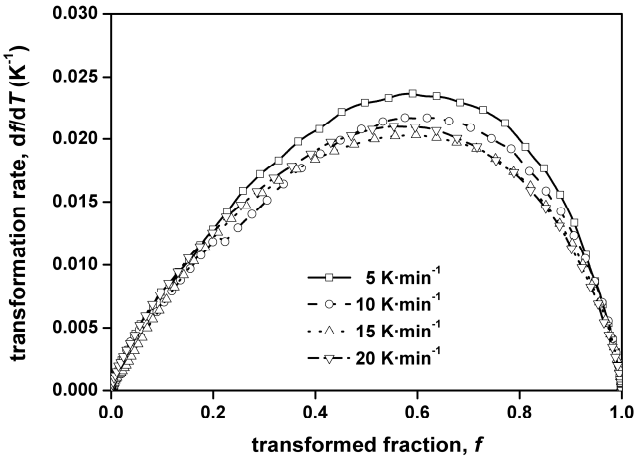

Fig. 4.6: The transformation rate as function of the transformed fraction f (obtained from the data shown in Fig. 4.1). The peak maximum occurs at a value for f equal to about $1 - 1/e \approx 0.6$ which is compatible with Eq. (4.7).

The kinetic parameters K_0, Q and n were determined by fitting the "general" model (combination of Eqs. (4.7) and (4.8)) to *simultaneously* all isochronal heating runs of variable heating rate as recorded from the as-quenched supersaturated Cu – 0.95 at. % Co. Start values for the fit parameters K_0, Q and n were estimated within a physical meaningful range. Then a calculated transformed fraction vs. temperature curve was obtained according to Eqs. (4.7) and (4.8). The mean square error (*MSE*) was defined as the squared difference between the calculated (f_{calc}) and experimental (f_{exp}) transformed fraction curves normalized with respect to f_{exp} for each, i^{th}, of the heating rates applied:

$$MSE = \sum_{i=1}^{n_\Phi} \left[\sum_{\text{data points}} \left(\frac{f_{\mathrm{exp}} - f_{\mathrm{calc}}}{f_{\mathrm{exp}}} \right)^2 \right] \tag{4.11}$$

with n_Φ as the number of heating rates applied. The *MSE* was minimized by varying the fit parameters using a multidimensional unconstrained nonlinear minimization fitting routine as implemented in MATLAB. The results of the fitting as described above are shown in Fig. 4.7 (experimental data: *symbols*; fit: *lines*). The corresponding values for the fitting parameters of the "general" model have been gathered in Table 4.2.

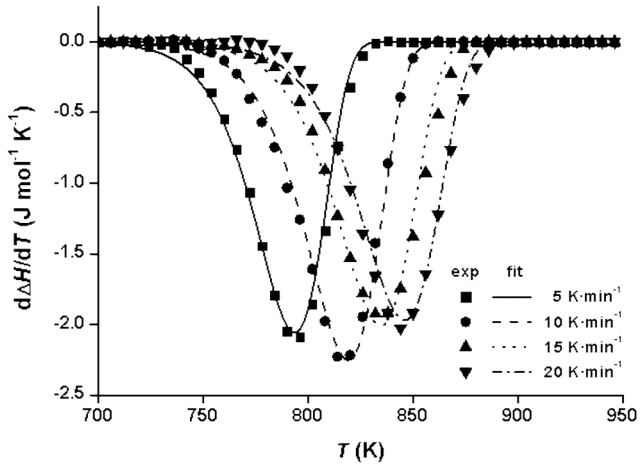

Fig. 4.7: Isochronal DSC curves (symbols) and model fit (simultaneously to all runs) using the modular phase transformation model (K_0, Q and n as fit parameters) for the precipitation of Co from supersaturated Cu - 0.95 at. % Co.

Adopting specific nucleation and growth modes, as site saturation (pre-existing nuclei) or continuous nucleation and diffusion-controlled or interface-controlled growth, the growth exponent n was set to a fixed value (see Table 4.1) and solely K_0 and Q were used as fit parameters. Values obtained for the fit parameters for the above cases of specific nucleation and growth modes have also been listed in Table 4.2.

Table 4.2: Values obtained for the kinetic parameters K_0, Q and n as determined by fitting the modular phase-transformation model for the "general" case as well as for fixed values of the growth exponent n (i. e. fixed modes for nucleation and growth, see Table 4.1) to the experimental data (*MSE* is the mean square error of the fit) and values for the overall activation energy Q and the growth exponent n as determined by model *independent* analysis (Figs. 4 and 5).

model	$\boldsymbol{K_0}$ (s^{-1})	$\boldsymbol{Q}$ (kJ mol^{-1})	$\boldsymbol{n}$	***MSE** (%)*
"general"	$7.6 \cdot 10^4$	134	2.2	2
CN + DCG	$2.9 \cdot 10^4$	126	5/2 (fixed)	4
SS + DCG	$809.0 \cdot 10^4$	174	3/2 (fixed)	18
CN + ICG	$0.2 \cdot 10^4$	101	4/1 (fixed)	68
SS + ICG	$0.8 \cdot 10^4$	115	3/1 (fixed)	17
procedure for Q; Kissinger-like analysis [29]	-	133±8	-	-
procedure for n [23]	-	-	2.4±0.3	-

(CN: continuous nucleation, SS: site saturation, DCG: diffusion-controlled growth, ICG: interface-controlled growth)

Evidently the values for Q and n, as obtained from (i) the general case of the modular phase transformation model, (ii) the modular phase transformation model based on a combination of continuous nucleation and diffusion-controlled growth and (iii) the model-independent, separate methods, agree well. It is also noted that the smallest values for the mean square error of the model fits occur for the cases described under (i) and (ii). Continuous nucleation and diffusion-controlled growth can thus be adopted as nucleation and growth mechanisms controlling the Co precipitation reaction.

For the above identified nucleation and growth modes analytical expressions for Q and K_0 are available: the overall activation energy Q is given by Eq. (4.9) and the rate constant K_0 can be expressed as follows [23]:

$$\left(\frac{K_0}{Q}\right)^n = \frac{gN_0 v_0^{d/m} C_c}{n} \tag{4.12a}$$

with C_c as a correction factor depending on the activation energy values for nucleation, Q_N, and growth, Q_G [31]:

$$C_c = \frac{5}{2}\frac{Q_G^{\frac{1}{2}}\left(3Q_G + 4Q_N\right)}{4Q_N\left(Q_N + \frac{1}{2}Q_G\right)\left(Q_N + Q_G\right)\left(Q_N + \frac{3}{2}Q_G\right)}. \tag{4.12b}$$

The shape factor g for spherical product particles (see Fig. 4.3 and section 4.4.2) is given by $g = 4\cdot\pi/3$. As discussed in section 4.2 fitting of the modular phase-transformation model expressed in terms of fitting parameters as N_0, v_0, Q_N and Q_G to data of the degree of transformation as function of time and/or temperature, in order to find values for these fitting parameters, is partly impossible (in this case for N_0 and v_0, separately) or partly impracticable (in this case for Q_N and Q_G). Involvement of extra experimental information depending on the kinetic parameters in a way different from the transformation-rate data is required. One possible approach is to measure the number of precipitated particles per unit volume, i. e. the product-particle density N_{exp}^{tot}, after completed transformation, i. e. after completion of the peak in the DSC scans (see section 4.4.2 and Fig. 4.2). The product-particle density is related to the (continuous) nucleation rate $\dot{N}$ (see Eq. (4.1b)) and is calculated by

$$N_{calc}^{tot} = \int_0^t \dot{N}(\tau)\left(1 - f(\tau)\right) d\tau \tag{4.13}$$

Applying Eq. (4.13) with the requirement $N_{\mathrm{exp}}^{\mathrm{tot}} = N_{\mathrm{calc}}^{\mathrm{tot}}$ as additional constraint in the fitting now leads to determination of separate values for the parameters N_0, v_0, Q_{N} and Q_{G} by numerical fitting of Eqs. (4.7) and (4.8) to the experimentally determined degree of transformation, f. For that purpose, the total mean square error ($\mathrm{MSE_{tot}}$) is defined as the sum of (a) the mean square error (MSE) for the fitted transformed fraction curves (see Eq. (4.11)) and (b) the squared difference between the calculated ($N_{\mathrm{calc}}^{\mathrm{tot}}$) and experimental ($N_{\mathrm{exp}}^{\mathrm{tot}}$) particle density normalized with respect to $N_{\mathrm{exp}}^{\mathrm{tot}}$ for the isochronal anneal with the largest heating rate (20 K min^{-1}) for which the final particle density was determined by TEM measurement (see section 4.4.2):

$$MSE_{\mathrm{tot}} = \frac{z-1}{z} MSE + \frac{1}{z} \left(\frac{N_{\mathrm{exp}}^{\mathrm{tot}} - N_{\mathrm{calc}}^{\mathrm{tot}}}{N_{\mathrm{exp}}^{\mathrm{tot}}} \right)^2 \Bigg|_{\Phi = 20\,\mathrm{K/min}} \tag{4.14}$$

with z as the total number of experimental data points composed of all heating-rate data points plus one for the particle density.

Fitting of the kinetic model to the degree of transformation rate data (the DSC scans) subjected to the constraint $N_{\mathrm{exp}}^{\mathrm{tot}} = N_{\mathrm{calc}}^{\mathrm{tot}}$ (TEM product-particle density) yielded the following values for the fit parameters: $N_0 = 3.9 \cdot 10^{24}$ s^{-1}, $v_0 = 4.6 \cdot 10^{-10}$ m^2 s^{-1}, $Q_{\mathrm{N}} = 50$ kJ mol^{-1} and $Q_{\mathrm{G}} = 177$ kJ mol^{-1}. The fitted transformation curves are shown in Fig. 4.8 (experimental data: *symbols*; fit: *lines*).

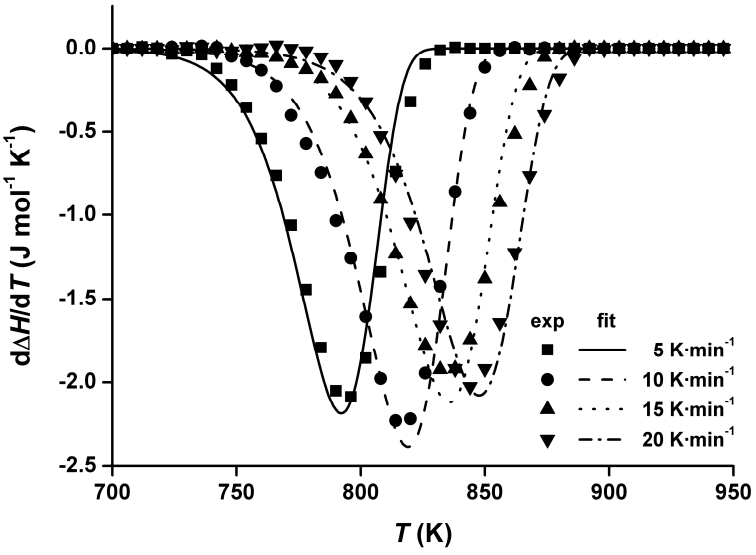

Fig. 4.8: Isochronal DSC curves (symbols) and model fit (simultaneously to all runs) using the modular phase transformation model (continuous nucleation and diffusion-controlled growth with N_0, v_0, Q_{N} and Q_{G} as fit parameters and the experimentally determined particle density $N_{\mathrm{v,exp}}$ as additional boundary condition) for the precipitation of Co from supersaturated Cu - 0.95 at. % Co.

4.5 Discussion

The as-quenched Cu - 0.95 at. % Co alloy exhibits a homogeneous precipitate-free microstructure (Fig. 4.2a). Upon precipitation spherical, coherent, *fcc* Co particles develop, as revealed by HRTEM (Fig. 4.3). The low-temperature *hcp* Co phase was not observed, indicating the very small difference in bulk energy of the *fcc* and *hcp* modifications [32]. The spherical shape, and possibly the preservation of the *fcc* structure at room temperature, of the small coherent particles may be ascribed to a delicate interplay of elastic strain energy and interface energy [33].

The TEM analysis in combination with EELS yielded a precipitate-volume fraction of Co of 0.147 vol.% (section 4.4.2) immediately after completion of the exothermic peak in DSC, whereas for a total separation into phases with equilibrium concentrations as given by the phase diagram [12], a volume fraction of precipitates of about 0.89 vol.% is expected for a Cu - 0.95 at. % Co alloy. Before interpretation of this observed discrepancy can occur two possible error sources must be taken into consideration: (a) The determination of the specimen volume with EELS and (b) the measurement of the particle size:

(a) The accuracy of the thickness measurement is ±20% [27]. The measurement of lateral distances in the digitalized TEM image can occur with an accuracy of about ±2%. This leads to an accuracy of the volume determination of about ±25%.

(b) The measurement of the particle diameter is based on an estimate of the position of the centre line in the ring of strain contrast. The inaccuracy of the value thus determined for the particle size is estimated at ±0.2 nm [18].

This [(a) + (b)] leads to a range for the measured precipitate-volume fraction from 0.078 vol. % to 0.280 vol. %, still clearly remote from the expected equilibrium value.

DSC measurements revealed that the total enthalpy change associated with the precipitation reaction is about -95±7 J mol^{-1} (see section 4.4.1). The enthalpy of decomposition according to the reaction $(Cu,Co)_{fcc} \rightarrow (Cu)_{fcc} + (Co)_{fcc}$ can be assessed adopting the regular solution model for the solid solution with a, for dilute solid solutions, concentration independent interaction parameter Ω = 37048 J mol^{-1} [34]. At a temperature of about 1000 K, the here recorded transformation enthalpy corresponds to a precipitate-volume fraction of about 0.181±0.014 vol.%. This result agrees well with the above discussed range of values for the precipitate-volume fraction as determined by TEM (plus EELS).

Hence, the discrepancy between the expected precipitate-volume fraction of about 0.89 vol.% for total decomposition and the experimentally observed precipitate-volume fraction of about 0.147 vol.% indicates that, at the apparent end of the reaction represented by the exothermic peak in the DSC scans (Fig. 4.1), a significant fraction of Co (here 0.8 at. %) still is dissolved.

Understanding of this observation is provided by the additional isothermal annealing experiments, performed in the present project, for the Cu - 2.13 at. % Co alloy at 843 K: as demonstrated by particle density measurements with TEM, no further Co particles nucleated after 15 min annealing. The solute concentration in the matrix measured with EDX at this stage still was 1.7±0.3 at. %, being compatible with the Co particle density and size distribution as determined by TEM. Continued annealing showed that the Co particle size increased with a simultaneous decrease of the particle density and a decline of the solute concentration in the matrix down to 0.4±0.2 at. % after 6000 min of annealing. Hence, after an initial rapid nucleation and growth stage continued precipitation of Co is realized by a considerably slower process of growth only, accompanied by simultaneous coarsening.

The exothermic DSC peak (Fig. 4.1) can therefore be ascribed to an initial stage of Co precipitation by nucleation and growth with a rapid increase of the precipitate-volume fraction and thus with pronounced heat release. Then nucleation effectively comes to a halt. The later stages of growth and coarsening are not well detectable with DSC due to the very small amount of released heat per unit of time.

Because of the abrupt diminution of the reaction rate after the initial stage of the precipitation reaction manifested by the exothermal DSC peak, it appears reasonable to treat this nucleation and growth dominated part of the overall precipitation reaction as a separate reaction and to define a degree of transformation f with $0 \leq f \leq 1$ by choosing the state of transformation immediately at the end of this first stage as reference state (cf. Eq. (4.10)).

The evaluation of the Co precipitation kinetics based on such considerations (section 4.4.3) revealed that the precipitation of Co, as corresponding to the peaks in the isochronal DSC runs, can be described by continuous nucleation in combination with diffusion-controlled growth. This result is in agreement with the values obtained for Q and n by the methods independent of a specific model (see Fig. 4.4 and Fig. 4.5) and also with the microstructure: The formation of spherical precipitates (Fig. 4.2b and Fig. 4.3) suggests 3-dimensional growth ($d = 3$). The growth exponent n as determined by the model independent analysis (Fig. 4.5) equals 2.4±0.3. Within experimental accuracy this value is (only) compatible with diffusion-controlled growth and continuous nucleation satisfying the equation $n = d/m + 1 = 5/2$ [23].

Using additional information, i.e. the particle density immediately after the exothermic peak in DSC, values for the kinetic parameters N_0, v_0, Q_N and Q_G could be obtained. For the activation energy of nucleation, a value of $Q_N = 50$ kJ mol^{-1} and for the activation energy of growth, a value of $Q_G = 177$ kJ mol^{-1} were obtained.

The value of the activation energy for tracer-volume diffusion of Co in Cu [35] is about 214 kJ mol^{-1}, thus being significantly larger than the value determined for Q_G. It can be assumed that (a significant amount of) quenched-in vacancies have been retained at the onset of Co precipitation upon isochronal annealing. Preservation of quenched-in vacancies was also found for the isochronal precipitation of Co_2Si from Cu - 1 at. % Co_2Si [36] and of CoTi from Cu - (1) at. % (CoTi) [37]. In particular a bonding of quenched-in vacancies to solute Co atoms could occur [38]. In the extreme case this can imply that the vacancy-formation energy is no longer part of the activation energy for Co diffusion. Consequently, the expected value for the activation energy of Co diffusion in the Cu-rich matrix can be considerably reduced as compared to the activation energy for bulk (tracer) diffusion of Co in Cu. This consideration leads to the conclusion that quenched-in vacancies likely contribute to the kinetics of precipitation of the nano-sized *fcc* Co precipitate particles in the Cu-rich matrix.

The occurrence of a defined initial stage of continuous nucleation and diffusion-controlled growth, with a significant fraction of Co remaining in solution at the end of this initial stage may be interpreted in terms of classical nucleation theory, as follows. For precipitation reactions, the Gibbs energy for formation of a particle of critical size, ΔG^*, strongly depends on the degree of supersaturation (Ref. 24). For large degrees of supersaturation, as is the case for the here applied experimental conditions at the beginning of the heat treatment, ΔG^* is distinctly smaller than the activation energy for nucleation Q_N, and nucleation can be well described by continuous nucleation (Eq. (4.2)).

With a decreasing degree of supersaturation of the matrix, i.e. with increasing solute depletion by precipitation, ΔG^* increases which can lead to a sharp decline of the nucleation (c.f. Eq. (4.1), note that in the modeling approach applied here the solute depletion of the matrix is accounted for by the impingement correction). The precipitation process then can only be completed by growth, in combination with simultaneous coarsening, which is a comparatively slow process as indicated by the large difference in activation energies obtained in this work for nucleation, Q_N (50 kJ mol^{-1}), and growth, Q_G (177 kJ mol^{-1}).

4.6 Conclusions

- The precipitation of *fcc* Co from supersaturated Cu - 0.95 at. % Co solid solution is governed by continuous, random nucleation and diffusion-controlled, isotropic growth, as described by the modular phase-transformation model.
- Fitting of the kinetic model to isochronal transformation-rate data, as exhibited by DSC scans, subject to additional constraints as for example provided by microscopic (TEM) product particle-density analysis, allows determination of the kinetic parameters characterizing the separate nucleation and growth modes.
- The effective, overall activation energy of about 133±8 kJ mol^{-1} can (thus) be separated into separate activation energies of nucleation and growth of 50 kJ mol^{-1} and 177 kJ mol^{-1}, respectively.
- Nucleation is found to come to a halt long before all Co dissolved in the Cu-rich matrix has precipitated. Continued precipitation can only be realized by growth, accompanied by simultaneous coarsening, which, as indicated by the activation energies of nucleation and growth, is a relatively slow process.
- The activation energy of growth is distinctly smaller than the activation energy for volume diffusion of Co in equilibrated Cu due to the presence of quenched-in excess vacancies.

References

[1] E. J. Mittemeijer and F. Sommer, *Z Metallkd* **93** (2002) 352.
[2] A. T. W. Kempen, F. Sommer, and E. J. Mittemeijer, *Acta Metall Mater* **50** (2002) 1319.
[3] A. T. W. Kempen et al., *Metall Mater Trans A* **33A** (2002) 1041.
[4] H. Nitsche, F. Sommer, and E. J. Mittemeijer, *Metall Mater Trans A* **37A** (2006) 621.
[5] H. Nitsche et al., *Z Metallkd* **96** (2005) 1341.
[6] H. Nitsche, F. Sommer, and E. J. Mittemeijer, *J Non-Cryst Solids* **351** (2005) 3760.
[7] F. Liu, F. Sommer, and E. J. Mittemeijer, *Acta Metall Mater* **52** (2004) 3207.
[8] A. T. W. Kempen, F. Sommer, and E. J. Mittemeijer, *Acta Metall Mater* **50** (2002) 3545.
[9] Y. C. Liu, F. Sommer, and E. J. Mittemeijer, *Acta Metall Mater* **51** (2003) 507.
[10] Y. C. Liu, F. Sommer, and E. J. Mittemeijer, *Acta Metall Mater* **54** (2006) 3383.
[11] W. Baumann, A. Leineweber, and E. J. Mittemeijer, Max Planck Institute for Metals Research, Stuttgart, Germany, submitted for publication, June 2010 .
[12] T. Nishizawa and K. Ishida, *B. Alloy Phase Diagrams* **5** (1984) 161.
[13] V. A. Phillips and J. D. Livingston, *Phil Mag* **7** (1962) 969.
[14] J. B. Hess and C. S. Barrett, *J Met* **4** (1952) 645.
[15] M. F. Ashby and L. M. Brown, *Phil Mag* **8** (1963) 1083.
[16] P. Villars and L. D. Calvert, *Pearson's Handbook of Crystallographic Data for Intermetallic Phases 2*, ASM International, Materials Park, Ohio, 1996.
[17] S. Matsumura, M. Toyohara, and Y. Tomokiyo, *Phil Mag* **62** (1990) 653.
[18] R. Hattenhauer and F. Haider, *Scr Metall Mater* **25** (1991) 1173.
[19] F. K. LeGoues and H. I. Aaronson, *Acta Metall Mater* **32** (1984) 1855.
[20] J. D. Robson, *Mat Sci Techn* **20** (2004) 441.
[21] R. Kampmann, T. Ebel, and M. Haese, *Phys Status Solidi* **172** (1992) 295.
[22] R. P. Setna et al., *Appl Surf Sci* **67** (1993) 368.
[23] F. Liu et al., *IntMat Rev* **52** (2007) 193.
[24] J. W. Christian, *The Theory of Transformations in Metals and Alloys*, Part 1 (Chapter 46), 3rd edt., Pergamon, Oxford (UK), 2002.
[25] C. Wert and C. Zener, *J Appl Phys* **21** (1950) 5.
[26] A. T. W. Kempen, F. Sommer, and E. J. Mittemeijer, *J Mat Sci* **37** (2002) 1321.
[27] R. F. Egerton, Electron Energy-Loss Spectroscopy in the Electron Microscope. 2nd edt., Plenum Press, New York, 1996.
[28] M. B. Berkenpas et al., *Scr.Metall Mater* **20** (1986) 323.
[29] E. J. Mittemeijer, *J Mat Sci* **27** (1992) 3977.
[30] F. Liu et al., *Acta Metall Mater* **57** (2009) 6176.
[31] F. Liu, F. Sommer, and E. J. Mittemeijer, *J Mat Sci* **39** (2004) 1621.
[32] A. T. Dinsdale, *Calphad* **15** (1991) 317.
[33] D. A. Porter and K. E. Easterling, *Phase Transformations in Metals and Alloys*. 2nd edt., Nelson Thornes Ltd, 2001.
[34] M. A. Turchanin and P. G. Agraval, *Powder Metall Met C+* **46** (2007) 77
[35] R. Döhl, M. P. Macht, and V. Naundorf, *Phys Status Solidi A* **86A** (1984) 603.

[36] A. Varschavsky and E. Donoso, *J Therm Anal Calorim* **74** (2003) 41.
[37] E. Donoso, G. Diaz, and J.M. Criado, *J Therm Anal Calorim* **91** (2008) 491.
[38] L.A. Girifalco and H. Herman, *Acta Metall Mater* **13** (1965) 683.

5 Kinetics of the Allotropic *hcp-fcc* Phase Transformation in Cobalt

R. Bauer, E. A. Jägle, W. Baumann and E. J. Mittemeijer

Abstract

The allotropic, martensitic phase transformation *hcp→fcc* in cobalt was investigated by differential scanning calorimetry (DSC) upon isochronal annealing at heating rates in the range from 10 K min^{-1} to 40 K min^{-1}. The microstructural evolution was traced by light optical microscopy (LM) and X-ray diffractometry (XRD). The kinetics of the phase transformation from *hcp* to *fcc* Co upon isochronal annealing was described on the basis of a modular phase transformation model. Appropriate model descriptions for athermal nucleation and thermally activated, anisotropic interface-controlled growth tailored to the martensitic phase transformation of Co were implemented into the modular model. Fitting of this model of phase transformation kinetics to simultaneously all isochronal DSC runs yielded values for the energy of the interface separating the *hcp* and *fcc* Co phase and the activation energy for growth.

5.1 Introduction

Pure cobalt exhibits an allotropic phase transformation at the equilibrium temperature T_0 (at constant pressure) with the *hcp* modification as low temperature phase and the *fcc* modification as high temperature phase. This allotropic transformation shows characteristics of a martensitic transformation [1, 2]: the transformation needs no diffusion and composition change, has a distinct athermal nucleation nature leading to spontaneous initiation of the reaction upon reaching the "martensite" start temperature M_S upon cooling or the "austenite" start temperature A_S upon heating.

Many studies on the mechanism and microstructural evolution associated with the allotropic phase transformation in Co have been performed (e. g. see Refs. 1 - 17), providing controversial or inconclusive results on a number of aspects: The equilibrium temperature and its uncertainty as given in Ref. 4, $T_0 = 690 \pm 7$ K (at 1 atm), covers the range of most of the available literature data [2, 9, 11, 18], based on calculations or determined experimentally, taken as average of the "austenite" and "martensite" start temperatures, measured by X-ray diffractometry, magnetometry, dilatometry or calorimetry. Values for the martensite start temperature M_S range from 692 K to 661 K and for the austenite start temperature A_S range from 694 K to 720 K [2, 7, 10]. The difference between the start temperatures for the *fcc*→*hcp* transformation (M_S temperature) and the *hcp*→*fcc* transformation (A_S temperature) is called (here) "temperature hysteresis". Values for the enthalpy of transformation, $\Delta H_{hcp \leftrightarrow fcc}$, range from 377 to 464 J mol^{-1} [1, 2, 9, 11, 18] and some studies indicate differences upon heating and cooling [10, 15]. The diversity of these results appears to depend on the specimen shape (thin layer [6, 16, 17], powder [3, 5, 12], sheet [8, 10, 13, 15] and rod [1, 3, 5, 7]), the specimen size [10, 15], the state of stress [7, 12] and the (type of) thermal treatment [1, 3 - 8, 10, 12, 15].

It appears that depending on the initial microstructure and experimental conditions (as heating/cooling rate) a significant number of *hcp*↔*fcc* transformation cycles must be passed through in order to establish reproducible characteristics of the *hcp*↔*fcc* transformation (see Refs. 1, 2, 5, 10, 15, 19 and, in particular, results of this study presented in section 5.4). This may contribute to the discrepancies apparent from the literature cited above.

A full, quantitative, description of the kinetics of the allotropic transformation in Co was not presented until now. The present paper for the first time provides such a model description of the allotropic, martensitic transformation kinetics of Co, departing from a general modular model of phase-transformation kinetics composed of separate modes of nucleation, growth and impingement [20, 21], thereby incorporating an athermal nucleation mode as proposed in Ref. 19, interface-controlled growth and anisotropic impingement. This approach was recently applied successfully by our group to the polymorphic transformation of Laves phases [22].

The present paper focuses on the *hcp→fcc* phase transformation using "stabilized" specimens (i. e. after a number of preceding transformation cycles). Isochronal annealing experiments in a fixed temperature range using Differential Scanning Calorimetry, DSC, were performed. The resulting enthalpy changes as function of time and heating rate were interpreted quantitatively using the modular phase transformation model.

5.2 Theoretical Background of Transformation Kinetics

Solid state phase transformations can take place as soon as the hitherto existing phase is not stable anymore; i. e. a thermodynamic driving force can be indicated. Such a phase transformation can be realized in different ways. In general a phase transformation can be subdivided into three (overlapping) steps: nucleation, growth and impingement. This type of modular approach has been described in [20, 23] (see, especially, the review in Ref. 21) and has been applied successfully to a variety of phase transformations: crystallization of amorphous metal alloys [24 - 29], the austenite-ferrite transformation in Fe-based alloys [30 - 32] and the polytypic transformations of Laves phases [22].

Assuming, hypothetically, that each individual product *particle*, emanating from a successful nucleation process, grows into an infinitely large parent phase, in the absence of other product particles, the so-called extended volume, V_e, given by the sum of the volumes of all these (hypothetical) particles, can be calculated. In a second step the extended transformed fraction, x_e (= V_e / V_S; with V_S as the volume of the specimen), has to be corrected for (*hard*) *impingement* to obtain the *real* transformed fraction, *f*, by adopting a certain impingement mode. In the following, after discussing the *hcp↔fcc* transformation mechanism, nucleation, growth and impingement modes relevant for the *hcp↔fcc* transformation are indicated briefly.

5.2.1 The *hcp*↔*fcc* Transformation Mechanism

The dislocation (line) energy of a so-called perfect dislocation can be reduced by dissociation into two Shockley partial dislocations inducing a stacking fault (SF) in-between both partials, with the stacking fault energy (SFE) σ. The width of the dissociated partial dislocations is given by the balance of the elastic repulsion force, forcing the dissociation, and the stacking fault energy, σ, opposing the dissociation: dissociated (perfect) dislocations are a basic component of the microstructure [33].

The transformation of an *fcc* (ABCABC… stacking sequence) into an *hcp* (ABABAB… stacking sequence) crystal structure, and vice versa, can be realized by the motion of Shockley partial (SP) dislocations, with Burgers vectors, of type $1/6\langle 11\bar{2}\rangle$, on every second closest packed plane [6, 19].

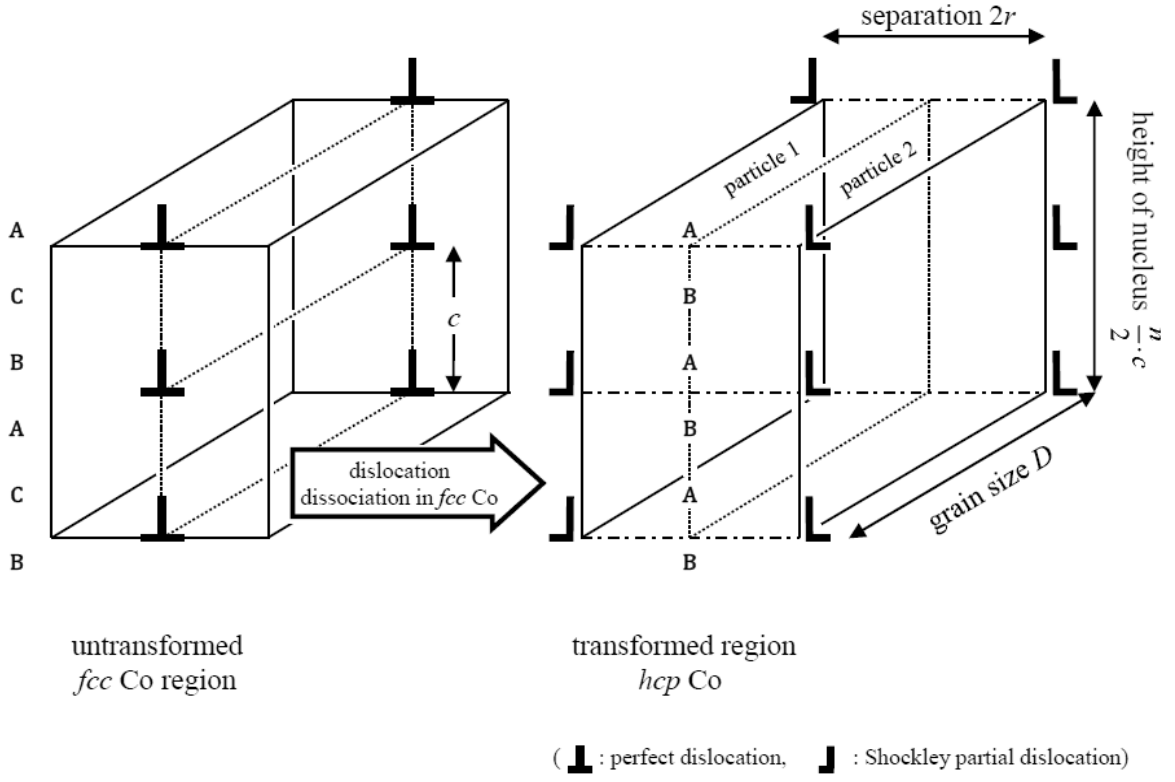

Fig. 5.1: Schematic view of an *hcp* nucleus (ABABAB… stacking sequence) developing in an *fcc* matrix (ABCABC… stacking sequence) by dissociation of three perfect dislocations in *fcc*. *Left*: Array of three perfect dislocations in the *fcc* Co phase (before dissociation); *right*: two arrays each consisting of three Shockley partial dislocations; the two arrays build up two particles consisting of the *hcp* phase, each particle having a volume determined by the grain size *D*, the height of the defect structure (depending on the number of Shockley partial dislocations within the array) and half of the separation distance, 2*r*, realised by glide of the Shockley partial dislocations.

This process can be called "ordered glide" as an ordered array of Shockley partials is required for the phase transformation. So this ordered array of *x* partials transforms a region of thickness 2*x* closest packed layers. The transformation *fcc*→*hcp* occurs by dissociation of the perfect dislocations and the transformation *hcp*→*fcc* by association of the SPs (see Fig. 5.1). Studies of the microstructural evolution upon thermal (transformation) cycling showed that such ordered dislocation arrangements evolve indeed [6], establishing, by the "back and forth" movement of the same partial dislocations, the reversible *hcp*↔*fcc* transformation with preservation of the orientation, in the specimen frame of reference, of the *hcp* and *fcc* crystals, as validated for Co [1].

Each SP can be associated with one of six Burgers vectors of type $1/6\langle 11\bar{2}\rangle$ on a closest packed plane leading, upon glide of the SP, to a *microscopic shear* of the lattice (see top part in Fig. 5.2). This shear can be nullified (no add up of *microscopic* to *macroscopic* shear) by the summation of a set of three successive dislocations in the ordered array of SPs, with Burgers vectors such that $\vec{b}_1+\vec{b}_2+\vec{b}_3=0$ (see bottom left part in Fig. 5.2). If $\vec{b}_1+\vec{b}_2+\vec{b}_3\neq 0$, macroscopic shear evolves* (see bottom right part in Fig. 5.2 where the extreme case, all SPs have same $\vec{b}$, is shown). However, it is usually assumed [13, 14] that microscopic shear cancels out over short distances and therefore the contribution of macroscopic shear to the phase transformation (kinetics) is considered to be negligible in this paper.

* Note that for polymorphic Laves-phase transformations such macroscopic shear is impossible because of the glide of synchro-Shockley partial dislocation *dipoles* [22].

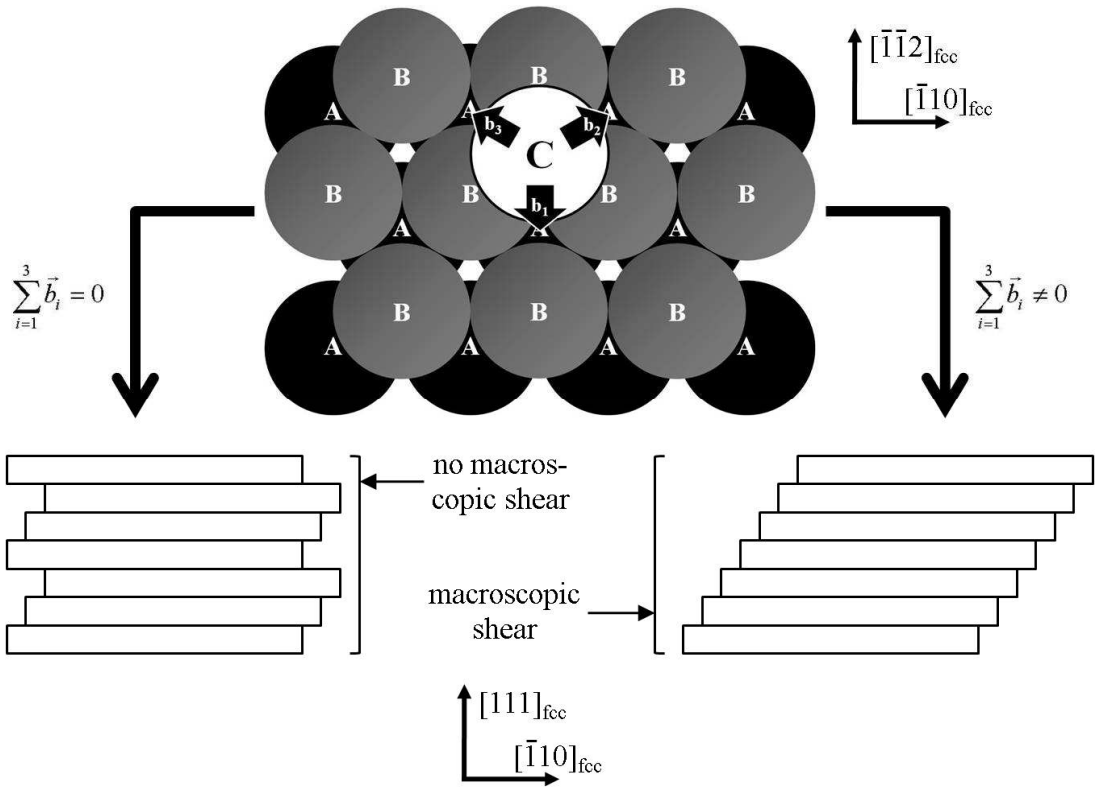

Fig. 5.2: Stacking sequence of an *fcc* crystal lattice (*top*). The black arrows indicate possible Burgers vectors available for the glide process of Shockley partial dislocations upon the *fcc→hcp* transformation. *Bottom left*: Burgers vectors of Shockley partial dislocations in every second closest packed plane oriented such that for three successive Shockley partials (i. e. comprising a stack of six closest packed planes) $\vec{b}_1 + \vec{b}_2 + \vec{b}_3 = 0$. No macroscopic shear occurs. *Bottom right*: Shockley partial dislocations, gliding on every second closest packed plane with the same Burgers vector. This leads to macroscopic shear.

Irrespective of the micro-/macroscopic shear discussed above, the allotropic transformation in cobalt is associated with a *macroscopic distortion* due to the change of the atomic distances. This macroscopic distortion for the *fcc→hcp* transformation is +0.021% parallel to and -0.242% perpendicular to the closest packed plane [13].

The *hcp* crystal lattice has only one closest packed set of {0001} planes; the *fcc* crystal lattice has four equivalent sets of closest packed {111} planes. Upon thermal cycling the dislocation structure is (re)arranged, from any initial state, such, that only one single set of $\{111\}_{fcc}$ planes is active and parallel to $\{0001\}_{hcp}$ (further see section 5.6.1).

5.2.2 Nucleation

The thermodynamic model for nucleation must be compatible with the mechanism for the *hcp↔fcc* transformation by glide of an ordered array of Shockley partial dislocations (cf. section 5.2.1). The model presented here is derived from an earlier description of nucleation of the martensitic *fcc→hcp* transformation in metals by dissociation of perfect dislocations [19].

Consider the periodically arranged array of *perfect* dislocations in an *fcc* crystal as shown in Fig. 5.1 and Fig. 5.3. The *fcc*↔*hcp* phase transformation is performed by glide of the periodically arranged Shockley *partial* dislocations through the crystal lattice (see section 5.2.1)

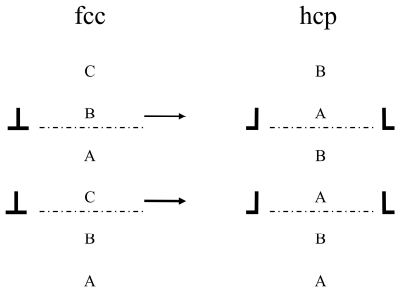

Fig. 5.3: Ordered arrays of Shockley partial dislocations gliding through an *fcc* Co crystal leaving behind the *hcp* Co structure (see also Fig. 5.1).

Initiation of an *fcc*→*hcp* transformation requires dissociation of the array of perfect dislocations into two arrays of Shockley partial dislocations. The region in between these two arrays can be described as a stacking faulted region (with reference to the parent structure) or as transformed region (exhibiting the product, *hcp* crystal structure). As long as *fcc* is the stable phase, the dissociation is limited by the relatively high energy (with reference to the parent phase) of the faulted structure lying between the two arrays of Shockley partial dislocations. This is no longer the case if the *hcp* phase becomes the stable phase, i.e. by passing the *hcp-fcc* phase equilibrium temperature T_0 upon (isochronal) cooling from the *fcc* phase field.

The region between the two separated arrays of Shockley partial dislocations can be considered as two second-phase (*hcp*) particles each having the volume V and the interfacial area S. The total Gibbs energy change ΔG associated with the formation of this second phase particle can be given as:

$$\Delta G = V\left(\Delta G_V^{ch} + E_V^{str}\right) + S\sigma \tag{5.1}$$

where ΔG_V^{ch} $(= \Delta G_m^{ch} / V_m$; ΔG_m^{ch} is the chemical Gibbs energy difference per mole of atoms between product phase and parent phase and V_m is the molar volume) is the chemical Gibbs energy difference between product phase and parent phase per unit volume, E_V^{str} $(= E_m^{str} / V_m$; E_m^{str} is the elastic strain energy per mole of atoms) is the elastic strain energy per unit volume and σ is the particle/matrix interface energy per unit area. For small overheating/undercooling, i.e. in the vicinity of the equilibrium phase-transformation temperature T_0, the chemical Gibbs-energy change per mole of atoms ΔG_m^{ch} can be approximately given as:

(5.2) $$\Delta G_m^{ch} \cong \frac{\Delta H_{hcp\leftrightarrow fcc}}{T_0}\left(T_0 - T\right) = \frac{\Delta H_{hcp\leftrightarrow fcc}}{T_0}\Delta T$$

with $\Delta H_{hcp\leftrightarrow fcc}$ as the molar enthalpy of transformation (*fcc*→*hcp*: $\Delta H < 0$, *hcp*→*fcc*: $\Delta H > 0$) and ΔT as the undercooling/overheating. The molar chemical Gibbs energy change ΔG_m^{ch} corresponds to the chemical driving force for the transformation and, as evident from Eq. (5.2), it changes its sign at T_0. The elastic strain energy per unit volume, E_V^{str}, cannot be neglected since the product and the parent phases have unequal molar volumes (see section 5.5).

The volume of a product-phase particle is given by

(5.3) $$V = \frac{n}{2} c \cdot r \cdot D$$

with nc / 2 as the height/size of the nucleus; n / 2 is the number of dislocations within the array of dislocations oriented perpendicular to the stacking direction (cf. Fig. 5.1 and Fig. 5.3; n is the number of closed packed layers in the stack considered and c is the distance between adjacent dislocations in the array parallel to the c-axis (c_{hcp} = 0.40686 nm, $c_{fcc} = (2/3)\cdot\sqrt{3}\cdot a_{fcc}$ = 0.40931 nm [34]), $2r$ is the separation distance of the partial dislocations (r is the distance passed by one array of Shockley partial dislocations) and D is the grain size of the parent crystal (cf. Fig. 5.1).

The newly created interfacial area S of one particle is given by the top and the bottom side and the front and the rear side of the product-phase particle (as shown in Fig. 5.1). Because $D \geq nc/2$ the interfacial area S is approximately given by the top and bottom sides and thus:

(5.4) $$S \approx 2rD\,.$$

It follows from Eqs. (5.1), (5.3) and (5.4):

(5.5) $$\Delta G_A \equiv \frac{\Delta G}{rD} = n\frac{c}{2V_m}\left(\Delta G_m^{ch} + E_m^{str}\right) + 2\sigma\,.$$

The term $\Delta G / rD$ corresponds to the energy difference between the product phase/particle and parent phase per unit area top/bottom interface, ΔG_A. Note that both the volume chemical energy term as well as the interface energy term scale with r.

Evidently, a critical size (a critical value of r) does not occur (cf. Eq. (5.5)): The transformation can take place "spontaneously", i.e. without overcoming an energy barrier by thermal activation, provided that the energy difference between the product phase (lying in-between the dissociated dislocation arrays) and parent phase per unit area, ΔG_A, becomes negative, e.g. by a change of temperature (cf. Eqs. (5.2) and (5.5)). Hence, the product-phase particles develop by athermal nucleation.

The interfacial term 2σ in Eq. (5.5) is independent of the height nc / 2 of the possibly operating dislocation array, whereas the chemical Gibbs energy change for operation of the same dislocation array $\left(= nc\Delta G_m^{ch}/2V_m\right)$ increases with n. For a fixed value of n the energy difference per unit area top/bottom interface, ΔG_A, equals zero at a finite value of undercooling, $\Delta T = T_0 - T$, for the *fcc*→*hcp* transformation (or rather overheating, $\Delta T = T_0 - T$, for the *hcp*→*fcc* transformation). A distribution of heights of the arrays of dislocations (corresponding with a varying number of closed packed layers, n, in the stack considered) is supposed to exist in the *fcc* crystal. It follows from Eq. (5.5) that the larger the height of the dislocation array, i.e. the larger n, the lower the required undercooling in order that this dislocation array starts to produce by glide a product-phase (*hcp*) particle. In other words, the nucleation event can be described as a kind of site saturation at each temperature, where dislocation arrays of specific height start to operate.

At a given undercooling, $\Delta T(t) = T_0 - T(t)$, the critical (minimal) value of n, i. e. n^*, indicating the minimal height of the dislocation array for realising by glide the *fcc*→*hcp* transformation, satisfies (see Eqs. (5.2) and (5.5)):

$$n^*\left(\Delta T(t)\right) = -\frac{2\sigma}{\frac{c}{2V_m}\left(\frac{\Delta H_{hcp\leftrightarrow fcc}}{T_0}\left(T_0 - T\right) + E_m^{str}\right)}. \tag{5.6}$$

Depending on the values of the parameters at the right-hand side of Eq. (5.6), as σ, ΔH and E_m^{str}, a minimum number of stacked dislocations can be designated from n^* in order to obtain a stable nucleus that can grow. For example, considering the *hcp*→*fcc* transformation above $T_0 = 690$ K, if $\Delta H_{hcp\rightarrow fcc} = 501$ J mol^{-1}, $\sigma = 10$ mJ m^{-2} [8], $E_m^{str} = 0.838$ J m^2, it follows $n^* = 32$ at $T = 720$ K and $n^* = 24$ at T=730 K. Upon decreasing temperature more and more dislocation arrays of decreasing height can become active. From experimental data for the martensitic transformation in Fe 30.2 wt% Ni, it was proposed that the cumulative number of operating dislocation arrays, $N\left(n^*(\Delta T(t))\right)$, obeys the empirical function [35]:

$$N\left(n^*\left(\Delta T(t)\right)\right) = N_{tot}\exp\left(-n^*\left(\Delta T((t))\right)\right) \tag{5.7}$$

with N_{tot} as the total number of pre-existing Shockley partial dislocation arrays of variable height per unit volume. The total number of preexisting SP arrays of variable height can be (over)estimated by approximating the grain volume by D^3 and recognizing that D/c represents the number of dislocations covering a height D.

Hence, $N_{tot} = 2 \cdot (D/c)/D^3 = 2/cD^2$ taking into account that every perfect dislocation by dissociation contributes to the development of two nuclei (see Fig. 5.1). This estimation is rough as at the begin of the transformation the number of SPs in a nucleus is larger than one. However, the values of the fit parameters of the transformation model do not depend strongly on the value of N_{tot} (see section 5.5). The above treatment focussed on the *fcc→hcp* transformation occurring upon cooling. A parallel treatment holds for the *hcp→fcc* transformation occurring upon heating.

5.2.3 Interface-Controlled Growth

When an ordered array of Shockley partial dislocations glides through the crystal (as shown in Fig. 5.1 and Fig. 5.3) the product-phase particle grows. The dimensionality of the growth is one, i.e. the product-phase particle grows in one of the three possible $\langle 11\bar{2} \rangle$ directions oriented perpendicular to the *c*-axis (cf. Fig. 5.2). There is no composition change from parent to product phase in an allotropic phase transformation and thus the growth is controlled by atomic (jump) processes in the direct vicinity of the interface: interface-controlled growth.

The height of a product phase particle which starts to grow at time τ is given by $n^*(\Delta T(\tau)) \cdot c/2$ (cf. Fig. 5.1). Hence, at time t the volume $Y(\tau,t)$ of a product-phase particle, which starts to grow at time τ, is given by (see Fig. 5.1, Eqs. (5.3) and (5.6))

$$Y_i(\tau,t) = D\frac{n^*(\Delta T(\tau))}{2} cr(T(t)) = D\frac{n^*(\Delta T(\tau))}{2} c\int_{\tau}^{t} \nu dt' \tag{5.8}$$

with ν as the interface/Shockley partial dislocation-glide velocity. For small undercooling or overheating the growth velocity ν is given by

$$\nu(T(t)) = M(-\Delta G_m(T(t))) = M_0 \exp\left(-\frac{Q}{RT(t)}\right)(-\Delta G_m(T(t))) \tag{5.9}$$

where M is the temperature dependent interface mobility, M_0 is the pre-exponential factor for growth and Q denotes the activation energy for growth. The net driving force $\Delta G_m(T(t))$ which is given as a molar quantity [21] amounts to (cf. Eqs. (5.1) and (5.5)):

$$\Delta G_m(T(t)) = \frac{\Delta G}{rDn^*(\Delta T(\tau))\frac{c}{2V_m}} = \Delta G_m^{ch}(T(t)) + E_m^{str}(T(t)) + \frac{2\sigma}{n^*(\Delta T(\tau))\frac{c}{2V_m}}. \quad (5.10)$$

5.2.4 Extended Fraction, Transformed Fraction and Impingement

Adopting an appropriate impingement mode the *real* transformed fraction $f_{\text{model}}(T(t))$ can be calculated from the extended transformed fraction x_e (cf. beginning of section 5.2). In the case of anisotropic growth, which pertains to the allotropic phase transformation considered here (one-dimensional growth; cf. section 5.2.3), the (hard) impingement process can be phenomenologically described by the following equation [21]:

$$\frac{df}{dx_e} = (1-f)^{\xi} \quad (5.11)$$

where ξ is a measure for the degree of anisotropic impingement. Integration of Eq. (5.11) for the case $\xi > 1$ yields:

$$f = 1 - [1 + (\xi - 1)x_e]^{-\frac{1}{\xi - 1}}. \quad (5.12)$$

5.3 Experimental

5.3.1 Alloy Production

The cobalt rod with a diameter of 5 mm used in this study was obtained in the hammered, not annealed state from Alfa Aesar (Karlsruhe, Germany) and has a purity of 99.995 at.%. Disc shaped specimens were produced by cutting pieces with a thickness of 750 µm. Both sides of the specimen discs were prepared by grinding with SiC-paper and subsequently polishing using diamond paste down to 0.25 µm such that all specimens have approximately the same mass of about 100 mg. All specimens were cleaned ultrasonically in isopropyl. After the calorimetrical heat treatment the specimen discs were ground and polished again as mentioned above in order to reduce inhomogeneities of the surface as necessary for XRD and LM analysis.

5.3.2 Differential Scanning Calorimetry

The isochronal annealing was carried out with a power-compensated Differential Scanning Calorimeter (DSC) Pyris Diamond by Perkin Elmer. The temperature was calibrated using the melting temperature of zinc (T_m = 692.15 K [37]) measured for each heating rate used. Aluminum was used as pan material for both the specimen and reference container. Specimens of approximately the same mass were used in order to provide similar heat capacities. Pure argon gas with a constant flow was used as protective gas atmosphere. A measurement with empty pans served for determination of the baseline.

For each measurement in the temperature range from 523 K to 893 K at a heating rate varying from 10 to 40 K min^{-1} a new specimen was used. In order to establish a microstructural reference state (see section 5.4), each specimen used for the kinetic analysis, was initially exposed to 60 isochronal transformation cycles with a cooling/heating rate of ±50 K min^{-1} in a temperature range from 523 K to 893 K. The microstructure and phase composition of the specimens in the initial state and after the 1st, 2nd, 3rd, 10th, 20th, 40th and 60th isochronal transformation cycles were analyzed by LM and XRD.

For the calculation of the cumulative enthalpy $\Delta H(T(t))$, as function of temperature (time), the heat signal $d\Delta H(T(t))/dt$ was integrated for cumulative times. Previous to this integration, it is necessary to perform a baseline correction. This was done by subtracting the above mentioned DSC signal recorded with empty pans from the DSC signal recorded with the Co specimen for each heating rate [37]. This implies that the heat capacities of both phases are the same in the temperature region of the transformation, as holds for cobalt. The transformed fraction $f_{exp}(T(t))$ as function of temperature then is given by:

$$f_{\exp}(T(t)) = \frac{\Delta H(T(t))}{\Delta H_{hcp \leftrightarrow fcc}} \tag{5.13}$$

where the total transformation enthalpy $\Delta H_{hcp \leftrightarrow fcc}$ was obtained by integration of the baseline corrected DSC signal over the entire temperature range of the transformation.

5.3.3 X-Ray Diffraction

XRD was employed for phase analysis and to characterize the crystalline imperfection upon thermal cycling. The X-ray diffraction measurements were performed with Mo Kα radiation employing a Bruker D8 Discover diffractometer operating in parallel-beam geometry equipped with an X-ray lens in the incident beam, a parallel-plate collimator in the diffracted beam and an energy-dispersive detector. The 2θ-range of 15° - 45° was measured with a step size of 0.015° and counting time per step of 10s.

5.3.4 Light Microscopy

The surface of the specimen discs before and after the 1^{st}, 2^{nd}, 3^{rd}, 10^{th}, 20^{th}, 40^{th} and 60^{th} transformation cycles and of specimens used for the kinetic analysis were analysed using a Zeiss Axiophot light optical microscope. For that purpose the polished specimen discs were etched for 2 - 7 s using a fresh etching solution (14.3 vol.% H_20, 14.3 vol.% CH_3COOH, 57.1 vol.% HCl and 14.3 vol.% HNO_3).

5.4 Results and Evaluation

A baseline-corrected isochronal DSC-Scan of Co at a heating rate of 20 K min^{-1} showing a heat signal associated with the *hcp→fcc* transformation is presented in Fig. 5.4. T_{onset} denotes the peak onset temperature, T_{peak} is the peak maximum temperature and $\Delta H_{hcp\rightarrow fcc}$ is the enthalpy of transformation (> 0 for the endothermic *hcp→fcc* transformation) given by the (hatched) area enclosed by the DSC signal and the baseline (*dashed*).

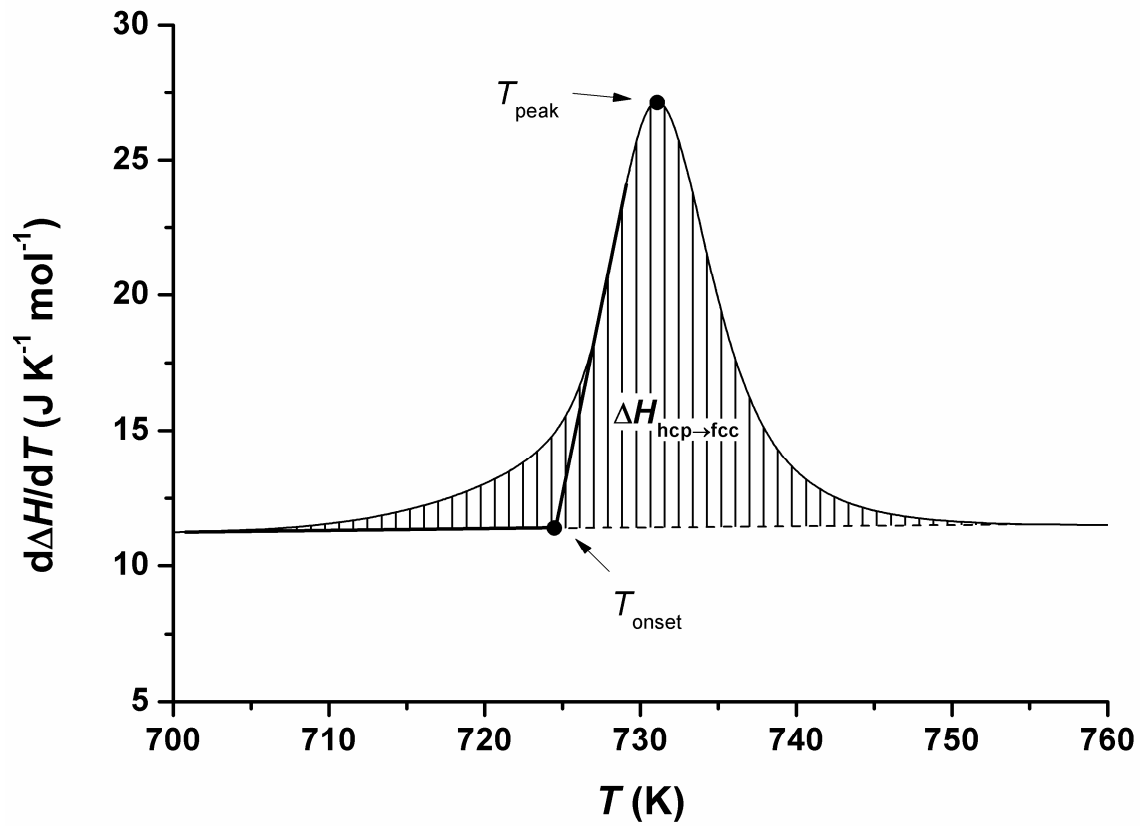

Fig. 5.4: Heat signal corresponding to the endothermic *hcp→fcc* transformation in Co (after 61st cycles) obtained upon isochronal heating at a rate of 20 K min^{-1}

In order to characterize the *hcp→fcc* transformation behaviour and the microstructural evolution upon thermal cycling of initially heavily deformed Co, the change of the DSC heat signal (characterized by the parameters indicated above), XRD diffractograms and the change of the grain size were recorded as a function of the number of transformation cycles experienced (one cycle is *hcp→fcc* followed by *fcc→hcp*). Results are presented in Fig. 5.5.

The variation of the parameters T_{onset}, T_{peak} and $\Delta H_{hcp\rightarrow fcc}$ for the *hcp→fcc* transformation (see Fig. 5.4) is shown in Fig. 5.5a as a function of the number of transformation cycles at a heating rate of 50 K min^{-1} between 523 K and 893 K. Starting from the heavily deformed initial state, the parameters T_{onset}, T_{peak} and $\Delta H_{hcp\rightarrow fcc}$ decrease from the 1st to the 2nd transformation cycle from 736.3 K, 746.9 K and 406 J mol^{-1} to 717.1 K, 735.6 K and 385 J mol^{-1}, followed by an increase between the 2nd and 3rd transformation cycle to 721.9 K, 738.7 K and 452 J mol^{-1}, respectively. After the 3rd transformation cycle T_{onset} and T_{peak} pass through modest local maxima of about 722.3 K and 739.0 K, respectively. Eventually T_{peak} and T_{onset} approach asymptotically equilibrium values of about 735.7±0.2 K (average of the last 40 transformation cycles) and about 726.5±0.2 K (average of the last 20 transformation cycle), respectively.

The total transformation enthalpy, $\Delta H_{hcp\rightarrow fcc}$, shows a steep increase from the 2nd to the 4th transformation cycle and approaches an equilibrium value after about 20 transformation cycles of about 500±3 J mol^{-1} (average of the last 40 transformation cycles). The small values of $\Delta H_{hcp\rightarrow fcc}$ observed in the first cycles suggest that the specimen only experiences a fractional *hcp*→*fcc* transformation during the first cycles.

XRD measurements of Co specimens at room temperature in the initial state and after the 1st, 2nd and 3rd transformation cycles (*inset* in Fig. 5.5b) reveal 111 and 002 reflexes of the *fcc* Co phase after (only) the 1st and 2nd transformation cycle (Cards 89-4308 for *hcp*-Co and 15-0806 for *fcc*-Co of the powder diffraction file [38], were used for phase identification). In the initial state, after the 3rd transformation cycle *and during further cycling* no *fcc* Bragg peaks could be detected. These XRD results support the above interpretation of the $\Delta H_{hcp\rightarrow fcc}$ changes during cycling.

Hence, the amount of *hcp* and *fcc* Co at room temperature after a specific number of transformation cycles can be deduced from the enthalpy data adopting direct proportionality of $\Delta H_{hcp\rightarrow fcc}$ with the amount of *hcp* present before the *hcp*→*fcc* transformation takes place. The thus determined fractional amounts of *hcp* and *fcc* phase at room temperature are shown in Fig. 5.5b as function of the number of transformation cycles. The amount of *fcc* Co at room temperature reaches a maximum of about 25 % after two transformation cycles followed by a decrease towards nil reached at about the 5th transformation cycle.

The full width at half maximum (FWHM) was calculated for the 100, 002, 101, 102 110 and 103 reflexes of *hcp* Co. The FWHM results as obtained for the initial state and after the 1st, 2nd, 3rd, 10th, 20th, 40th and 60th transformation cycles are presented in Fig. 5.5c as function of the corresponding transformation cycle number. For all reflexes a steep decrease can be observed from the values corresponding to the initial state to the values obtained after the 2nd/3rd transformation cycle. This decrease can be ascribed to a reduction of lattice defects in the initially heavily deformed state upon annealing (recovery), grain growth and transformation cycling. For all reflexes the FWHM and thus the defect structure remains about constant after the 3rd transformation cycle.

The change of the mean grain size, *D*, as determined by LM, is shown in Fig. 5.5d as function of the number of transformation cycles. It was not possible to measure the grain size of Co in the initial stage because the etched microstructure did not allow a clear identification of grain boundaries: the highly deformed initial state leads to an uncontrollable etching process. The grain size increases upon thermal cycling from initially less than 10 µm to about 87±5 µm after the 40th cycle and remains constant thereafter.

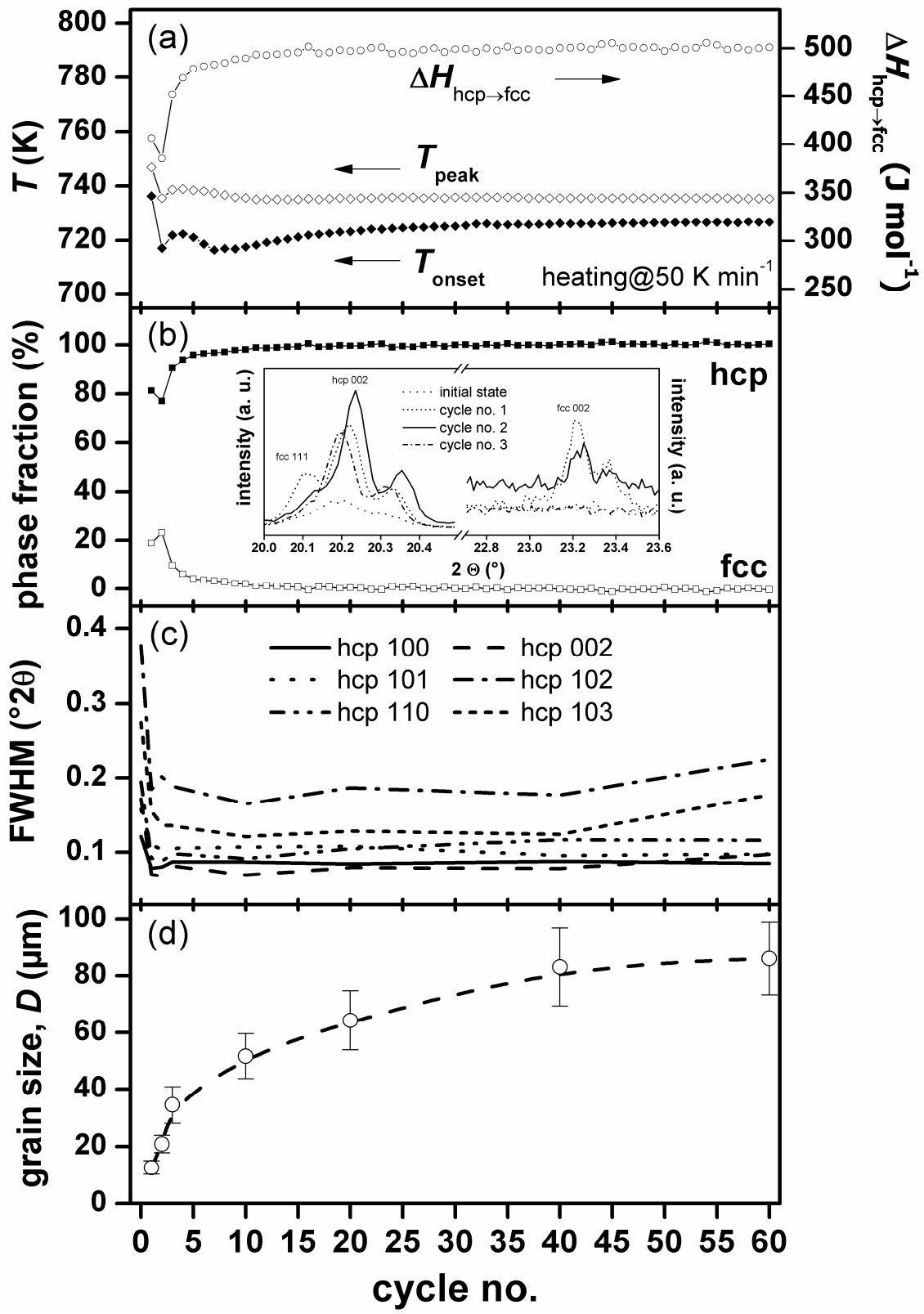

Fig. 5.5: Results of DSC, XRD and LM analysis as function of the number of transformation cycles. (a) T_{onset}, T_{peak} and $\Delta H_{hcp\rightarrow fcc}$ at a heating rate of 50 K min^{-1}, (b) phase fraction as deduced from the enthalpy data in (a) (see text); *inset*: 111 and 002 reflexes of *fcc* phase and 002 reflexes of *hcp* phase before and after the 1st, 2nd and 3rd cycles, (c) FWHM of selected XRD reflexes as indicated and (d) grain size.

It has been concluded from the above results that, to assure the same initial state for each experiment used for kinetic analysis, each such specimen will be subjected to 60 transformation cycles before a kinetic analysis is performed.

Important morphological characteristics are revealed by LM from the specimen surfaces, as shown for the 10^{th}, 40^{th} and 60^{th} transformation cycles in Fig. 5.6a-c. After the 10^{th} cycle (Fig. 5.6a) the etching suggests an underlying transformation structure exhibiting different, specific orientations of martensite plates within a Co grain. After the 40^{th} cycle (Fig. 5.6b) the etching suggests that only a single specific orientation is associated with the martensitic transformation experienced by a grain. After the 60^{th} transformation cycle no such etch effect is observed (cf. Fig. 5.10 and its discussion in section 5.6.1).

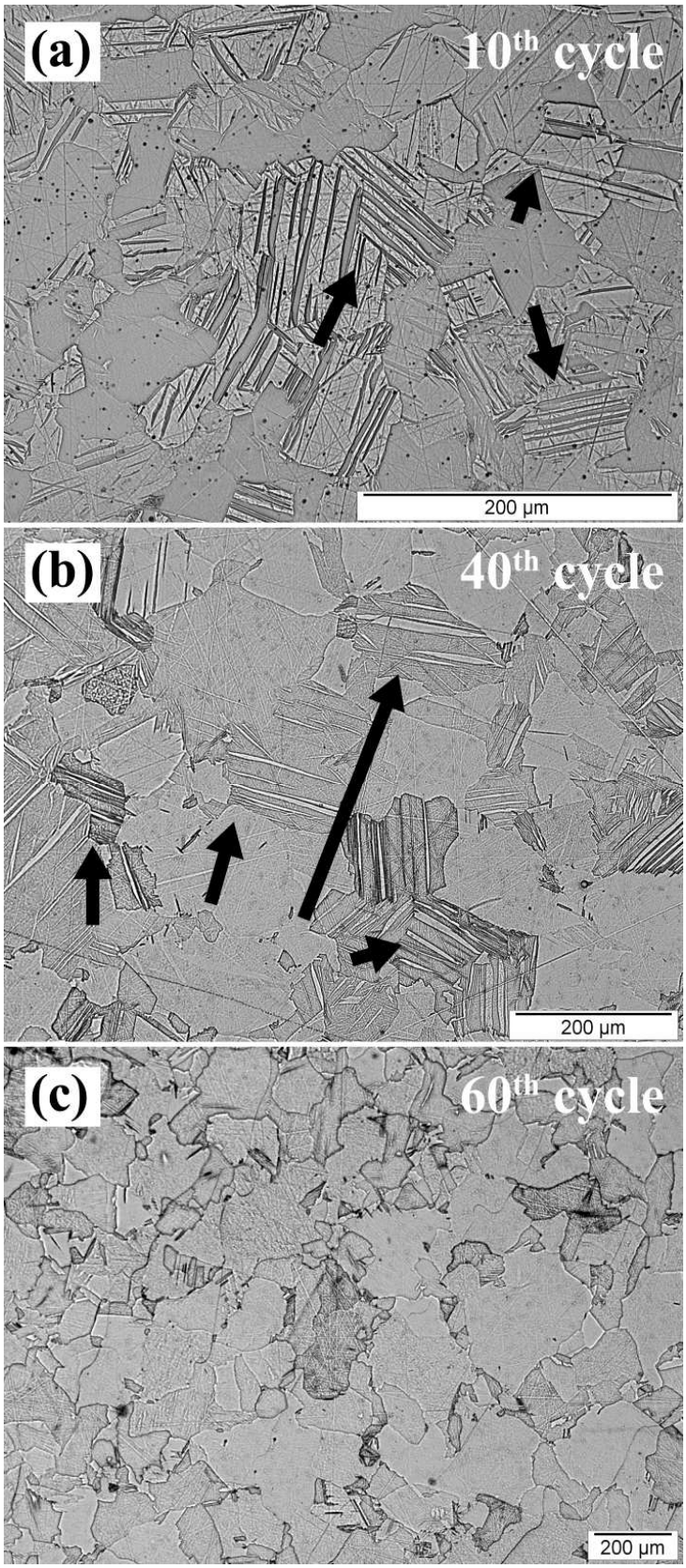

Fig. 5.6: Light optical micrographs of the etched microstructure of the surface of Co specimens after the (a) 10^{th}, (b) 40^{th} and (c) 60^{th} transformation cycle performed in the DSC at a rate of ± 50 K min^{-1} in the temperature range from 523 K to 893 K. The etched microstructure suggests (see the arrows) that upon prolonged annealing the number of types of glide planes operating during the martensitic transformation (the *fcc→hcp* experienced in the cooling part of the transformation cycle) in a single grain is reduced to one (see text and section 5.6.1).

5.5 Analysis of the Transformation Kinetics

Baseline corrected isochronal DSC scans for the allotropic *hcp→fcc* (upon heating) and *fcc→hcp* (upon cooling) transformations in Co measured at heating/cooling rates in the range from 10 to 40 K min^{-1} are presented in Fig. 5.7. The enthalpy of transformation for the *hcp→fcc* transformation (upon heating; independent of heating rate) is about +501±7 J mol^{-1} and for the *fcc→hcp* transformation (upon cooling; independent of cooling rate) about -512±13 J mol^{-1}, i. e. within the experimental accuracy the *hcp→fcc* and *fcc→hcp* transformations exhibit the same absolute value for the enthalpy of transformation.

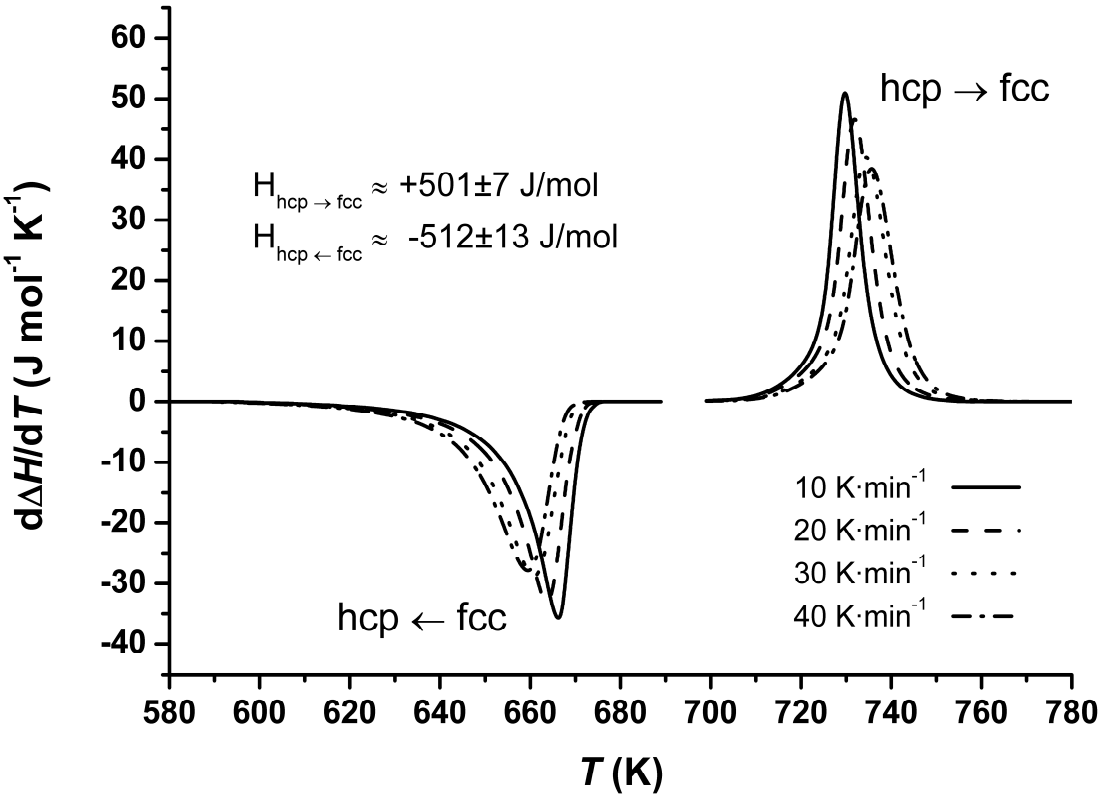

Fig. 5.7: Isochronal baseline corrected DSC-scans for Co (after 60 transformation cycles) at various heating rates as indicated.

The cooling curves in Fig. 5.7, i. e. for the *fcc→hcp* transformation, have been included for the sake of completeness. Whereas the start temperature for the *fcc→hcp* transformation (upon cooling) clearly depends on the cooling rate applied, this is much less the case (if at all) for the dependence of the start temperature of the *hcp→fcc* transformation (upon heating) on heating rate (see Fig. 5.7). In both cases, i. e. for the transformation upon cooling and the transformation upon heating, a cooling/heating rate independent start temperature is expected in view of the athermal value of the nucleation process (see section 5.2.2). It must be noted, that no temperature calibration of the DSC for the cooling part of the cycle is possible and that the DSC signal during cooling is smeared distinctly, as is well known for power-compensated DSCs [37]. Therefore, the cooling-rate dependence of the start temperature of the transformation upon cooling has to be considered as an artifact from the measurement and the cooling curves cannot be used for kinetic analysis.

The kinetic analysis of the allotropic *hcp→fcc* transformation of Co was performed applying the modular phase transformation model in the form as described in section 5.2.

The experimental transformation rates df_{exp}/dT ($df_{\mathrm{exp}}/dT = 1/\Phi\, df_{\mathrm{exp}}/dt$) have been plotted in Fig. 5.8 as function of the transformed fraction $f_{\mathrm{exp}}(T(t))$ for the different heating rates. The corresponding curves for the experimentally determined transformed fractions $f_{\mathrm{exp}}(T(t))$ (see section 5.3.2, Eq. (5.13)) are shown in Fig. 5.9 as function of temperature $T(t)$. Evidently, the maximum transformation rate occurs at $f_{\mathrm{exp}} < 1 - 1/e$. This is a strong indication for anisotropic growth [39] as expected for the *hcp↔fcc* transformation in Co (cf. sections 5.2.2and 5.2.3). The impingement mode for anisotropic growth (introduced in section 5.2.4) has thus been used in the kinetic model of the phase transformation.

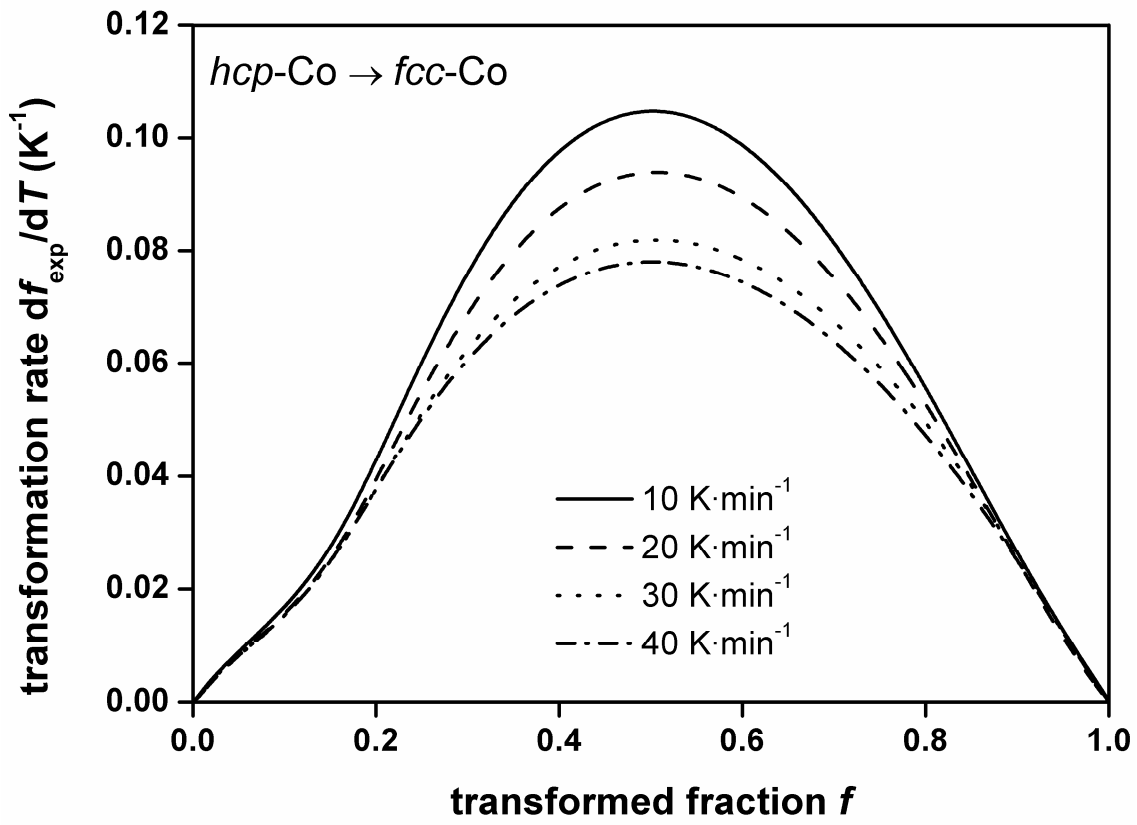

Fig. 5.8: The experimental transformation rate df_{exp}/dT as function of the transformed fraction for the *hcp→fcc* transformation for various heating rates. The plots show maxima at positions left with respect to the position $f = 1 - 1/e$, indicating an anisotropic impingement mode [39].

The kinetic model parameters σ, Q and ξ were determined by numerically fitting of the model to *simultaneously* all isochronal heating runs obtained for various heating rates in the range from 10 K min^{-1} to 40 K min^{-1}. The mean square error (*MSE*) between the calculated (*calc*) and experimental (*exp*) transformed fraction curves was minimized by varying the fit parameters using a multidimensional unconstrained nonlinear minimization fitting routine [40] as implemented in MATLAB for each *i*th of the applied heating rates

$$MSE = \sum_{i=1}^{N} \left(\frac{exp - calc}{exp} \right)^2 . \tag{5.14}$$

The results of the fitting as described above are shown in Fig. 5.9 (experimental data: *symbols*; fit: *lines*) and Table 5.1 (i. e. the values thus determined for σ, Q and ξ).

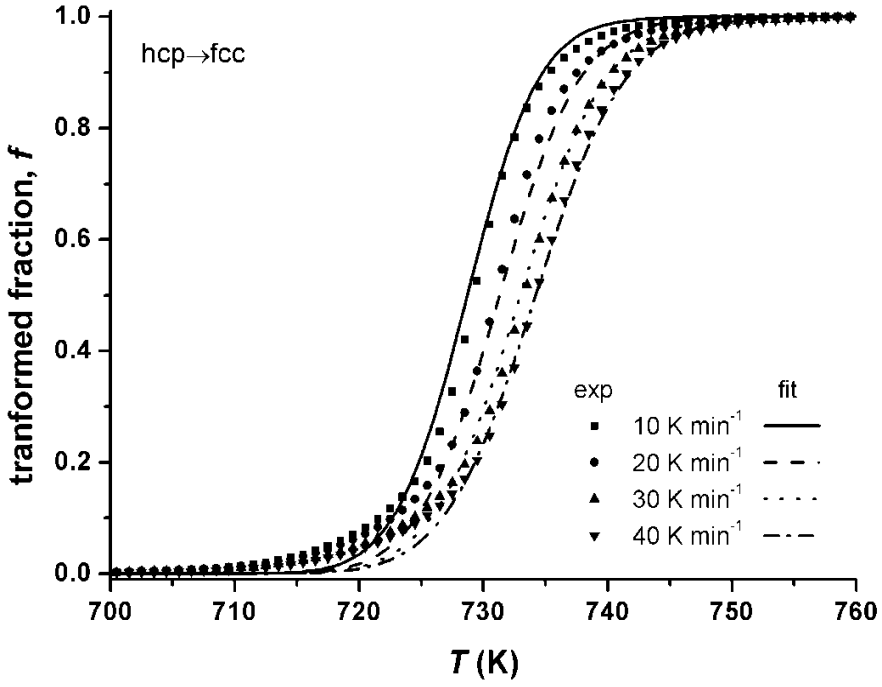

Fig. 5.9: Isochronal DSC curves (symbols) and model fit (simultaneously to all runs) using the modular phase transformation model (σ, Q and ξ as fit parameters) for the allotropic phase transformation *hcp→fcc* of Co.

Values used for the constants in the model have (also) been given in Table 5.1. The total number of pre-existing dislocations N_{tot} within a grain of mean size D = 87±5 µm was calculated as described in section 5.2.2 as $6.5 \cdot 10^{17}$ m^{-3}. The total enthalpy of transformation was taken as $\Delta H_{hcp \rightarrow fcc}$ = 501±7 J mol^{-1}, as determined experimentally (cf. section 5.4). The strain energy contribution expressed as E_m^{str}, corresponding with the macroscopic distortion discussed in sections 5.2.1 and 5.2.2, was estimated according to [19] at about 0.838 J mol^{-1} under the assumption of linear elasticity and coherency (full elastic accommodation of volume misfit).

It is supposed that dislocation glide is rate controlled by thermal activation as it generally holds for materials with metallic bonding type. In pure metals it is assumed that the atomic structure within the closest packed glide plane represents a weak lattice resistance. The mobility of these dislocations is thus determined by thermal fluctuations characterized by an activation energy Q [41].

The temperature-independent dislocation/interface velocity v_0 was estimated by using the well-known (empirical) expression for the pre-exponential factor for lattice-resistance controlled glide of dislocations in metals (i. e. rate limited by weak discrete obstacles) (as validated for a wide range of metals [42]), which reads $\dot{\gamma}_0 = v_0 \rho_m b = 10^6\, s^{-1}$ with ρ_m as the dislocation density and b as the Burgers vector taken equal to $1/2 \cdot \sqrt{2} \cdot a_{fcc}$ with a_{fcc} = 0.35447 nm [34]. The density of mobile dislocations can be estimated according to [42] as 10^{13} m^{-2} lying in the range of values expected for *fcc* and *hcp* metals. The thus obtained value for v_0 is about 400 m s^{-1}. Thus the mobility $M_0 = v_0 / RT$ [21] was assessed at 4.3 m·mol·J^{-1}·min^{-1}, adopting a mean value for the temperature T = 700 K. Note that the temperature dependence of M_0 is small in comparison to the temperature dependence of the exponential term in M (see Eq. (5.9)) and thus the temperature dependence of M_0 can be neglected.

Table 5.1: Overview of the constants used in the adopted modular phase transformation model (see section 5.2), as well as the values obtained for the fit parameters by fitting this model to, simultaneously, all isochronal DSC scans upon heating.

	parameter	value	source
constants	enthalpy, $\Delta H_{hcp \rightarrow fcc}$	501±7 J mol^{-1}	experiment; this work
	grain size, D	87 µm	experiment; this work
	lattice parameter, c	0.40686 nm	[34]
	equilibrium temperature, T_0	690±7 K	[4]
	total number of pre-existing dislocations, N_{tot}	$6.5 \cdot 10^{17}$ m^{-3}	$N_{tot} = 2/cD^2$; this work
	strain energy, E_{Str}	0.838 J mol^{-1}	according to [19]
	mobility, M_0	4.3 m mol J^{-1} min^{-1}	$M_0 = v_0 / RT$ v_0 estimated from [42]; this work
***fit* parameters**	interface energy, σ	6.8±0.4 mJ m^{-2}	-
	activation energy for growth, Q	33±15 kJ mol^{-1}	-
	impingement parameter, ξ	1.35 -	-

The influence of a variation of the constant parameters N_{tot}, T_0 and M_0 on the fit parameters, as indicated by $N_{tot} = 6.5 \cdot 10^{17\pm1}$ m^{-3}, T_0 = 690±1 K and $M_0 = 4.3 \cdot 10^{0\pm1}$ m mol J^{-1} min^{-1}, yielded variations of σ and Q as indicated in Table 5.1; the impingement parameter ξ is not influenced.

5.6 Discussion

5.6.1 Preceding transformation cycles

Each Co specimen used for kinetic analysis was subjected to a number of 60 preceding transformation cycles to assure similar starting conditions (same microstructure) and full transformation (see section 5.4). The phenomenon can be interpreted as that the preceding transformation cycles are needed to stabilize the dislocation configuration (cf. section 5.2.1) in the specimen that carries the forward (*hcp→fcc*) and backward (*fcc→hcp*) transformations.

The initially incomplete transformation can partly be ascribed to the relatively strong interaction of the (partial) dislocations with the grain boundaries: upon increasing grain size during cycling (see Fig. 5.5d) relatively more dislocations become available for establishing the transformation [1, 2, 10].

During the first transformation cycles the transformations occur in conjunction with recovery, possible (local) recrystallisation and grain growth in order to reduce the stored plastic deformation and grain-boundary surface. This leads to changes of the (initially disarranged) dislocation structure. A further complication is that after a first *hcp→fcc* transformation upon heating, that then, upon subsequent cooling, a completely reverse formation of *hcp* Co requires glide of SPs on the closest packed $\{111\}_{fcc}$ planes lying parallel to the previous $\{0001\}_{hcp}$ planes. However, at least initially SPs may be available as well on $\{111\}_{fcc}$ planes not parallel to the former $\{0001\}_{hcp}$ plane and thus the original *hcp* grain microstructure is not re-established (Note the variously orientated *hcp* Co martensite “plates” in a single grain in Fig. 5.6a). As a consequence, this reasoning provides a further reason (see above) why the transformation cannot run to completion in such a grain; a small amount of parent phase is retained (see Fig. 5.5b and its inset).

The above described transformation behaviour for the first transformation cycles is compatible with the DSC results. The decrease of T_{onset} and T_{peak} found for the 2nd transformation cycle can be understood such that during the first complete *hcp↔fcc* cycle the disordered dislocation structure of the initial state evolves into a more ordered (in the sense of the discussion in section 5.2.1) dislocation structure, thereby facilitating the transformation: less overheating is required (see section 5.2.2).

Prolonged thermal cycling leads to an increase of the thickness of the martensite “plates” (Fig. 5.6b), i. e. the height of the operating dislocation array increases, and a single glide variant appears to become dominant (cf. Fig. 5.6b and c) [6, 10].

The above discussion leads to a summarizing schematic presentation of the evolving dislocation structure in a grain during *hcp*↔*fcc* (thermal) cycling as presented in Fig. 5.10.

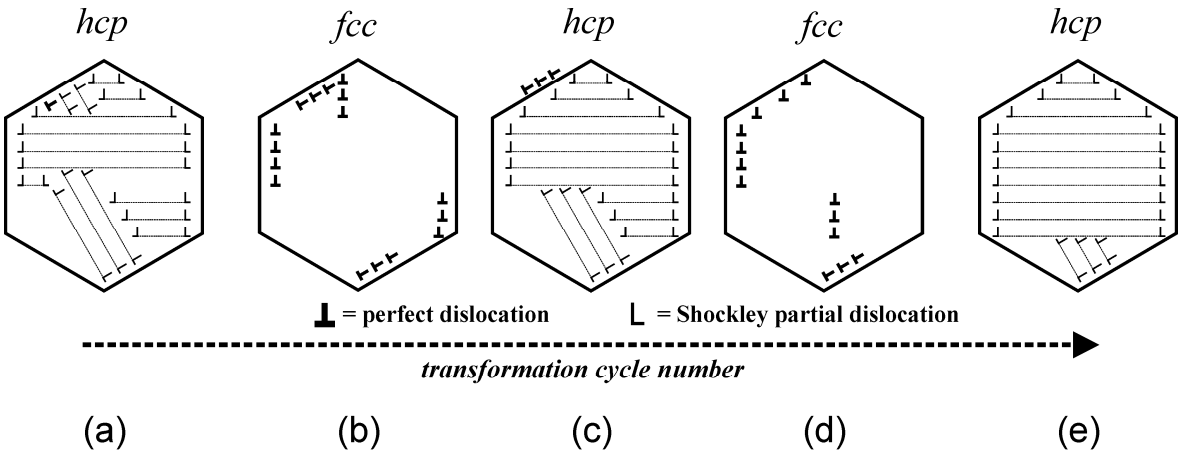

Fig. 5.10: Schematic presentation of the dislocation structure development in Co upon *hcp*↔*fcc* (thermal) cycling.
(a) The initial state represents (severely deformed) *hcp* Co as formed by dissociation of arrays of perfect dislocations and subsequent "ordered" glide of SPs on every second closest packed {111} plane in the parent *fcc* Co. The whole grain could not transform to *hcp* Co because of blocking of the growing martensite "plates" growing by "ordered" glide of arrays of SPs; each stack of SPs glides along one of the four equivalent types of $\{111\}_{fcc}$ planes.
(b) + (c) Upon continued thermal cycling the height of the (remaining, active) stacks of arrays of (partial) dislocations (perpendicular to $\{0001\}_{hcp}/\{111\}_{fcc}$ planes) increases, due to pick up of neighbouring dislocations, pushing aside unfavourably oriented smaller dislocation stacks, e. g. by limiting the associated SP glide, and by even driving them back (in associated form) into the grain boundaries (as illustrated in the figure; cf. (a) and (c)).
(d) + (e) Eventually, upon prolonged thermal cycling, a dislocation structure emerges that realizes the *hcp*↔*fcc* transformation on the basis of (ideally) one single stack of ordered perfect dislocations (in *fcc*) = 2 parallel stacks of ordered Shockley partial dislocations (in *hcp*) implying that only one (instead of, maximally, four; see (a) + (b)) glide plane system operates within a single grain, e. g. $(111)_{fcc} \parallel (0001)_{hcp}$, $[\bar{1}10]_{fcc} \parallel [\bar{1}0\bar{1}0]_{hcp}$.

5.6.2 Kinetics

The evaluation of the kinetics of the allotropic *hcp*→*fcc* phase transformation in Co performed in section 5.5 demonstrates that this transformation can be well described as governed by the activation of pre-existing nuclei (stacked dislocation sequences) and thermally activated interface-controlled growth subjected to anisotropic impingement. The resulting values for the fit parameters σ, Q and ξ agree well with data provided by theory and experiment (see what follows).

The investigation of dislocation nodes (the extension of a dislocation node depends amongst others on the stacking fault energy produced by the node) in pure Co [8] and Fe-Cr-Ni alloys [43] yielded stacking-fault energy values from 5 to 10 mJ m^{-2}. This agrees very well with the here determined value for the interface (= stacking fault) energy resulting from model fitting of the transformation kinetics yielding $\sigma = 6.7 \pm 0.4$ mJ m^{-2}.

The ratio of the activation energy for diffusion and the activation energy for dislocation glide controlled by lattice resistance is for metals about 7 [42]. The activation energy for self diffusion of Co is $Q_{Co} = 270$ kJ mol^{-1} [2]. Indeed, $1/7 \cdot Q_{Co} \approx 38$ kJ mol^{-1} which is well compatible with the here determined value of the activation energy for growth, $Q = 33 \pm 15$ kJ mol^{-1}, thereby validating the applied concept of growth controlled by dislocation glide.

5.7 Conclusions

- Extensive thermal cycling of Co in a fixed temperature range is necessary to establish full reversibility of the allotropic *hcp*↔*fcc* phase transformation (i. e. reaching constant values of T_{onset}, T_{peak} and $\Delta H_{hcp \rightarrow fcc}$). During thermal cycling stabilization of the dislocation structure is established such that in a single grain the *hcp*↔*fcc* transformation is established by (ideally) only one single stack of ordered perfect dislocations (in *fcc*) = 2 parallel stacks of ordered Shockley partial dislocations (in *hcp*), implying that only one (of the maximally four) glide-plane types operates within a single grain.

- The kinetics of the transformation can be well described on the basis of a modular transformation model adopting an athermal nucleation mode and an anisotropic interface-controlled growth mode.

- Results obtained for the fit parameters σ (= 6.7±0.4 mJ m^{-2}) and Q (= 33±15 kJ mol^{-1}) are well compatible with the interpretation of the product/parent interface as a stacking fault and of the growth process as realized by thermally activated glide of Shockley partial dislocations.

References

[1] F. Sebilleau and H. Bibring, In: *The Mechanism of Phase Transformation in Metals*, Edited, London, Institute of Metals, **18** (1955) 209.
[2] Cobalt Monograph, *Centre d'Information du Cobalt*. Brussels (1960).
[3] O. S. Edwards and H. Lipson, *J Inst Met* **69** (1943) 177.
[4] J. B. Hess, and C. S. Barrett, *J Met* **4** (1952) 645.
[5] E. A. Owen and D. Madoc Jones, *Proc Phys Soc London Sec B* **67** (1954) 456.
[6] E. Votava, *J Inst Met* **90** (1961) 129.
[7] J. O. Nelson and C. J. Altstetter, *Trans Metall Soc AIME* **230** (1964) 1577.
[8] T. Ericsson, *Acta Metall* **14** (1966) 853.
[9] R. Hultgren, P. D. Desai, and D. T. Hawkins, *Selected Values of the Thermodynamic Properties of the Elements*. American Society of Metals, Ohio (1973).
[10] A. Munier et al., *J Mat Res* **5** (1990) 769.
[11] O. H. Knacke, *Thermochemical Properties of Inorganic Substances*. Springer, Berlin, Heidelberg (1991).
[12] J. Y. Huang, Y. K. Wu, and H. Q. Ye, *Acta Metall* **44** (1996) 1201.
[13] T. Waitz and H. P. Karnthaler, *Acta Mater* **45** (1997) 837.
[14] O. Blaschko, *Mat Sci Eng* **A127** (1990) 257.
[15] Z. H. Kuang et al., *Scr Mater* **42** (2000) 795.
[16] H. T. Hesemann, P. Müllner, and E. Arzt, *Scr Mater* **44** (2001) 25.
[17] H. T. Hesemann et al., *J Phys IV* **112** (2003) 107.
[18] A. T. Dinsdale, *Calphad* **15** (1991) 317.
[19] G. B. Olson, and M. Cohen, *Metall Trans* **7A** (1976) 1897.
[20] E. J. Mittemeijer, and F. Sommer, *Z Metallkd* **93** (2002) 352.
[21] F. Liu et al., *Int Mat Rev* **52** (2007) 193.
[22] W. Baumann, A. Leineweber, and E. J. Mittemeijer (2010), as submitted for publication
[23] A. T. W. Kempen, F. Sommer, and E. J. Mittemeijer, *J Mat Sci* **37** (2002) 1321.
[24] A. T. W. Kempen, F. Sommer, and E. J. Mittemeijer, *Acta Metall Mater* **50** (2002) 1319.
[25] A. T. W. Kempen et al., *Metall Mater Trans* **33A** (2002) 1041.
[26] H. Nitsche, F. Sommer, and E. J. Mittemeijer, *Metall Mater Trans* **37A** (2006) 621.
[27] H. Nitsche et al., *Z Metallkd* **96** (2005) 1341.
[28] H. Nitsche, F. Sommer, and E. J. Mittemeijer, *J Non-Cryst Solids* **351** (2005) 3760.
[29] F. Liu, F. Sommer, and E. J. Mittemeijer, *Acta Mater* **52** (2004) 3207.
[30] A. T. W. Kempen, F. Sommer, and E. J. Mittemeijer, *Acta Mater* **50** (2002) 3545.
[31] Y. C. Liu, F. Sommer, and E. J. Mittemeijer, *Acta Mater* **51** (2003) 507.
[32] Y. C. Liu, F. Sommer, and E. J. Mittemeijer, *Acta Mater* **54** (2006) 3383.
[33] A. H. Cottrell, *The Mechanical Properties of Matter* (Chapter 3) John Wiley & Sons, Inc., New York (1964)
[34] P. Villars and L. D. Calvert. *Pearson's Handbook of Crystallographic Data for Intermetallic Phases 1*, ASM International, Materials Park, Ohio, (1997).
[35] M. Lin, G. B. Olson, and M. Cohen, *Metall Trans* A **23** (1992) 2987.

[36] E.-S. Lee and Y. G. Kimm, *Acta Metall Mater* **38** (1990) 1677.
[37] G. W. H. Höhne, W. F. Hemminger, and H.-J. Flammersheim, *Differential Scanning Calorimetry*. Second Edition. Berlin Heidelberg , Springer-Verlag, (2003)
[38] International Centre of Diffraction Data. Newton Square, PA, USA (1997-2007)
[39] F. Liu et al., *Acta Metall Mater* **57** (2009) 6176.
[40] J. A. Nelder and R. Mead, *Comput J* **7** (1965) 308.
[41] J. E. Dorn, *Mechanical Behavior of Materials at elevated Temperatures* (Chapter 5), McGraw-Hill Book Company, Inc., New York (1961)
[42] J. F. Frost and M. F. Ashby, *Deformation-Mechanism Maps* [..], Oxford, Pergamon Press (1982)
[43] F. Lecroisey and A. Pineau, *Metall Trans* **3** (1972) 387.

6 Summary

6.1 Natural Formation of *bcc* Co in the Initial Stage of Co Precipitation in Supersaturated $Au_{90}Co_{10}$ Alloy

In *chapter 2* of this thesis the initial precipitation of Co from supersaturated Au - 10.12 at. % Co is investigated. The microstructural evolution upon isochronal annealing with differential scanning calorimetry (DSC) at a heating rate of 20 K min^{-1} was investigated by (high resolution) transmission electron microscopy [(HR)TEM]. The natural formation of, according to bulk thermodynamics, metastable *bcc* Co, with a platelike morphology and a Bain-type orientation relationship with the Au-rich matrix, is observed (Fig. 6.1).

The metastable *bcc* modification happens because the high initial interface-to-volume ratio promotes the development of precipitates of low interface energy (as holds for the *bcc* Co precipitates coherent with the Au-rich matrix). Upon continued annealing growth/coarsening of the precipitate particles takes place. Then, by a Bain transformation of metastable *bcc* Co, the *fcc* Co modification can be formed which then exhibits a cube on cube orientation relationship with the Au rich matrix. The low interface-to-volume ratio for the precipitate phase in an advanced stage of annealing makes possible an overcompensation of an unfavorable interfacial energy (incoherent vs. coherent interface) by a more favorable chemical bulk energy (*fcc* vs. *bcc* modification).

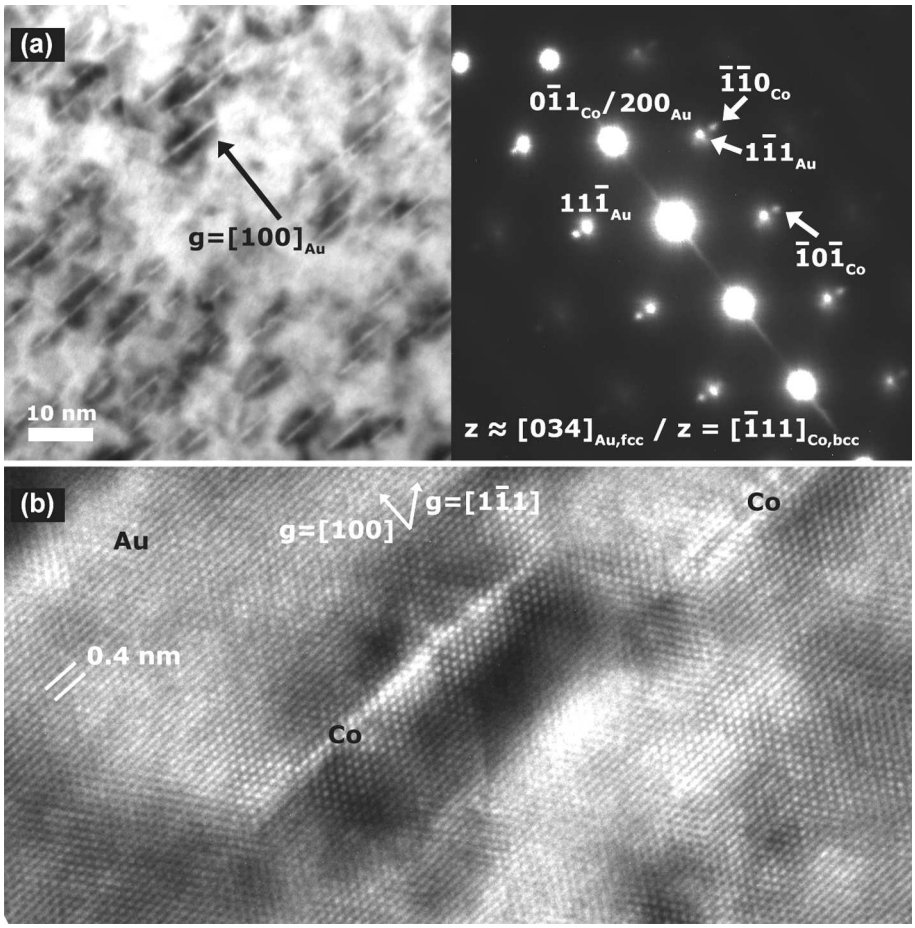

Fig. 6.1: TEM bright field and HRTEM images of $Au_{90}Co_{10}$ after isochronal annealing to 633 K with 20 K min^{-1}. (a) extra spots due to the *bcc* crystal structure of the Co precipitate plates near the {111} Au-matrix spots (see arrows in the SADP) are compatible with a [-111] zone axis for the *bcc* Co precipitates. (b) HRTEM image: [011] zone axis of Au-rich matrix; Co has precipitated as very thin coherent plates about 0.5 to 1 nm thick and 5 to 10 nm in width.

6.2 Precipitation of Co from Supersaturated $Au_{90}Co_{10}$: Morphology and Kinetics

In *chapter 3* of this thesis the kinetics of precipitation reaction of Co from initially supersaturated Au – 10.12 at. % Co and the corresponding morphology of these precipitates are investigated. Specimens of quenched supersaturated Au-Co alloy were exposed to isothermal and isochronal annealings applying differential scanning calorimetry (DSC) in order to force the precipitation of Co and to trace the corresponding heat release which is used for kinetic analysis. The microstructure, phase composition and mechanical properties are investigated by (high resolution) electron transmission microscopy [(HR)TEM], X-ray diffractometry (XRD) and hardness measurements.

Platelike coherent *bcc* Co nanoparticles (width $\approx 0.5 - 1$ nm, length ≈ 5 - 10 nm) develop in the initial stage of precipitation from quenched supersaturated Au - 10.12 at. % Co, in the bulk of the grains, exhibiting a Bain-type orientation relationship [$(100)_{Au,fcc}//(100)_{Co,bcc}$ and $[001]_{Au,fcc}//[011]_{Co,bcc}$ (three variants)], upon both isothermal annealing and isochronal annealing. Prolonged annealing leads to a transition from coherent *bcc* Co to incoherent *fcc* Co precipitates epitaxially orientated to the *fcc* Au matrix [$(100)_{Au,fcc}//(100)_{Co,fcc}$ and $[001]_{Au,fcc}//[001]_{Co,fcc}$ (three variants)]. This *bcc*-to-*fcc* transition is associated with a minor heat effect represented by a shoulder at the DSC peak. During further isochronal annealing an equiaxial morphology develops for the precipitated particles.

A minor amount of discontinuous precipitation (DP) occurs in small regions adjacent to grain boundaries (< 0.5 vol. %). The DP is halted in an early stage due to the continuous nucleation accompanied with blocking of the migrating DP reaction front and decreasing driving force for DP due to a decreasing supersaturation upon prolonged precipitation.

The nucleation and growth modes for the precipitation of the coherent *bcc* Co particles could be determined by fitting of a modular phase transformation model simultaneously to all isothermal DSC runs and simultaneously to all isochronal DSC runs. In case of isothermal annealing (Fig. 6.2a) the kinetics of the precipitation is governed by site saturation (pre existing nuclei at $t = 0$) in combination with interface controlled growth. The effective activation energy of the transformation is given solely by the activation energy for growth which equals about 60 kJ mol^{-1} and is ascribed to the enthalpy of vacancy migration. In case of isochronal annealing (Fig. 6.2b) the kinetics of the precipitation is governed by continuous nucleation in combination with interface controlled growth. The effective activation energy equals about 100 kJ mol^{-1}, which is generally given by a weighted sum of the activation energy for growth and the activation energy for nucleation. In the present case the activation energy for nucleation and growth may be about equal, implying that their values are about 100 kJ mol^{-1}.

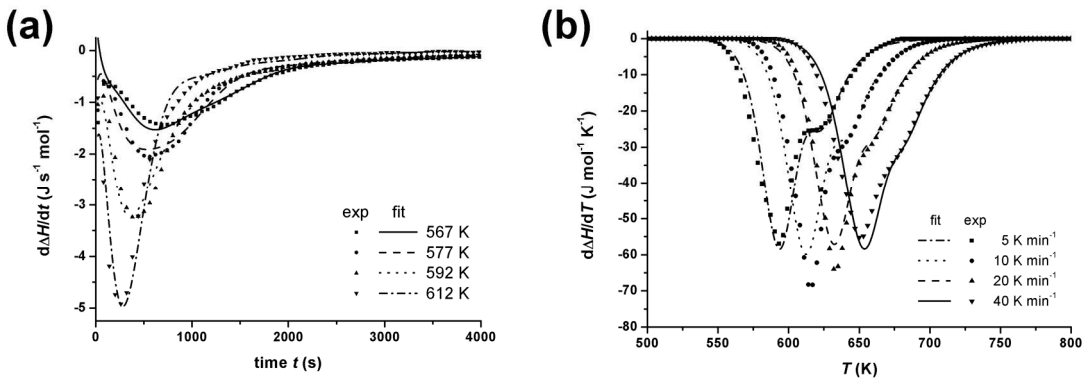

Fig. 6.2: (a) Isothermal and (b) isochronal DSC curves (symbols) and results of the fitting (solid lines) of the modular phase transformation model to simultaneously all isothermal and simultaneously all isochronal DSC scans, respectively.

The differences in nucleation modes for the isothermal and isochronal anneals is a direct consequence of quenched in defects as vacancies and dislocations during quenching and the difference in the extent of recovery before the onset of precipitation. Whereas in case of isothermal annealing most of the quenched in lattice defects are present at the onset of precipitation, in case of isochronal annealing a partial recovery takes place prior to the begin of precipitation. As a consequence a smaller amount of excess vacancies and dislocations operates during precipitation in the isochronal anneals. This implies, as compared to the isothermal annealing, a different nucleation mode (site saturation → continuous nucleation) and a larger activation energy for growth (larger then the enthalpy of migration of vacancies).

6.3 Kinetics of the Precipitation of Co from Supersaturated Cu Co Alloy

In *chapter 4* of this thesis the kinetics of the precipitation of Co from initially supersaturated Cu – 0.95 at. % Co upon isochronal annealing applying differential scanning calorimetry (DSC) is investigated (Fig. 6.3). The microstructure is analysed by (high resolution) transmission electron microscopy [(HR)TEM] (Fig. 6.4).

The precipitation of *fcc* Co from supersaturated Cu – 0.95 at. % Co is governed by continuous, random nucleation and diffusion controlled, isotropic growth, as described by the modular phase transformation model.

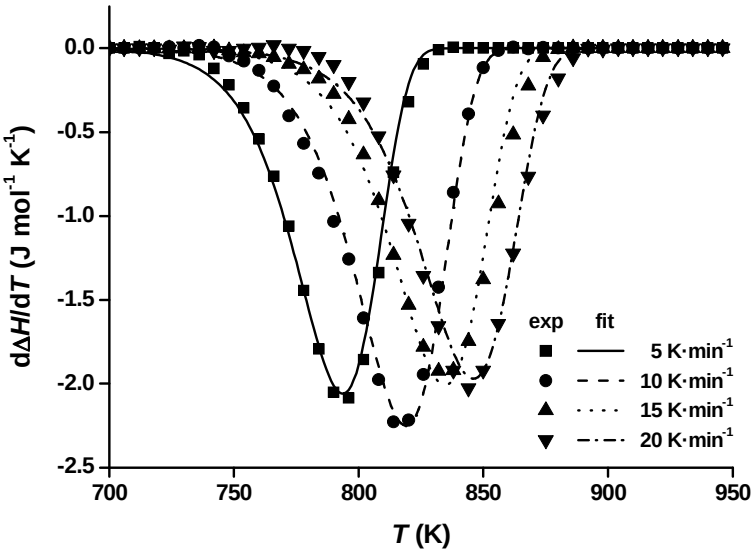

Fig. 6.3: Isochronal DSC curves (symbols) and model fit (simultaneously to all runs) using the modular phase transformation model for the precipitation of Co from supersaturated Cu - 0.95 at. % Co.

Fitting of the kinetic model to transformation rate data (Fig. 6.4), as exhibited by DSC scans, subject to additional constraints as for example provided by microscopic (TEM) analysis, allows determination of the kinetic parameters characterizing the separate nucleation and growth modes.

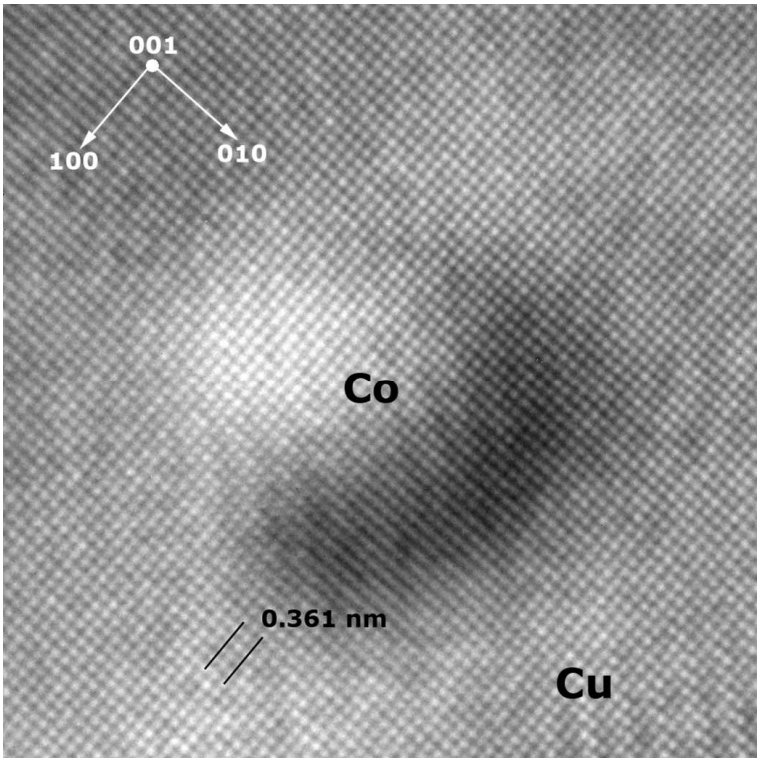

Fig. 6.4: HRTEM image of Cu – 2 at. % Co annealed at 843 K for 60 min ([001] zone axis). The image shows a spherical Co-rich particle fully coherent with the surrounding Cu-rich matrix. The precipitate particle has a *fcc* crystal structure, as well as the matrix.

The effective, overall activation energy of about 133±8 kJ mol^{-1} can (thus) be separated into separate activation energies of nucleation and growth of 50 kJ mol^{-1} and 177 kJ mol^{-1} respectively. Nucleation is found to come to a halt long before all Co dissolved in the Cu rich matrix has precipitated. Continued precipitation can only be realized by growth accompanied with simultaneous coarsening. The activation energy of growth is distinctly smaller than the activation energy for the diffusion of Co in equilibrated Au due to the presence of quenched in excess vacancies.

6.4 Kinetics of the Allotropic *hcp→fcc* Phase Transformation in Cobalt

In the last, fifth chapter of this thesis the allotropic phase transformation in Co from the low temperature *hcp* crystal structure into the high temperature *fcc* crystal structure was investigated by differential scanning calorimetry (DSC) upon isochronal annealing at heating rates in the range from 10 to 40 K min^{-1}. Preceding to the kinetic analysis of the martensitic *hcp→fcc* phase transformation isochronal thermal cycling was applied to all Co specimens using DSC at a heating rate of 50 K min^{-1} in order to equalize the microstructure.

From the analysis of XRD measurements and characterizing DSC parameters as the enthalpy, peak onset and peak maximum temperature which were deduced from the thermal cycling treatments, the microstructure evolution can be understood (Fig. 6.5). In each single Co grain of the poly crystalline specimens a preferred glide plane, e. g. $(0001)_{hcp}||(111)_{fcc}$, evolves leading to an orientated transformation.

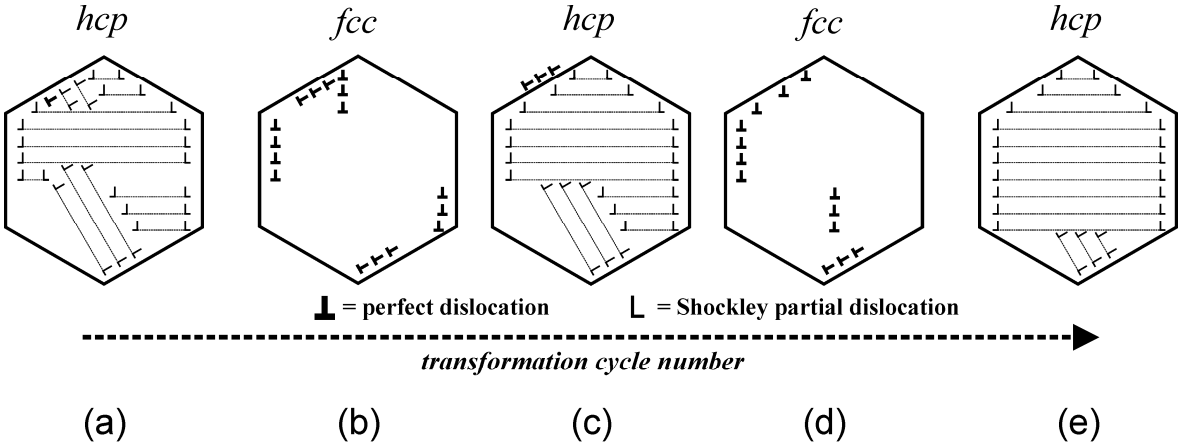

Fig. 6.5: Schematic presentation of the dislocation structure development in Co upon *hcp*↔*fcc* (thermal) cycling.
(a) The initial state represents (severely deformed) *hcp* Co as formed by dissociation of arrays of perfect dislocations and subsequent "ordered" glide of SPs on every second closest packed {111} plane in the parent *fcc* Co. The whole grain could not transform to *hcp* Co because of blocking of the growing martensite "plates" growing by "ordered" glide of arrays of SPs; each stack of SPs glides along one of the four equivalent types of $\{111\}_{fcc}$ planes.
(b) + (c) Upon continued thermal cycling the height of the (remaining, active) stacks of arrays of (partial) dislocations (perpendicular to $\{0001\}_{hcp}/\{111\}_{fcc}$ planes) increases, due to pick up of neighbouring dislocations, pushing aside unfavourably oriented smaller dislocation stacks, e. g. by limiting the associated SP glide, and by even driving them back (in associated form) into the grain boundaries (as illustrated in the figure; cf. (a) and (c)).
(d) + (e) Eventually, upon prolonged thermal cycling, a dislocation structure emerges that realizes the *hcp*↔*fcc* transformation on the basis of (ideally) one single stack of ordered perfect dislocations (in *fcc*) = 2 parallel stacks of ordered Shockley partial dislocations (in *hcp*) implying that only one (instead of, maximally, four; see (a) + (b)) glide plane system operates within a single grain, e. g. $(111)_{fcc} \| (0001)_{hcp}$, $[\bar{1}10]_{fcc} \| [\bar{1}0\bar{1}0]_{hcp}$.

The kinetics of the phase transformation from *hcp* to *fcc* Co upon isochronal annealing was described (Fig. 6.6) on the basis of a modular phase transformation model. Appropriate model descriptions for athermal nucleation and thermally activated, anisotropic interface controlled growth tailored to the martensitic phase transformation of Co were implemented into the modular model. Fitting of this model of phase transformation kinetics to simultaneously all isochronal DSC runs yielded values for the energy of the interface separating the *hcp* and *fcc* Co phase and the activation energy for growth.

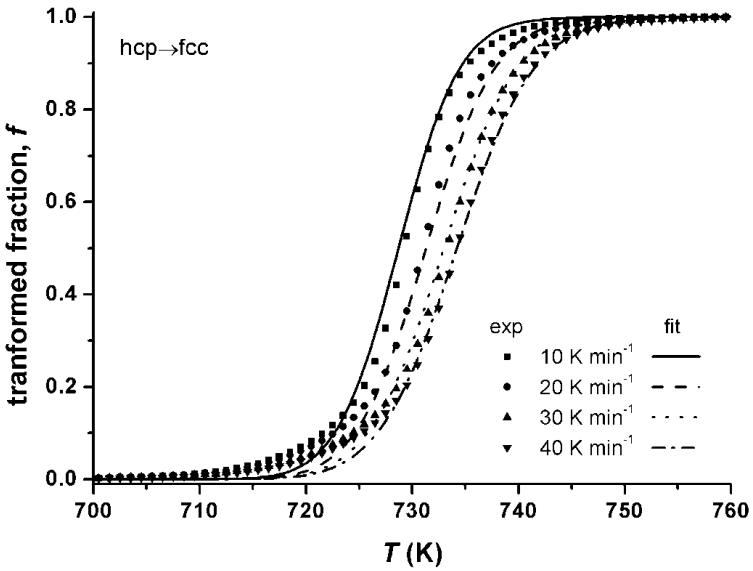

Fig. 6.6: Isochronal DSC curves (symbols) and model fit (simultaneously to all runs) using the modular phase transformation model (σ, Q and ξ as fit parameters) for the allotropic phase transformation *hcp→fcc* of Co.

7 Zusammenfassung

7.1 Natürliche Bildung von *krz* Co im Anfangsstadium der Ausscheidung von Co in übersättigtem $Au_{90}Co_{10}$

Im *Kapitel 2* dieser Doktorarbeit wird die anfängliche Ausscheidung von Co aus übersättigtem Au – 10.12 at. % Co. Die Entwicklung der Mikrostruktur, während einer isochronen Wärmebehandlung mittels Differenzial-Scanning-Kaloriemter (DSK) mit einer Heizrate von 20 K min^{-1}, wird mit (hochauflösender) Transmissionselektronenmikroskopie (TEM) untersucht. Dabei bildet sich auf natürliche Weise, bezüglich der bulk-Thermodynamik, metastabiles kubisch raumzentriertes (*krz*) Co mit einer plattenartigen Morphologie und einer Orientierungsbeziehung mit der Au-reichen Matrix vom Bain-Typ (Fig. 7.1).

Die metastabile *krz* Modifikation tritt auf, weil das anfänglich hohe Grenzflächen-zu-Volumenverhältnis die Ausbildung von Ausscheidungen mit niedriger Grenzflächenenergie fördert (wie es für die, bezüglich der Au-reichen Matrix, kohärenten Co Ausscheidungen gefunden wird). Während fortdauernder Wärmebehandlung kommt es zum Wachstum bzw. zur Vergröberung der Ausscheidungspartikel. Dabei kommt es mittels einer Bain Umwandlung des metastabilen *krz* Co zu Bildung der kubisch flächenzentrierten (*kfz*) Co Modifikation, welche kubische Orientierungsbeziehung mit der Au-reichen Matrix aufweist. Das niedrige Grenzflächen-zu-Volumenverhältnis der Ausscheidungsphase im fortgeschrittenen Stadium der Wärmebehandlung bewirkt einen Ausgleich der ungünstigen Grenzflächenenergie (inkohärent kontra kohärente Grenzfläche) durch eine viel günstigere chemische Volumenenergie (*kfz* kontra *krz* Modifikation).

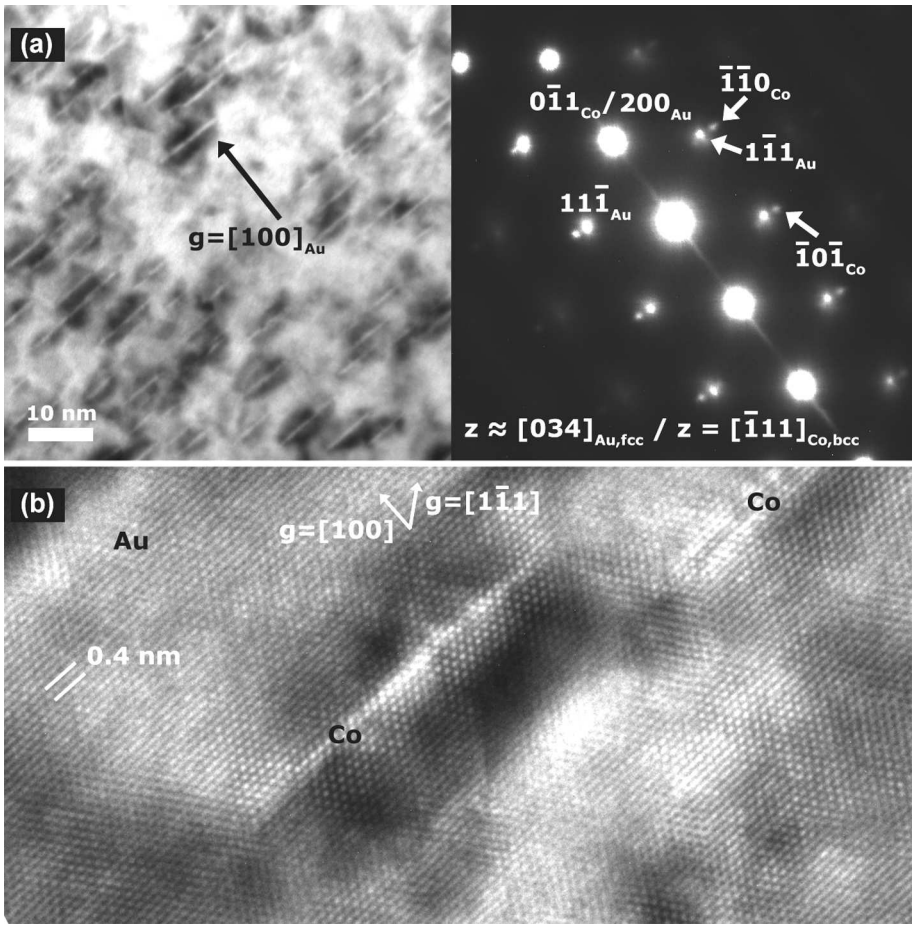

Fig. 7.1: Transmissionselektronenmikroskopische (TEM) Hell-Feld und hochauflösend TEM Bilder von $Au_{90}Co_{10}$ nach isochroner Auslagerung bis 633 K mit 20 K min^{-1}. (a) Die in der Nähe der {111} Au-matrix Beugungspunkte (siehe Pfeile im Beugungsbild) befindlichen Extrabeugungspunkte sind kompatibel mit *krz* Co Ausscheidungen in [-111] Zonenachse bezüglich Co. (b) Hochauflösendes TEM-Bild: [011] Zonenachse der Au-reichen Matrix; Co ist in Form sehr dünner kohärenter Platten ausgeschieden mit einer Dicke zwischen 0.5 bis 1 nm und einer Ausdehnung zwischen 5 und 10 nm.

7.2 Ausscheidung von Co aus übersättigtem $Au_{90}Co_{10}$: Morphologie und Kinetik

In *Kapitel 3* dieser Doktorarbeit wird die Kinetik der Ausscheidungsreaktion von Co aus anfänglich übersättigtem $Au_{90}Co_{10}$ und die dazugehörige Morphologie dieser Ausscheidungen untersucht. Abgeschreckte Proben der übersättigten Au-Co-Legierung werden in einem Differenzial-Scanning-Kalorimeter (DSK) einer isothermen und isochronen Wärmebehandlung unterzogen, um die Ausscheidung von Co voranzutreiben und die dabei auftretenden Wärmetönung zu verfolgen, welche für die kinetische Analyse verwendet wird. Die Mikrostruktur, Phasenzusammensetzung und mechanischen Eigenschaften werden mittels (hochauflösender) Transmissionselektronenmikroskopie [(HR)TEM], Röntgenbeugungsanalyse (XRD) und Härtemessung untersucht.

Plattenartige kohärente *krz* Co Nanopartikel (Dicke ≈ 0.5 – 1 nm, Länge ≈ 5 - 10 nm) bilden sich während isothermer und isochroner Wärmebehandlung im Anfangsstadium der Ausscheidung von abgeschreckten übersättigtem Au – 10.12 at. % Co im Korninneren mit einer Orientierungsbeziehung nach Bain [$(100)_{Au,kfz}//(100)_{Co,krz}$ and $[001]_{Au,kfz}//[011]_{Co,krz}$ (drei Varianten)]. Im weiteren Verlauf der Wärmebehandlung kommt es zum Übergang von kohärentem *krz* Co zu inkohärentem *kfz* Co, welches epitaktisch zur Au-Matrix orientiert ist matrix [$(100)_{Au,kfz}//(100)_{Co,kfz}$ and $[001]_{Au,kfz}//[001]_{Co,kfz}$ (drei Varianten)]. Der Übergang von *krz* zu *kfz* ist verknüpft mit einem geringen Wärmeffekt sichtbar durch Ausbildung einer Schulter im DSK-Signal. Während fortdauernder isochroner Wärmebehandlung bilden sich äquaxiale Ausscheidungsteilchen.

Ein kleiner Anteil an diskontinuierlicher Ausscheidung (DA) tritt in kleinen Bereichen nahe der Korngrenze auf (< 0.5 vol. %).Die DA stoppt in einem frühen Stadium aufgrund der kontinuierlichen Keimbildung in Kombination mit einer Blockierung der wandernden Reaktionsfront der DA und einer kleiner werdenden Triebkraft für die DA durch eine sinkende Übersättigung mit voranschreitender Ausscheidung.

Die Keimbildungs- und Wachstumsmodi für die Ausscheidung von kohärenten *krz* Co Teilchen konnten mittels Anpassung eines modularen Phasenumwandlungsmodels, simultan an jeweils all isotherme bzw. isochrone Heizläufe mit DSK, bestimmt werden. Im Fall der isothermen Wärmebehandlung (Fig. 7.2a) wird die Kinetik von präexistenten Keimen zum Zeitpunkt $t = 0$ in Kombination mit grenzflächenkontrolliertem Wachstum beschrieben. Die effektive Aktivierungsenergie für die Umwandlung mit ungefähr 60 kJ mol^{-1} ist allein durch die Aktivierungsenergie für das Wachstum gegeben und kann als die Wanderungsenergie von Leerstellen verstanden werden. Im Fall der isochronen Wärmebehandlung (Fig. 7.2b) wird die Kinetik der Ausscheidung durch kontinuierliche Keimbildung in Kombination mit grenzflächenkontrolliertem Wachstum beschrieben. Die effektive Aktivierungsenergie entspricht ungefähr 100 kJ mol^{-1}, und ist im Allgemeinen durch die gewichtete Summe der Aktivierungsenergien für Keimbildung und Wachstum gegeben. Im vorliegenden Fall sind die Aktivierungsenergien für Keimbildung und Wachstum ungefähr gleich, einen jeweiligen Wert von 100 kJ mol^{-1} vorausgesetzt.

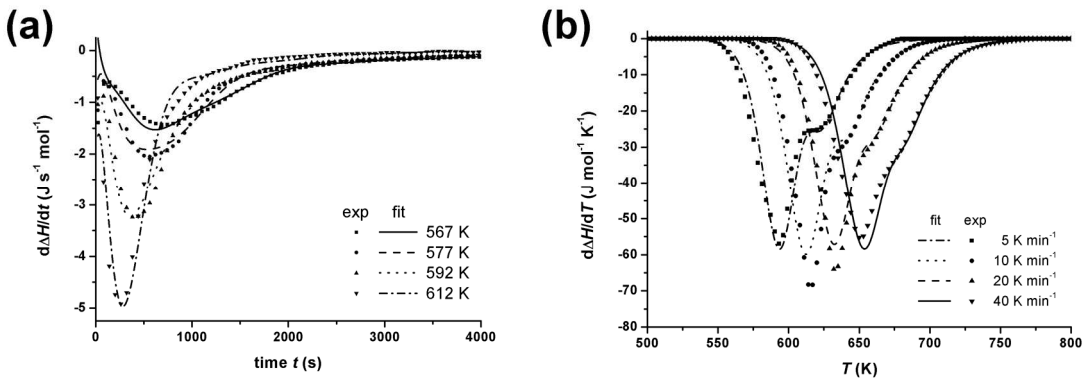

Fig. 7.2: (a) Isotherme und (b) isochrone DSK Kurven (Symbole) und Ergebnisse der Anpassung (Linien) des modularen Phasenumwandlungsmodels simultan an alle isotherme bzw. isochrone DSK-Läufe.

Der Unterschied der Keimbildungsmodi für die isothermen und isochronen Wärmebehandlungen ist eine direkte Konsequenz von, während dem Abschrecken, eingefrorenen Leerstellen und Versetzungen und dem Unterschied im Ausmaß der Erholungsreaktion vor Erreichen des Beginns der Ausscheidung. Während im Fall der isothermen Wärmebehandlung die meisten eingefrorenen Gitterdefekte vorhanden sind zu Beginn der Ausscheidung, hat im Fall der isochronen Wärmebehandlung eine zumindest teilweise Erholungsreaktion vor Beginn der Ausscheidungsreaktion stattgefunden. Als Konsequenz ist eine kleine Menge an Leerstellen und Versetzungen aktiv. Die bedingt, im Vergleich zum isothermen Fall, einen anderen Keimbildungsmodus (präexistierende Keime → kontinuierliche Keimbildung) und eine größere Aktivierungsenergie (größer als die für die Wanderungsenergie von Leerstellen).

7.3 Kinetik der Ausscheidung von Co aus einer überstättigtem Cu-Co-Legierung

In Kapitel 4 dieser Doktorarbeit wird die Kinetik der Ausscheidung von Co aus anfänglich übersättigtem Cu – 0.95 at. % Co während einer isochronen Wärmebehandlung mittels Differenzial-Scanning-Kalorimtrie (DSK) untersucht (Fig. 7.3). Die Mikrostruktur wird mittels (hochauflösender) Transmissionselektronenmikroskopie [(HR)TEM] untersucht (Fig. 7.4).

Die Ausscheidung von *kfz* Co aus übersättigtem Cu – 0.95 at. % Co wird im Rahmen des modularen Phasenumwandlungsmodels durch kontinuierliche, zufällige Keimbildung und diffusionskontrolliertem, isotropem Wachstum beschrieben.

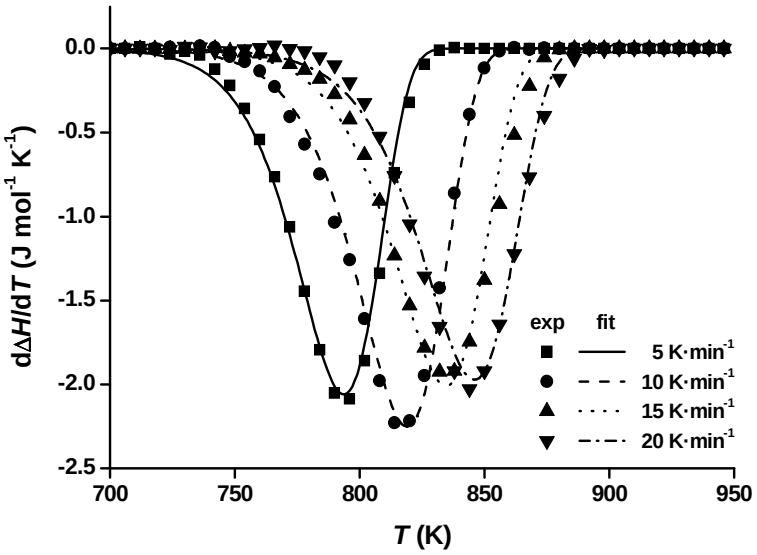

Fig. 7.3: Isochrone DSK Kurven (Symbole) und Modelanpassung (gleichzeitig an alle Läufe) unter Anwendung des modularen Phasenumwandlungsmodels für Ausscheidung von Co aus übesättigtem Cu – 0.95 at. % Co.

Die Anpassung des kinetischen Models an die Umwandlungsratendaten (durch die DSK Kurven gegeben) (Fig. 7.3) unter zusätzlichen Bedingung wie durch eine mikroskopische TEM-Analyse gegeben, ermöglicht die Bestimmung von kinetischen Parametern, welche die separaten Keimbildungs- und Wachstumsmodi charakterisieren.

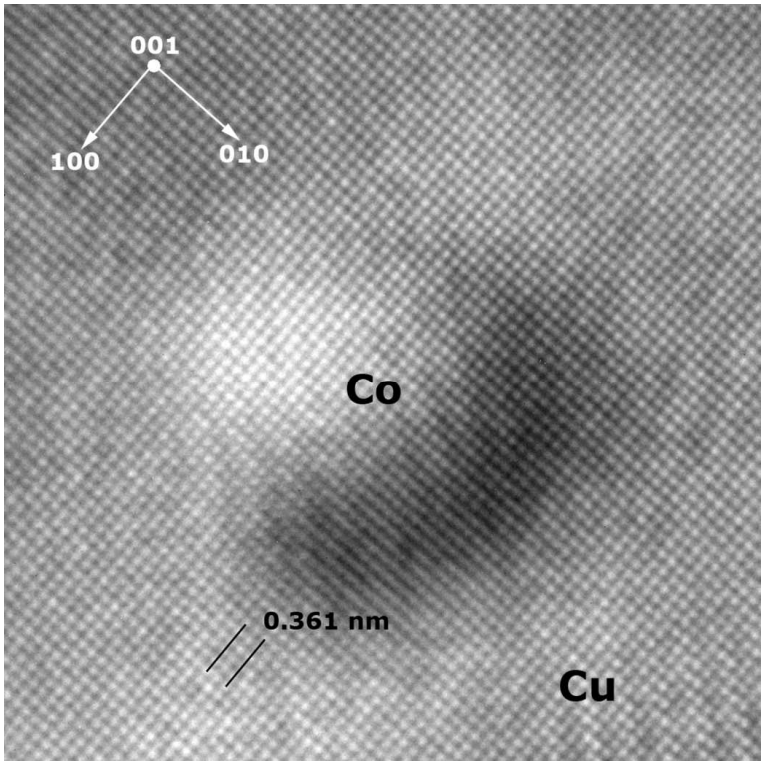

Fig. 7.4: HRTEM-Bilder von Cu – 2 at. % Co ausgelagert bei 843 K für 60 min ([001] Zonenachse). Das Bild zeigt einen kugelförmige Co-reichen Partikel vollständig kohärent mit der umgebenden Cu-reichen Matrix. Das Ausscheidungsteilchen hat eine *kfz* Struktur, genau wie die Matrix.

Die effektive, allumfassende Aktivierungsenergie von ungefähr 133±8 kJ mol^{-1} kann (daher) in die separaten Aktivierungsenergien für das Wachstum mit 50 kJ mol^{-1} und die Keimbildung mit 177 kJ mol^{-1}. Die Keimbildung kommt zum Erliegen lange bevor das gesamte gelöste Co in der Cu-reichen ausscheiden konnte. Die Ausscheidung geht nur mittels Wachstum oder Vergröberung weiter. Die Aktivierungsenergie für das Wachstum ist deutlich kleiner als die Aktivierungsenergie von normalgeglühtem Co aufgrund von eingefrorenen Überschussleerstellen.

7.4 Kinetik der allotropen *hdp-kfz* Phasenumwandlung in Kobalt

Im letzten, *fünften Kapitel* dieser Doktorarbeit wird die allotrope Phasenumwandlung in Co von der hexagonal dichtgepackten (*hdp*) Niedrigtemperaturphase zur kubisch flächenzentrierten (*kfz*) Hochtemperaturphase untersucht. Vor der eigentlichen kinetischen Analyse der martensitischen Phasenumwandlung von *hdp* nach *kfz* in Co während einer isochronen Wärmebehandlung mittels Differnzial-Scanning-Kalorimetrie (DSK) bei verschiedenen Heizraten von 10 to 40 K min^{-1} in einem festen Temperaturbereiche, wurden alle verwendeten Kobaltproben thermisch zykliert mit einer Heizrate von 50 K min^{-1}, um mikrostrukturelle Inhomogenitäten auszugleichen.

Mittels Röntgenbeugungsanalyse sowie der Erfassung von DSK Parametern wie der Enthalpie, der Peakonset- und der Peakmaximumtemperatur, welche aus den thermischen Zyklierungsexperimenten gewonnen werden, kann die mikrostrukturelle Entwicklung verstanden werden. In jedem einzelnen Co Korn der polykristallinen Proben bildet sich eine bevorzugte Gleitebene, beispielsweise $(0001)_{hdp}||(111)_{kfz}$, was zu einer gerichteten Umwandlung führt (Fig. 7.5).

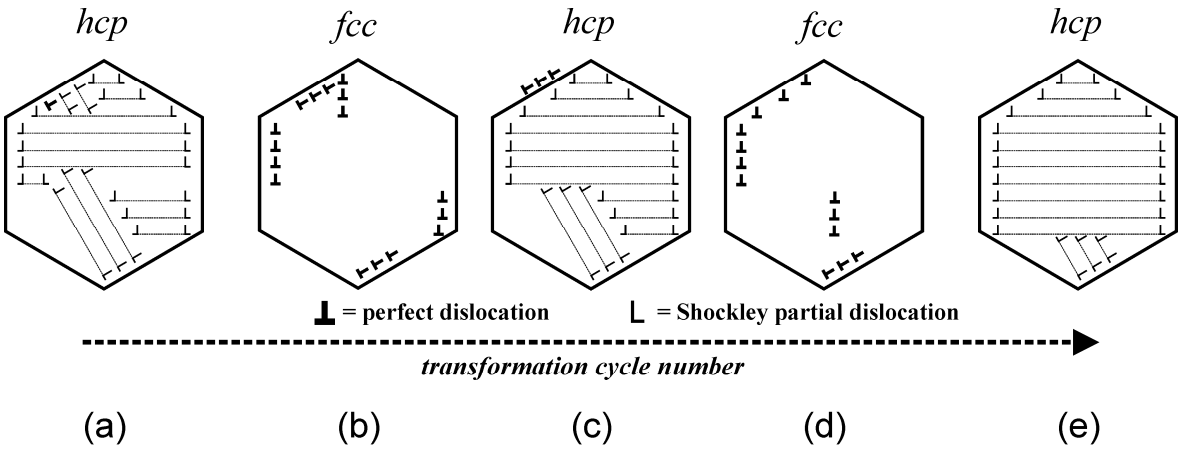

Fig. 7.5: Schematische Darstellung der *kfz*↔*hdp* Umwandlung in Co während des thermischen Zyklierens.
(a) Der Anfangszustand stellt stark verformtes *hdp* Co dar, wie es durch die Dissoziation von Anordnungen perfekter Versetzungen und anschließendem Gleiten von SPs auf jeder zweiten dichtgepackten {111} Ebene der vorhergehenden *kfz* Co Phase geformt wird. Das komplette Korn kann dabei nicht in *hdp* Co umwandeln, da sich die wachsenden „Martensitplatten", die durch das "geordnete" Gleiten von SPs wachsen, gegenseitig blockieren; jeder Stapel von SPs gleitet entlang einer von vier gleichberechtigten Typen von $\{111\}_{kfz}$ Ebenen.
(b) + (c) Während des andauernden thermischen Zyklierens vergrößert sich die Höhe der (verbleibenden, aktiven) Stapelanordnungen der (partiellen) Versetzungen (senkrecht zu $\{0001\}_{hdp}/\{111\}_{kfz}$ Ebenen) durch das Aufsammeln von benachbarten Versetzungen und dem gleichzeitigen Wegschieben von ungünstig orientierten, kleineren Versetzungsstapeln, z. B. durch Limitierung der damit verbundenen SP-Gleitung, und durch deren Verdrängung in die Korngrenzen (wie in der Abbildung schematisch dargestellt; siehe (a) und (c)).
(d) + (e) Schließlich, während dem voranschreitenden thermischen Zyklieren, bildet sich eine Versetzungsstruktur heraus, mittels derer die *hdp*↔*kfz* Umwandlung auf Basis von (idealerweise) Einzelstapeln von geordneten, perfekten Versetzungen möglich wird (in *kfz*) = 2 parallele Stapel von geordneten Shockley Partialversetzungen (in *hdp*) unter der Voraussetzung, dass nur ein (anstelle von, maximal, vier, siehe (a) + (b)) Gleitebendensystem innerhalb eines Korns aktiv ist, z. B. $(111)_{fcc} \| (0001)_{hcp}$, $[\bar{1}10]_{fcc} \| [\bar{1}0\bar{1}0]_{hcp}$

Die Kinetik der martensitischen *hdp*→*kfz* Phasenumwandlung in Co wurde erfolgreich unter Anwendung einer modularen Phasenumwandlungsmodels beschrieben (Fig. 7.6) unter der Annahme von athermischer Keimbildung, thermisch aktiviertem Wachstum, gesteuert durch die Bewegung von Shockleypartialversetzungen, und anisotropen Zusammenstoß.

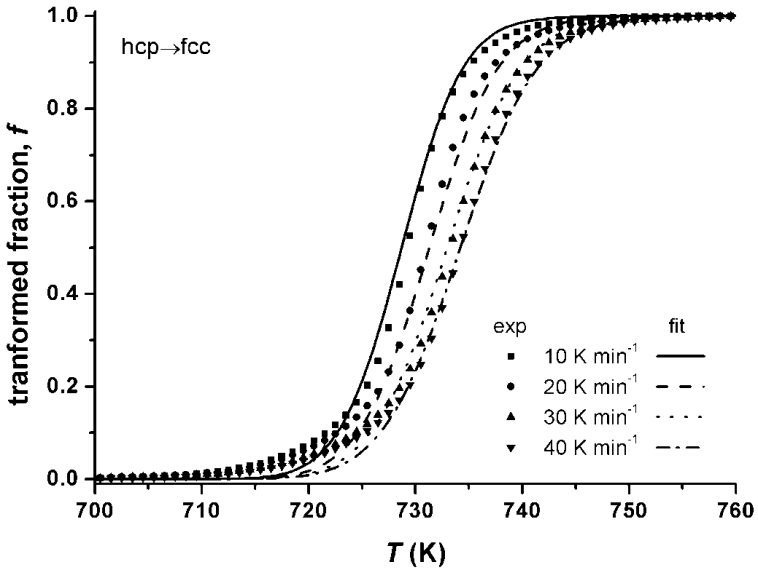

Fig. 7.6: Isochrone DSK-Kurven (Symbole) und Modelanpassung (simultan an alle Läufe) unter Anwendung des modularen Phasenumwandlungsmodels (σ, Q und ξ als Anpassungsparameter) auf die allotrope Phasenumwandlung *hdp→kfz* von Co.

List of Publications

1. R. Bauer, M. Baccalaro, L. P. H. Jeurgens, M. Pohl, and E. J. Mittemeijer, Oxidation behavior of Fe-25Cr-20Ni-2.8Si during isothermal oxidation at 1286 K; Life time prediction, *Oxidation of Metals* **69** (2008) 265.

2. R. Bauer, E. Bischoff, and E. J. Mittemeijer, Natural formation of *bcc* Co; Initial stage of Co precipitation in supersaturated $Au_{90}Co_{10}$, *Physical Review B* **81**(9) (2010) 094113. Chapter 2 of this thesis.

3. R. Bauer, E. Bischoff, and E. J. Mittemeijer, Precipitation of Co from Supersaturated $Au_{90}Co_{10}$: Microstructure and Kinetics, *International Journal for Materials Research* (2010) submitted. Chapter 3 of this thesis.

4. R. Bauer, B. F. Rheingans, and E. J. Mittemeijer, The kinetics of the precipitation of Co from supersaturated Cu Co Alloy, *Metallurgical and Materials Transactions A* (2010) accepted for publication. Chapter 4 of this thesis.

5. R. Bauer, E. A. Jägle, W. Baumann, and E. J. Mittemeijer, Kinetics of the Allotropic hcp-fcc Phase Transformation in Cobalt, *Philosophical Magazine* (2010) accepted for publication. Chapter 5 of this thesis.

6. R. Bauer, E. Bischoff, and E. J. Mittemeijer, Precipitation of Co in Supersaturated Au-based Au-Co Alloys; Microstructural Evolution and Transformation Kinetics, Conference Proceeding PTM 2010, *Solid State Phenomena* (2010) submitted.

Danksagung

Die vorliegende Arbeit wurde am Institut für Materialwissenschaft der Universität Stuttgart und am Max-Planck-Institut für Metallforschung, Stuttgart, angefertigt. An dieser Stelle möchte ich all denen danken, die zum Gelingen der Arbeit beigetragen haben.

An erster Stelle möchte ich Herrn Prof. Dr. Ir. E. J. Mittemeijer dafür danken, dass er mich in seine Abteilung aufgenommen und mir dieses überaus interessante Thema überlassen hat, sowie mich stets durch sein uneingeschränktes Vertrauen bestärkte. Sein außergewöhnliches Engagement bei der Betreuung der Arbeit als Doktorvater und als täglicher Betreuer in Form von meist wöchentlichen wissenschaftlichen Diskussionen, sowie seine stetige Bereitschaft zum freien Gedankenaustausch haben maßgeblich zum Erfolg der Arbeit beigetragen.

Herrn Prof. Dr. J. Bill danke ich für die freundliche Übernahme des Mitberichts, sowie Herrn Prof. Dr. T. Schleid für die Bereitschaft den Prüfungsvorsitz zu übernehmen.

Herrn Dr. E. Bischoff gebührt ein besonderer Dank. Er hat durch sein unerschöpfliches Fachwissen und seine Geduld auf dem Gebiet der Elektronenmikroskopie wesentlich zum Gelingen dieser Arbeit beigetragen.

Allen Mitarbeitern des Max-Planck-Instituts für Metallforschung, insbesondere den Kollegen der Abteilung Mittemeijer, gilt mein herzlicher Dank für die vertrauensvolle Zusammenarbeit und die angenehme Arbeitsatmosphäre. Namentlich möchte ich mich bei Herrn Dr. Wolfgang Baumann für seine Geduld und die Zusammenarbeit, sowie bei Frau Ute Schestag für die fachliche und menschliche Unterstützung bei der Meisterung von Höhen und Tiefen bedanken.

Meiner lieben Ehefrau Bianca, meiner Tochter Lena und meinem Sohn Max gebührt ein besonderer Dank für ihre Geduld und den persönlichen Rückhalt. Zu guter Letzt möchte ich meinen Eltern dafür danken, dass sie mir diesen Weg ermöglicht haben.

Curriculum Vitae

Persönliche Daten

Name	Rico Bauer
Geburtsdatum	09.12.1979
Geburtsort	Jena
Staatsangehörigkeit	deutsch

Schulbildung

1986 – 1989	Grundschule Eisenberg
1989 – 1990	Grundschule Öhringen
1990 – 1999	Hohenlohe Gymnasium Öhringen Abschluss: Abitur

Hochschulbildung

2000 – 2005	Studium der Werkstoffwissenschaft an der Universität Stuttgart
03/2005 – 09/2005	Diplomarbeit am Institut für Metallkunde (*heute*: Institut für Materialwissenschaft), Lehrstuhl I, Universität Stuttgart in Kooperation mit der Robert Bosch GmbH, Schillerhöhe Thema: „Hochtemperaturoxidation von Fe-25Cr-20Ni-2.8Si“ Hauptberichter: Prof. Dr. Ir. E. J. Mittemeijer
09/2005	Abschluss: Diplom-Ingenieur

Promotion

2005 – 2010	Max-Planck-Institut für Metallforschung, Stuttgart und Institut für Materialwissenschaft, Lehrstuhl I, Universität Stuttgart Thema: „Solid-Solid Phase Transformation Kinetics“ Hauptberichter: Prof. Dr. Ir. E. J. Mittemeijer